分类号________ 密级________

U D C ________ 编号________

华中师范大学

博士学位论文

相对论重离子碰撞中净质子，质子和反质子数分布的高阶矩和关联函数测量

学 位 申 请 人 姓 名: 杨贞贞

申请学位学生类别: 全日制博士

申请学位学科专业: 粒子物理与原子核物理

指 导 教 师 姓 名: 罗晓峰 副教授

许 怒 教 授

博士学位论文

相对论重离子碰撞中净质子、质子以及反质子数分布的高阶矩和关联函数测量

论文作者：杨贞贞
指导教师：罗晓峰 副教授　许怒 教授
学科专业：粒子物理与原子核物理
研究方向：相对论重离子物理

华中师范大学物理科学与技术学院
二零二零年六月

Dissertation

Measurements of Higher-order Cumulants of Net-Proton、 Proton and Anti-Proton Multiplicity Distributions and Correlation Functions in Relativistic Heavy Ion Collisions

By

Zhenzhen Yang

Supervisor: **Prof. Xiaofeng Luo Prof. Nu Xu**

Specialty: **Particle Physics and Nuclear Physics**

Research Area: **Heavy Ion Collisions**

College of Physical Science and Technology

Central China Normal University

Jun. 2020

华中师范大学学位论文原创性声明和使用授权说明

原创性声明

本人郑重声明：所呈交的学位论文，是本人在导师指导下，独立进行研究工作所取得的研究成果。除文中已经标明引用的内容外，本论文不包含任何其他个人或集体已经发表或撰写过的研究成果。对本文的研究做出贡献的个人和集体，均已在文中以明确方式标明。本声明的法律结果由本人承担。

作者签名：　　　　　　　　　　　　日期：　　年　　月　　日

学位论文版权使用授权书

学位论文作者完全了解华中师范大学有关保留、使用学位论文的规定，即：研究生在校攻读学位期间论文工作的知识产权单位属华中师范大学。学校有权保留并向国家有关部门或机构送交论文的复印件和电子版，允许学位论文被查阅和借阅；学校可以公布学位论文的全部或部分内容，可以允许采用影印、缩印或其它复制手段保存、汇编学位论文。（保密的学位论文在解密后遵守此规定）

保密论文注释：本学位论文属于保密，在 ___年解密后适用本授权书。

非保密论文注释：本学位论文不属于保密范围，适用本授权书。

作者签名：　　　　　　　　　　　　导师签名：

日期：　　年　　月　　日　　　　　日期：　　年　　月　　日

本人已经认真阅读"CALIS 高校学位论文全文数据库发布章程"，同意将本人的学位论文提交"CALIS 高校学位论文全文数据库"中全文发布，并可按"章程"中的规定享受相关权益。同意论文提交后滞后：□半年；□一年；□二年发布。

作者签名：　　　　　　　　　　　　导师签名：

日期：　　年　　月　　日　　　　　日期：　　年　　月　　日

摘要

强相互作用力(也被称为核力)，是自然界四种基本相互作用力之一，它将核子(质子与中子)束缚形成原子核并支配着自然界中 90%以上的可见物质。量子色动力学（Quantum Chromodynamics, QCD)是描述强作用力的现代理论。组成物质的基本单元—夸克与胶子，被强作用力禁闭在核子中，因此在自然界没有发现自由的夸克与胶子。高温高密核物质相图是核物理研究领域的前沿和热点。格点 QCD 预言在高温低重子密度区域，强子物质和夸克胶子等离子体之间发生的相变是平滑穿越，而基于量子色动力学(QCD)有效模型计算表明在高重子密度区域，他们之间是一阶相变。因此，如果平滑穿越和一阶相变边界真的如理论所预言，那么在一阶相变边界延伸到平滑穿越区一定会存在一个终结点，被称为 QCD 相变临界点。QCD 临界点的实验确认将是探索强相互作用物质相结构的里程碑，具有重要科学意义。为了在这一具有潜在重大发现的研究方向上占据领先地位、取得突破，各个国家纷纷建造大型粒子探测器、开展重离子碰撞实验(包括：美国 RHIC-STAR 能量扫描实验， 德国 CBM 实验、俄罗斯 NICA 实验、日本 J-PARC 实验以及中国兰州 CSR 外靶 CEE 实验)，其主要物理目标就是研究高温高密核物质相图结构、寻找 QCD 相变临界点。

在束流能量扫描（BES）项目的第一阶段，位于美国布鲁克海文国家实验室的相对论重离子对撞机（RHIC）使用 STAR 探测器，通过加速重离子完成了金金每核子对的质心碰撞能量为 7.7，11.5， 14.5， 19.6， 27， 39， 54.4， 62.4 和 200 GeV 的数据采集。这就使我们能够探索相图中比较宽广的区域，有利于临界点的寻找。

在这篇论文中，我们完成了在金金对撞中质心碰撞能量为 $\sqrt{s_{NN}} = 7.7 - 200$ GeV, 在中心快度区间 ($|y| < 0.5$) 和横动量区间为 $0.4 < p_T < 2.0$ GeV/c 内， 质子，反质子和净质子数分布的直到四阶累积矩以及它们的比值和（反）质子的关联函数的测量；铜铜碰撞中，质心碰撞能量为 $\sqrt{s_{NN}} =$ 22.4， 62.4 和 200 GeV 下，在中心快度区间($|y| < 0.5$)和横动量区间为 $0.4 < p_T < 0.8$ GeV/c 内，质子，反质子和净质子数分布的直到四阶累积矩以及它们的比值；金金碰撞固定靶实验中碰撞能量为 $\sqrt{s_{NN}} =$ 4.5 GeV 下，在快度区间为 $-2 < y < 0$和横动量区间为 $0.4 < p_T < 2.0$ GeV/c 内，（反）质子数分布的直到四阶累积矩以及它们的比值。

各阶累积矩和它们的比值可以表示为碰撞中心度，快度和横动量和能量的函数。我们观察到在最中心 ($0 - 5\%$) 金金碰撞中， C_4/C_2 这一比值随着能量呈现出非单调变化的趋势，其偏离值为3.1σ。为了理解横动量接受度，净重子与净质子和净重子数守恒的影响， 在 STAR 接受度范围中进行了输运模型 UrQMD 和强子共振气体（HRG）模型计算。金金碰撞中 C_3/C_2 和 C_4/C_2 的 UrQMD 和 HRG 模型计算显示出随着能量的单调变化。 我们也与具有 QCD 相变临界点的模型相比较， 发现实验测量得到的 C_4/C_2，其碰撞能量的依赖性符合理论模型的预期结果。此外，从测得的累积量中，我们提取出质子和反质子的的关联函数，发现质心能量在 7.7 GeV 时中心碰撞中质子分布的 C_4/C_2 值增大是由于四粒子关联。我们在 RHIC 第一阶段能量扫描的守恒荷涨落测量中，首次观测到净质子数四阶涨落对碰撞能量的非单调依赖(3.1σ显著性)，该实验测量为寻找 QCD 相变临界点提供了重要实验依据，也为 RHIC

第二阶段能量扫描以及 STAR 固定靶实验中守恒荷涨落的高精度测量奠定了基础。

这篇文章组织结构如下。第一章主要介绍了分析的目的和实验中所需要的观测量，以及这些量在统计与概率中的表示。在第二章中，我们简单介绍了 RHIC 上的 STAR 探测器及其子探测器的结构和功能。第三章中主要介绍了在实验分析中的细节，数据选择，事件选择，粒子鉴别，中心度的定义，以及净质子数的分布和模型简介。第四章主要研究了一些效应对于结果的影响，例如中心度宽度修正和有限探测器效率修正。最后一章中我们将会呈现实验的计算结果，包括在金金对撞中的质心系模式和固定靶模式以及铜铜对撞， 并进行讨论和实验的发展前景。

关键词：重离子碰撞；QCD 相变；QCD 临界点；高阶矩；关联函数

Abstract

Strong interaction forces (also known as nuclear forces) are one of the four fundamental interaction forces in nature that bind nucleus (protons and neutrons) to form atomic nuclei and dominate more than 90% of the visible matter in nature. Quantum Chromodynamics (Quantum Chromodynamics, QCD) is a modern theory that describes strong interaction forces. The basic unit of the substance, quarks and glues, is confined to the nucleus by strong interaction forces, so no free quarks and gluons are found in nature. The phase diagram of high temperature and high-density nuclear material is the frontier and hot spot in the field of nuclear physics research. Lattice QCD predicts that at high temperature and low baryon chemical potential, the phase transition between the hadron matter and the quark gluon plasma occurs is smooth crossover, while the model predicts that at the high baryon chemical potential, the phase transition between them is a first-order phase transition. Therefore, if the first-order phase transition does exist, then there must be an end point in the end of the first-order phase transition line to the smooth crossover, which is called the QCD critical point.

The experimental confirmation of QCD critical point will be a milestone in the exploration of the phase structure of strong interaction substances, which is of great scientific significance. In order to take a leading position in this potentially significant discovery research direction and make a breakthrough, various countries have built large particle detectors and carried out heavy ion collision experiments (including: RHIC-STAR beam energy scanning experiment in the United States, CBM experiment in Germany, NICA experiment in Russia, J-PARC experiment in Japan and CEE experiment of the external target of CSR in Lanzhou, China), the main physical goal is to study the structure of high temperature and high-density nuclear material phase diagram, search for the critical point.

In the first phase of Beam Energy Scan (BES) program, Relativistic Heavy Ion Collider (RHIC) located at Brookhaven National Laboratory (BNL), in the Unites States used the STAR detector to complete data collection of 7.7, 11.5 14.5, 19.6, 27, 39, 54.4, 62.4 and 200 GeV by accelerating heavy ions. This allows us to explore the phase diagram in a broader range.

In this thesis, we have finished the measurements of up to the fourth-order cumulants (C_n) of the proton, anti-proton and net-proton multiplicity distributions and correlation functions of (anti-) protons in Au+Au collisions for center of mass energies per nucleon pair, $\sqrt{s_{\mathrm{NN}}}$ = 7.7, 11.5, 14.5, 19.6, 27, 39, 54.4, 62.4 and 200 GeV. The measurements are carried out at mid-rapidity (|y| < 0.5) and for transverse momentum $0.4 < p_{\mathrm{T}} < 2.0$ (GeV/c); the measurements of up to the fourth-order cumulants (C_n) of the proton, anti-proton and net-proton multiplicity distributions in Cu+Cu collisions for center of mass energies per nucleon pair, $\sqrt{s_{\mathrm{NN}}}$ = 22.4, 62.4 and 200 GeV at mid-rapidity (|y| < 0.5) and for transverse momentum $0.4 < p_{\mathrm{T}} < 0.8$ (GeV/c); the measurements of up to the fourth-order cumulants (C_n) of the proton, multiplicity distributions in Au+Au collisions

at Fixed-Target mode $\sqrt{s_{\mathrm{NN}}}$ = 4.5 GeV at -2 < y < 0 and for transverse momentum 0.4 < p_{T}< 2.0 (GeV/c).

The various order cumulants C_n and their ratios can be expressed as a function of collision centrality, rapidity, transverse momentum $p_{\mathrm{T}}$and collision energy. We observe a non-monotonic variation of the ratio of C_4/C_2 with the significance of 3.1σ for the most central $(0-5\%)$ Au+Au collisions with $\sqrt{s_{\mathrm{NN}}}$. Transport model UrQMD and Hadron Resonance Gas (HRG) model calculations are carried out in the STAR acceptance to understand the effect of p_{T} acceptance, net-baryon versus net-proton and conservation of net-baryon number. The UrQMD and HRG model calculations of C_3/C_2 and C_4/C_2 in Au+Au collisions show a monotonic variation with $\sqrt{s_{\mathrm{NN}}}$. The collision energy dependence of the C_4/C_2 is consistent with expectations from a QCD based model with critical point. Further, we extract the various order correlation functions of protons and anti-protons from the measured cumulants in Au+Au collisions and find that the large value of C_4/C_2 for proton distributions in central collisions at $\sqrt{s_{\mathrm{NN}}}$ = 7.7 GeV is due to four-particle correlations. In the fluctuation measurements of conserved quantities in the RHIC's first beam energy scan program, we observed the non-monotonous dependence (3.1σ) of the net-proton number four-order fluctuations on the collision energy for the first time, which provides an important experimental baseline for searching for the critical point of QCD phase transition, and also lays the foundation for the high precision measurement of the conservation load in the second phase of beam energy scan and the STAR fixed target experiment at RHIC.

This thesis is organized as follows. The first chapter mainly introduced the motivation, the experimental measurements and the presentation of these observables in statistics and probability. In the second chapter, we briefly introduced the structure and function of the STAR detector and its sub-detectors at RHIC. The third chapter mainly introduces the details of experimental analysis, data selection, event selection, particle identification, definition of centrality, multiplicity distribution of net protons and model introduction. The fourth chapter mainly studies the effect of some effects on the results, such as the centrality bin width correction of and the limited detector efficiency correction. In the last chapter, we will present the calculation results of the experiment, including the centroid model and fixed target mode in the Au+Au collisions and the Cu+Cu collisions, and discuss the development prospects of the experiment.

Key Words: Heavy Ion Collisions; QCD Phase Transition; QCD Critical Point; Higher Order Cumulants; Correlation Function

Contents

List of Figures

List of Tables

Chapter 1

Introduction

1.1 Quantum Chromodynamics

Quantum Chromodynamics (QCD) is the theory of strong interactions, one of the four fundamental forces. The theory describes the interactions between quarks and gluons and is an important part of standard model of particle physics. Quarks and gluons, which have three different color charges (red, green and blue), can form the hadrons. Hadrons are divided into two kinds: baryons and mesons. Baryons are made of three quarks, such as protons and neutrons; mesons are made of a quark and an anti-quark, such as pions and kaons.

Color confinement and asymptotic freedom are the two characteristics of QCD. The static QCD potential V_s and running coupling constant $\alpha_s(Q)$ are written by:

$$V_s = -\frac{4}{3} \times \frac{\alpha_s}{r} + k \times r \tag{1.1}$$

$$\alpha_s(Q) = \frac{g_s^2}{4\pi} \approx \frac{4\pi}{(11 - \frac{2}{3} \times n_q) log(Q^2/\Lambda_{QCD}^2)} \tag{1.2}$$

where Q is the energy scale, n_q is the number of quark flavors and Λ_{QCD} is the QCD scale.

Fig. 1.1 shows the running coupling constant α_s as a function of energy scale. The running coupling constant α_s decreases with the increasing energy scale Q. On the one hand, if the distance between quarks is small ($r \to 0$) or the momentum transfer is large ($Q \to \infty$), α_s becomes smaller ($\alpha_s \to 0$), which means the interaction among quarks and gluons becomes weak and QCD can be computed by means of perturbation method. This property is called asymptotic freedom. On the other hand, if the distance between the quarks is large ($r \to \infty$) or momentum transfer according to QCD scale ($Q \to \Lambda_{QCD}$), α_s becomes larger ($\alpha_s \to \infty$), which means the interaction among quarks and gluons becomes strong, and the quarks can be confined in the hadrons. This property is called color confinement. Therefore, the confined quarks and gluons can't be observed directly.

1.2 QCD Phase Transition and Critical Point

From Eq. 1.2, when $r \to \infty$ or $Q \to \Lambda_{QCD}$, the nuclear matter is in the hadron gas phase, however, if we decrease the distance between the quarks and gluons or enlarge the momentum exchange, the interaction between quarks and gluons becomes weak. That

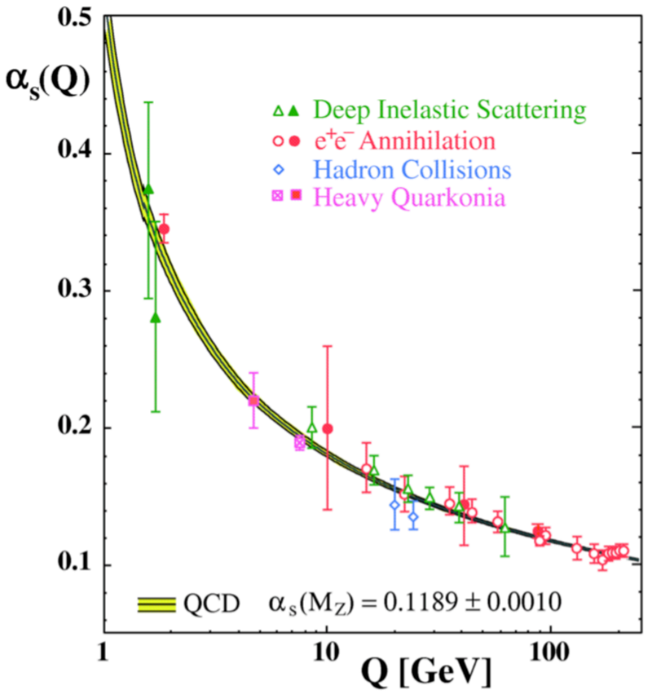

Fig. 1.1: (color online) Running coupling constant $\alpha_s(Q)$ as a function of energy scale Q. Figure is taken from[1, 2].

is to say, with high densities and temperature, quarks and gluons are released from deconfinement and enter a new phase−the quark-gluon plasma (QGP). The matter in the new state is thought to consist of asymptotical free quarks and gluons and behaves as a fluid. The two-dimensional diagram with the temperature T and the baryon chemical potential μ_B can describe the QCD matter at different phases.

Fig. 1.2 shows the overview of the QCD phase diagram. Theoretically, various QCD-based models predict that the phase transition is the first order phase transition in nonzero baryon chemical potential[3–6]. Lattice QCD calculations demonstrate that the phase transition between the hadronic phase and the QGP phase is a smooth crossover at vanishing baryon chemical potential[7]. So, if the first-order phase transition exists, there must be a critical point (CP) at the end of first order phase transition line towards the crossover region[8, 9]. But there is no experimental evidence to prove their existence[10]. Many scientists are working on study the QCD phase diagram and search for the critical point. Experimentally, to study the QCD phase diagram, we usually tune the colliding center of mass energy ($\sqrt{s_{\mathrm{NN}}}$) in heavy-ion collisions. The main goals of the heavy-ion collisions at the Relativistic Heavy-Ion Collider (RHIC) of the beam energy scan (BES) program at Brookhaven National Laboratory (BNL) are to map the QCD phase diagram and search for the critical point[11]. The BES program has been running since 2010 at $\sqrt{s_{\mathrm{NN}}}$ = 7.7, 11.5, 14.5, 19.6, 27, 39, 62.4 and 200 GeV. By changing the collision energy, the temperature and baryon chemical potential will vary accordingly, then the program can scan a large window in μ_B (25−422 MeV) and T in the phase diagram. Some experimental projects are in the preparation stage at facilities, such as the Facility for Anti-proton and Ion Research (FAIR) at GSI[12], the Nuclotron-based Ion Collider Facility (NICA) in Dubna[13] and High Intensity heavy-ion Accelerator Facility (HIAF) is under construction in Guangdong, which depict the QCD phase diagram of nuclear matter.

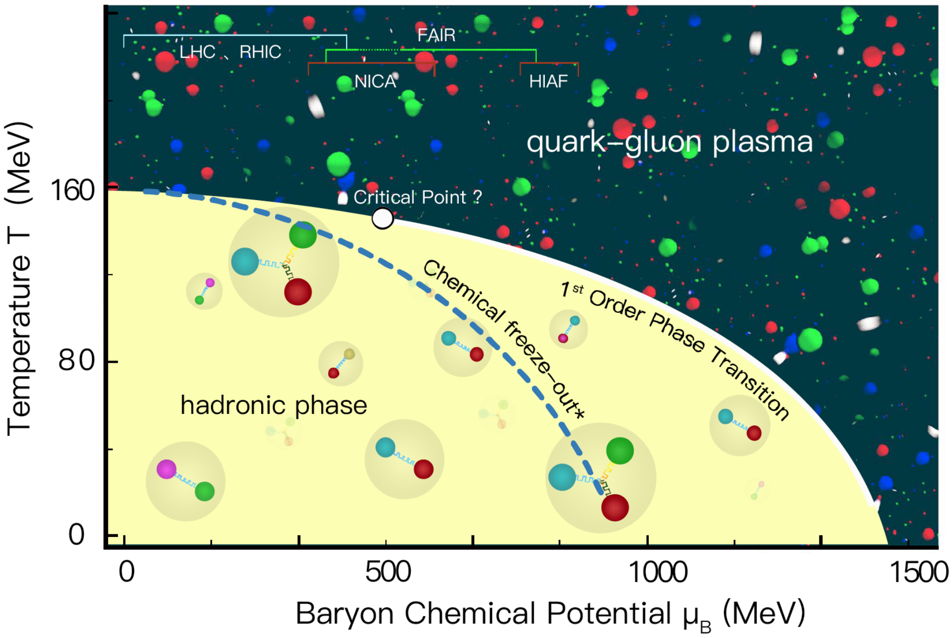

Fig. 1.2: (color online) Overview of QCD phase diagram. The X-axis is the baryon chemical potential μ_B, and the Y-axis is the temperature T.

1.3 Relativistic Heavy Ion Collisions

QGP are thought to be created after a few millionths of a second of the Big Bang, when the universe was filled with a hot soup at extremely high temperature. To recreate the conditions similar to those of the early universe, many powerful accelerators make collisions at ultra-relativistic energies between massive ions, such as gold or lead nuclei. Collisions between heavy atomic nuclei occurred near the speed of light.

Under the laboratory conditions, the two fast-moving nuclei collide each other like pancakes due to the Lorentz contraction in the beam direction. Two collided nuclei go through each other, and generate a large amount of energy, which is deposited in the central collision area. Nuclear matter is then produced, which experiences a pre-equilibrium stage, and then reaches the local thermal equilibrium. The quark-gluon plasma matter is considered to be formed at this stage, and expands like a relativistic fluid with the collision system expansion and cools down. When the temperature of the system go to the critical temperature, quarks and gluons are confined in hadrons again, which is hadronization process. After the fireball cools down, the quarks and gluons recombine to form hadrons. The produced hadrons continue to interact with each other, and may generate new hadrons via inelastic collisions. The temperature continues to cool down until the chemical freeze-out temperature is reached, inelastic collisions stop and the components of the hadron are fixed. After inelastic collision, elastic collisions takes place. When the kinetic freeze-out temperature is reached, the elastic collisions between the hadrons stops and the momentum spectrum is settled. After that the free hadrons fly to the detectors, and are observed by the detectors. The evolution of heavy ion collisions is shown in Fig. 1.3.

Although hadrons go through so many processes before reaching the detector, the process from hadron to QGP cannot be erased. Therefore, one of the important tasks in the study of QGP in heavy-ion collisions is to look at the distributions and fluctuations

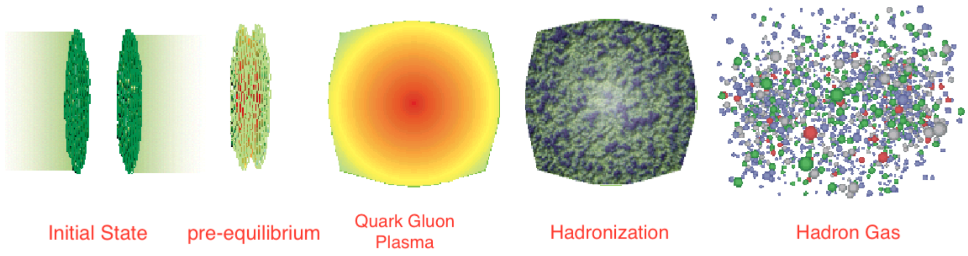

Fig. 1.3: (color online) Evolution of heavy ion collisions.

and correlations of the final state hadrons.

1.4 Critical Signature

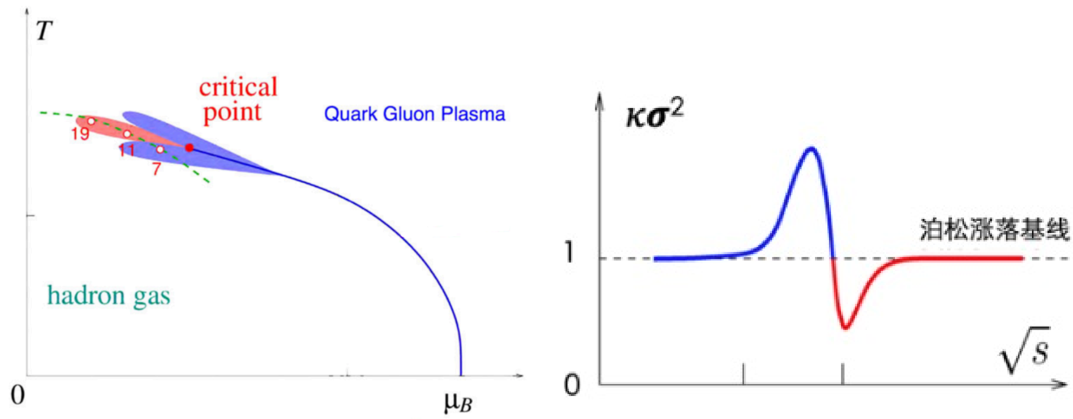

Fig. 1.4: (color online) A sketch of the phase diagram of QCD of the σ field with the freeze-out curve. The red region is negative, the blue region is positive. And the green dashed line is the chemical freeze-out lines in heavy-ion collisions. The solid blue line is the first-order phase transition and the red point is the so-called critical point. (Right) Normalized fourth order proton cumulant $\kappa\sigma^2$ as a function of collision energy or μ_B along the chemical freeze-out line. Figures are taken from[14–16].

Fig. 1.4 (left) shows the theoretical calculation about the critical point from σ model[14–16]. Fig. 1.4 (right) shows fourth order fluctuation $\kappa\sigma^2$ as a function of baryon chemical potential (μ_B). Due to the negative and positive critical contributions near the critical point, the $\kappa\sigma^2$ will show a non-monotonic energy or μ_B dependence with respect to the non-critical baseline. This might be the characteristic experimental signature of the critical point we are looking for in the heavy-ion collision experiment. The model describes the fluctuations based on the probability distribution of an order parameter field, which can be quantified by the critical mode σ. Its probability distribution $P(\sigma)$ can be expressed as:

$$P(\sigma) \sim exp\{-\Omega(\sigma)/T\} \tag{1.3}$$

where Ω is the free energy function of the field σ, which can be expanded into the exponential form and the expression of the gradients:

$$\Omega(\sigma) = \int d^3x[\frac{1}{2}(\bigtriangledown\sigma)^2 + \frac{m_\sigma^2}{2}\sigma^2 + \frac{\lambda_3}{3}\sigma^3 + \frac{\lambda_4}{4}\sigma^4 + \cdots] \tag{1.4}$$

where $m_\sigma = 1/\xi$ is the sigma-field screening mass, λ_3 and λ_4 are the interaction couplings.

In a system of volume V, the moments of the zero momentum mode is $\sigma_V \equiv \int d^3x\sigma(x)$, and the moments of the σ field are:

$$\langle\sigma_V^2\rangle = VT\xi^2 \tag{1.5}$$
$$\langle\sigma_V^3\rangle = 2\lambda_3VT\xi^6 \tag{1.6}$$
$$\langle\sigma_V^4\rangle_c = 6VT^3[2(\lambda_3\xi)^2 - \lambda_4]\xi^8 \tag{1.7}$$

where ξ is the correlation length and $\langle\sigma_V^4\rangle_c \equiv \langle\sigma_V^4\rangle - 3\langle\sigma_V^2\rangle^2$ is the fourth-order central moment (the fourth-order cumulant) of σ field.

Near the critical point, $\xi \to \infty$, and the couplings λ_3 and λ_4 also scale with ξ:

$$\lambda_3 = \widetilde{\lambda}_3T(T\xi)^{-3/2} \tag{1.8}$$
$$\lambda_4 = \widetilde{\lambda}_4(T\xi)^{-1} \tag{1.9}$$

where dimensionless couplings $\widetilde{\lambda}_3$ and $\widetilde{\lambda}_4$ are universal, do not depend on ξ. The coupling $\widetilde{\lambda}_3$ varies from 0 to about 8, and the coupling $\widetilde{\lambda}_4$ varies from about 4 to about 20, depending on the direction of approach to the critical point (crossover or the first-order transition side). Therefore, near the critical point, putting the equations Eq. 1.8 and Eq. 1.9 into Eq. 1.6 and Eq. 1.7, the moments of the σ field are:

$$\langle\sigma_V^3\rangle = 2\widetilde{\lambda}_3VT^{3/2}\xi^{4.5} \tag{1.10}$$
$$\langle\sigma_V^4\rangle_c = 6VT^2(2\widetilde{\lambda}_3 - \widetilde{\lambda}_4)\xi^7 \tag{1.11}$$

The kurtosis of the σ field is:

$$\kappa = \frac{\langle\sigma_V^4\rangle_c}{\langle\sigma_V^2\rangle^2} = \frac{6}{V}(2\widetilde{\lambda}_3 - \widetilde{\lambda}_4)\xi^3 \tag{1.12}$$

In Fig. 1.4, the value in the red region is negative, and the value in the blue region is positive. When approach the crossover region from the critical point along the chemical freeze-out line, according to the central limit theorem, the probability distribution of σ_V is Gaussian ($\langle\sigma_V^4\rangle_c = 0$). In the region near the critical point, $\langle\sigma_V^4\rangle_c$ is negative ($\langle\sigma_V^4\rangle_c < 0$). And the distribution of σ_V is skewed away from the crossover line, which makes the kurtosis positive ($\langle\sigma_V^4\rangle_c > 0$), the distribution becomes non-Gaussian. Therefore, when the chemical freeze-out line pass through the critical point from the crossover region, the probability distributions of the σ field change from Gaussian to non-Gaussian, and the corresponding fourth-order cumulant change from zero to negative and to positive. Obviously, the fluctuations of the σ field can not be measured directly experimentally, but they have effect on the multiplicities of observable particles, such as protons and kaons. When consider the influence of the critical point on the fluctuations of proton multiplicities, the fourth-order moment can be written as the terms of corresponding moment of the σ field[15]:

$$\langle(\delta N)^4\rangle_c = \langle N\rangle + \langle\sigma_V^4\rangle_c(\frac{gd}{T}\int_p \frac{n_p}{\gamma_p})^4 + \cdots \tag{1.13}$$

where $\gamma_p = (dE_p/dm)^{-1}$ is the relativistic gamma-factor of a particle with momentum p and mass m and $\langle N \rangle$ is the expected value of Poisson distribution. Near the critical point, the normalized fourth-order cumulant $(\langle (\delta N)^4 \rangle_c / \langle N \rangle)$will be smaller than 1. There is a non-monotonic collision energy dependence of kurtosis for multiplicity distributions along the chemical freeze-out line.

In the grand canonical ensemble system, the cumulants can be expressed in terms of the susceptibility of the system:

$$C_{ijk}^{BQS} = VT^3 \times \chi_{ijk}^{BQS} = VT^3 \times \frac{\partial^{i+j+k}(p/T^4)}{\partial \hat{\mu_B}^i \partial \hat{\mu_Q}^j \partial \hat{\mu_S}^k} \tag{1.14}$$

where $\hat{\mu_q} = \mu_q/T$, C_{ijk}^{BQS} is the diagonal and off-diagonal cumulants of conserved quantities (net-baryon B, net-charge Q and net-strangeness S). The results about the off-diagonal cumulants from UrQMD model[17] and STAR experiment have been published[18]. In this thesis, we only consider the diagonal cumulants, they can expressed as:

$$C_n^q = VT^3 \times \chi_n^q = VT^3 \times \frac{\partial^n (p/T^4)}{\partial (\mu_q)^n} \tag{1.15}$$

where χ_n^q is the n-th order susceptibility, V is the volume of the system, and q=B, Q, S. That is to say, the cumulants depend on the volume of the system.

1.5 Experimental Observables

We can measure the event-by-event particle multiplicity distributions of conserved quantities (net-baryon, net-charge and net-strangeness) in the heavy-ion collision experiment. Net-kaon and net-proton are proxies for net-strangeness and net-baryon, respectively. According to Eq. 1.10 and Eq. 1.11, higher-order moments of conserved quantities are more sensitive to correlation length (ξ)[15, 19–23]. For example, $\langle (\delta N)^3 \rangle \sim \xi^{4.5}$, $\langle (\delta N)^4 \rangle - 3\langle (\delta N)^2 \rangle \sim \xi^7$. Thus, we can use the higher-order moments of event-by-event multiplicity distributions of conserved charges as the experimental observables to study the QCD phase diagram and look for the QCD critical point[24–27].

The up to fourth-order cumulants can be written as the terms of event-by-event multiplicity distributions:

$$C_1 = \langle N \rangle \tag{1.16}$$
$$C_2 = \langle (\delta N)^2 \rangle \tag{1.17}$$
$$C_3 = \langle (\delta N)^3 \rangle \tag{1.18}$$
$$C_4 = \langle (\delta N)^4 \rangle - 3\langle (\delta N)^2 \rangle^2 \tag{1.19}$$

where N is the measured event-by-event particle number, and $\langle N \rangle$ is the mean value over the total events. $\delta N = N - \langle N \rangle$ is the difference of N and its mean value. The moments can also be expressed in terms of cumulants:

$$M = C_1 \tag{1.20}$$
$$\sigma^2 = C_2 \tag{1.21}$$
$$S = \frac{C_3}{(C_2)^{3/2}} \tag{1.22}$$
$$\kappa = \frac{C_4}{C_2^2} \tag{1.23}$$

Cumulant ratios are constructed to cancel the volume dependence and can also be expressed in terms of the products of moments $\kappa\sigma^2$ and $S\sigma$, and can be directly related to theoretical calculations:

$$\frac{C_3}{C_2} = S\sigma = \frac{\chi_3^q}{\chi_2^q} \tag{1.24}$$

$$\frac{C_4}{C_2} = \kappa\sigma^2 = \frac{\chi_4^q}{\chi_2^q} \tag{1.25}$$

Fig. 1.5 shows energy dependence of cumulant ratios ($\sigma^2/M, S\sigma$/Skellam and $\kappa\sigma^2$) of net-charge, net-kaon and net-proton multiplicity distributions for Au+Au collisions at $\sqrt{s_{\rm NN}}$ = 7.7−200 GeV for twocentralities (0 − 5% and 70 − 80%) within mid-rapidity window. We observed a non-monotonic energy dependence of $\kappa\sigma^2$ in most central Au+Au collisions for net-proton.

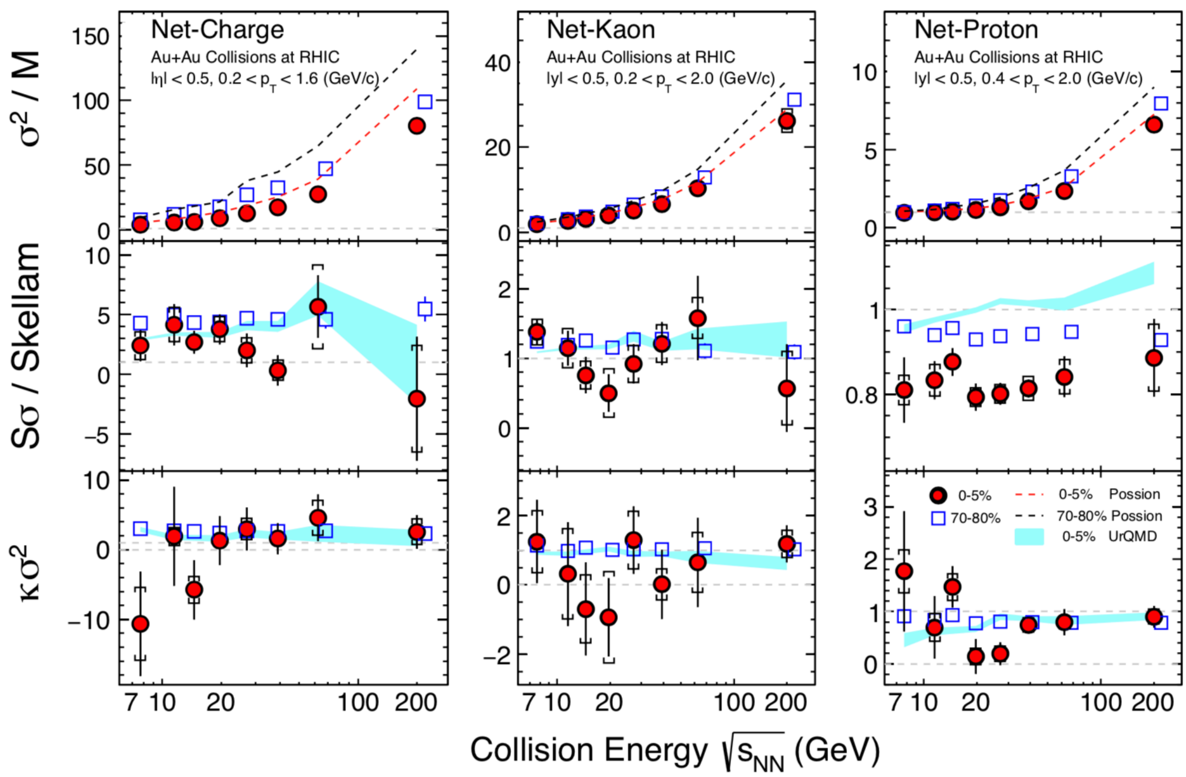

Fig. 1.5: (color online) Energy dependence of cumulant ratios (σ^2/M, $S\sigma$/Skellam and $\kappa\sigma^2$) of net-charge, net-kaon and net-proton multiplicity distributions for Au+Au collisions at $\sqrt{s_{\rm NN}}$ = 7.7−200 GeV for two centralities (0 − 5% and 70 − 80%) within mid-rapidity window[28–31].

1.6 Definition of Statistical Observables

1.6.1 Moments

In probability theory and statistics, the moment-generating function $M_X(t)$ is the mean value of the random variable e^{tX}:

$$
\begin{aligned}
M_X(t) = E(e^{tX}) &= 1 + tEX + \frac{t^2}{2!}EX^2 + \frac{t^3}{3!}EX^3 + \cdots + \frac{t^n}{n!}EX^n \\
&= 1 + tm_1 + \frac{t^2}{2!}m_2 + \frac{t^3}{3!}m_3 + \cdots + \frac{t^n}{n!}m_n
\end{aligned} \tag{1.26}
$$

where $e^{tX} = 1+tX+\frac{(tX)^2}{2!}+\frac{(tX)^3}{3!}+\cdots+\frac{(tX)^n}{n!}$ is the series expansion of e^{tX} and $M_X(0) = 1$. Thus, the n-th moments about zero m_n of a random variable X is the n-th derivative of $M_X(t)$ at $t = 0$:

$$
m_n = \frac{d^n M_X(t)}{dt^n}|_{t=0} = M_X^{(n)}(0) = EX^n = \langle X^n \rangle \tag{1.27}
$$

The n-th central moment μ_n of a random variable X is the n-th moment about its mean value:

$$
\mu_n \equiv E[(X - EX)^n], \tag{1.28}
$$

where $\mu_1 = 0$ and $M = m_1 = EX = \langle X \rangle$ is the mean value of the random variable $\langle X \rangle$. From Eq. A.2–Eq. A.4, the normalized higher-order central moments are:

$$
\sigma^2 = \mu_2 = \langle (X - \langle X \rangle)^2 \rangle \tag{1.29}
$$

$$
S = \frac{\mu_3}{\sigma^3} = \frac{\langle (X - \langle X \rangle)^3 \rangle}{\sigma^3} \tag{1.30}
$$

$$
\kappa = \frac{\mu_4}{\sigma^4} - 3 = \frac{\langle (X - \langle X \rangle)^4 \rangle}{\sigma^4} - 3 \tag{1.31}
$$

Usually, the first order moment around zero is the mean value of probability distribution; the higher-order central moments are used to describe the property of a probability distribution. For example, the second central moment is the variance $Var(X)$, which is used to describe the width of a distribution; Skewness S is the normalized third central moment, which is used to describe the asymmetry of a distribution; and Kurtosis κ is the normalized forth central moment, which is a descriptor of the sharpness of a probability distribution.

1.6.2 Cumulants

The cumulant-generating function $K_X(t)$ of a random variable X is the natural logarithum of the moment-generating function $M_X(t)$:

$$
K_X(t) = logM_X(t) = logE(e^{tX}), \quad K_X(0) = 0 \tag{1.32}
$$

Thus, the cumulants can be expressed in the n-th derivative of $K_X(t)$ at $t = 0$:

$$
C_n = K_X^{(n)}(0) = \frac{d^n K_X(t)}{dt^n}|_{t=0} = \frac{d^n}{dt^n} logM_X(t)|_{t=0} \tag{1.33}
$$

From Eq. A.10−Eq. A.12, cumulants can be written as:

$$C_1 = \langle X\rangle \tag{1.34}$$
$$C_2 = \langle X^2\rangle - \langle X\rangle^2 = \langle(\delta X)^2\rangle \tag{1.35}$$
$$C_3 = \langle X^3\rangle - 3\langle X^2\rangle\langle X\rangle + 2\langle X\rangle^3 = \langle(\delta X)^3\rangle \tag{1.36}$$
$$\begin{aligned} C_4 &= \langle X^4\rangle - 4\langle X^3\rangle\langle X\rangle - 3\langle X^2\rangle^2 + 12\langle X^2\rangle\langle X\rangle^2 - 6\langle X\rangle^4 \\ &= \langle(\delta X)^4\rangle - 3\langle(\delta X)^2\rangle^2 \end{aligned} \tag{1.37}$$

Combine Eq. 1.29−Eq. 1.31 and Eq. 1.34−Eq. 1.37, moments can be written as the terms of cumulants:

$$M = C_1, \quad \sigma^2 = C_2, \quad S = \frac{C_3}{(C_2)^{\frac{3}{2}}}, \quad \kappa = \frac{C_4}{C_2^2} \tag{1.38}$$

And the relation between moment products and cumulant ratios is:

$$\sigma^2/M = \frac{C_2}{C_1}, \quad S\sigma = \frac{C_3}{C_2}, \quad \kappa\sigma^2 = \frac{C_4}{C_2} \tag{1.39}$$

The cumulant ratios can cancel the volume dependence on the system, which can't be directly to be measured. Thus the cumulant ratios are used to be experimental observables. From Eq. A.18 − Eq. A.21, the moments can be expressed in terms of cumulants:

$$m_1 = C_1 \tag{1.40}$$
$$m_2 = C_2 + C_1^2 \tag{1.41}$$
$$m_3 = C_3 + 3C_2C_1 + C_1^3 \tag{1.42}$$
$$m_4 = C_4 + 4C_3C_1 + 3C_2^2 + 6C_2C_1^2 + C_1^4 \tag{1.43}$$

and vice versa, from Eq. A.13 − Eq. A.16, the cumulants can be expressed in terms of moments:

$$C_1 = m_1 \tag{1.44}$$
$$C_2 = m_2 - m_1^2 \tag{1.45}$$
$$C_3 = m_3 - 3m_2m_1 + 2m_1^3 \tag{1.46}$$
$$C_4 = m_4 - 4m_3m_1 - 3m_2^2 + 12m_2m_1^2 - 6m_1^4 \tag{1.47}$$

From Eq. 1.44−Eq. 1.47, we can get the recursion formula for cumulants:

$$C_n = m_n - \sum_{k=1}^{n-1} C_{n-1}^{k-1} C_k m_{n-k} \tag{1.48}$$

1.6.3 Properities of Cumulants

The cumulant-generating function $K_{X+Y}(t)$ for two independent random variables X and Y from Eq. 1.32 is:

$$\begin{aligned} K_{X\pm Y}(t) &= logE[e^{t(X\pm Y)}] \\ &= logEe^{tX}Ee^{\pm tY} \\ &= logEe^{tX} + logEe^{\pm tY} \\ &= K_X(t) + K_Y(\pm t) \end{aligned} \tag{1.49}$$

Then, the $n-th$ derivative of cumulant-generating function is given by:

$$\frac{d^n}{dt^n}K_{X\pm Y}(t) = \frac{d^n}{dt^n}K_X(t) + (\pm 1)^n \frac{d^n}{dt^n}K_Y(-t) \tag{1.50}$$

That is to say, the sum of the various order cumulants of two independent random variables is the sum of the corresponding cumulants. Thus, the $n-th$ cumulants of sum and difference of two random variables are given by:

$$C_{X\pm Y} = C_X + (\pm 1)^n C_Y \tag{1.51}$$

1.6.4 Factorial Moments

The factorial moment generating function $H_X(t)$ is the mean value of t^X:

$$H_X(t) = E[t^X] = \langle t^X \rangle, \quad H_X(1) = 1 \tag{1.52}$$

Thus, the n-th factorial moment F_n of a random variable X is given by the n-th derivative of factorial moment generating function $H_X(t)$ at t=1:

$$F_n = \frac{d^n}{dt^n}H_X(t)|_{t=1} = \frac{d^n}{dt^n}\langle t^X \rangle|_{t=1} = H_X^{(n)}(1) \tag{1.53}$$

From Eq. A.22−Eq. A.25, we can obtain the various order factorial moments:

$$F_1 = \langle X \rangle \tag{1.54}$$
$$F_2 = \langle X(X-1) \rangle = \langle X^2 \rangle - \langle X \rangle \tag{1.55}$$
$$F_3 = \langle X(X-1)(X-2) \rangle = \langle X^3 \rangle - 3\langle X^2 \rangle + 2\langle X \rangle \tag{1.56}$$
$$F_4 = \langle X(X-1)(X-2)(X-3) \rangle = \langle X^4 \rangle - 6\langle X^3 \rangle + 11\langle X^2 \rangle - 6\langle X \rangle \tag{1.57}$$

Therefore, it's easy to summarize the recursion formula for F_n[32]:

$$F_n = \langle X(X-1)(X-2)\cdots(X-n+1) \rangle = \langle \frac{X!}{(X-n)!} \rangle \tag{1.58}$$

1.6.5 Correlation Functions

The n-th correlation function κ_n is given by n-th derivatives from the logarithm of factorial moment generating function $H_X(t)$ [33, 34]:

$$\kappa_n = \frac{d^n}{dt^n} lnH_X(t)|_{t=1} \tag{1.59}$$

and from Eq. A.26−Eq. A.29, correlation functions can be written in terms of the factorial moments:

$$\kappa_1 = F_1 \tag{1.60}$$
$$\kappa_2 = F_2 - F_1^2 \tag{1.61}$$
$$\kappa_3 = F_3 - 3F_2F_1 + 2F_1^3 \tag{1.62}$$
$$\kappa_4 = F_4 - 4F_3F_1 - 3F_2^2 + 12F_2F_1^2 - 6F_1^4 \tag{1.63}$$

From Eq. 1.33, cumulants can also be written in terms of the factorial moments[34, 35]:

$$C_1 = F_1 \tag{1.64}$$

$$C_2 = F_2 + F_1 - F_1^2 \tag{1.65}$$

$$C_3 = F_3 + 3F_2 + F_1 - 3F_1^2 - 3F_2F_1 + 2F_1^3 \tag{1.66}$$

$$\begin{aligned} C_4 = {} & F_4 + 6F_3 + 7F_2 + F_1 - 4F_3F_1 - 18F_2F_1 - 7F_1^2 + 12F_2F_1^2 \\ & + 12F_1^3 - 3F_2^2 - 6F_1^4 \end{aligned} \tag{1.67}$$

Thus, we can express the correlation functions κ_n in terms of the cumulants C_n with the mean particle number $\langle X \rangle$:

$$\kappa_1 = C_1 \tag{1.68}$$

$$\kappa_2 = C_2 - \langle X \rangle \tag{1.69}$$

$$\kappa_3 = C_3 - 3C_2 + 2\langle X \rangle \tag{1.70}$$

$$\kappa_4 = C_4 - 6C_3 + 11C_2 - 6\langle X \rangle \tag{1.71}$$

and vice versa,

$$C_1 = \kappa_1 \tag{1.72}$$

$$C_2 = \kappa_2 + \langle X \rangle \tag{1.73}$$

$$C_3 = \kappa_3 + 3\kappa_2 + \langle X \rangle \tag{1.74}$$

$$C_4 = \kappa_4 + 6\kappa_3 + 7\kappa_2 + \langle X \rangle \tag{1.75}$$

As we have the various order cumulants of (anti-)proton in our analysis, it's straightforward to get the correlation functions according to the Eq. 1.68–Eq. 1.71. It should be noted that the relation between correlation functions and cumulants is only valid for a single source, such as protons or anti-protons[34]. Here we're only interested in the multi-proton correlations, so we consider proton correlations only.

1.7 Statistical Baseline

1.7.1 Binomial Distribution

In probability theory and statistics, the probability distribution of the binomial distribution (BD) of random variable $X = k$ is:

$$P(X = k) = B(k; N, p) = C_N^k p^k (1-p)^{N-k} \tag{1.76}$$

where k is the number of success and p is the probability of success in a sequence of n independent trails. And $C_N^k = \frac{N!}{k!(N-k)!}$ is the binomial coefficient, which is the name of the distribution. Therefore, the binomial distribution is used to describe the number of successes in a sequence of N trails. The moment-generating function of BD is:

$$\begin{aligned} M_B(t) &= \sum_k e^{kt} B(k; N, p) = \sum_k \frac{N!}{k!(N-k)!} p^k e^{kt} (1-p)^{N-k} \\ &= (1 - p + pe^t)^N \end{aligned} \tag{1.77}$$

and the cumulant-generating function of BD is:

$$K_B(t) = lnM_B(t) = Nln(1 - p + pe^t) \tag{1.78}$$

then, the n-th moments of BD can be expressed the n-th derivative of $M_B(t)$ at $t = 0$:

$$m_n = M_B^{(n)}(0) = \frac{d^n M_B(t)}{dt^n}|_{t=0} \tag{1.79}$$

Thus, the n-th cumulants of BD can be expressed the n-th derivative of $K_B(t)$ at $t = 0$:

$$C_n = K_B^{(n)}(0) = \frac{d^n K_B(t)}{dt^n}|_{t=0} \tag{1.80}$$

From Eq. A.31−Eq. A.35, various order moments of BD are given by:

$$m_1 = Np \tag{1.81}$$

$$m_2 = N^2p^2 + Np(1 - p) \tag{1.82}$$

$$m_3 = N^3p^3 - 3N^2p^2(1 - p) + Np(1 - 3p + 2p^2) \tag{1.83}$$

$$\begin{aligned} m_4 = {} & N^4p^4 - 6N^3p^3(1 - p) + N^2p^2(7 - 18p + 11p^2) \\ & + Np(1 - 7p + 12p^2 - 6p^3) \end{aligned} \tag{1.84}$$

From Eq. A.36−Eq. A.39, various order of cumulants of BD are given by:

$$C_1 = Np \tag{1.85}$$

$$C_2 = Np(1 - p) \tag{1.86}$$

$$C_3 = Np(1 - p)(1 - 2p) = Np(1 - 3p + 2p^2) \tag{1.87}$$

$$C_4 = Np(1 - p)(1 - 6p + 6p^2) = Np(1 - 7p + 12p^2 - 6p^3) \tag{1.88}$$

The mean value and variance of the BD are:

$$\mu = Np, \quad \epsilon = \frac{\sigma^2}{\mu} = (1 - p) \tag{1.89}$$

Then, cumulants of BD can be written in terms of μ and ϵ:

$$C_1 = \mu \tag{1.90}$$

$$C_2 = \mu\epsilon \tag{1.91}$$

$$C_3 = \mu\epsilon(2\epsilon - 1) \tag{1.92}$$

$$C_4 = \mu\epsilon(6\epsilon^2 - 6\epsilon - 1) \tag{1.93}$$

From Eq. 1.89, we can see $0 < \epsilon < 1$. And from Eq. 1.92, $C_2 = \mu\epsilon < \mu$, that is to say, the variance of BD is smaller than its mean value.

1.7.2 Poisson Distribution

In probability theory and statistics, the probability of the Poisson distribution of random variable $X = k$ with parameters λ is given by:

$$P_\lambda(k) = e^{-\lambda}\frac{\lambda^k}{k!} \tag{1.94}$$

The moment-generating function of Poisson distribution is:

$$M_P(t) = \sum_{k=0}^{\infty} e^{kt} e^{-\lambda} \frac{\lambda^k}{k!} = e^{-\lambda} \sum_{k=0}^{\infty} \frac{(\lambda e^t)^k}{k!} e^{\lambda(e^t-1)} \tag{1.95}$$

The cumulant-generating function of Poisson distribution is:

$$K_P(t) = lnM_P(t) = \lambda(e^t - 1) \tag{1.96}$$

So, the cumulants can be expressed as follows:

$$C_n = \lambda \frac{d^n}{dt^n}(e^t - 1)|_{t=0} = \lambda e^t|_{t=0} = \lambda \tag{1.97}$$

And the various moments and moment products can be expressed as:

$$M = \lambda, \quad \sigma = \sqrt{\lambda}, \quad S = \frac{1}{\sqrt{\lambda}}, \quad \kappa = \frac{1}{\lambda} \tag{1.98}$$

$$S\sigma = \kappa\sigma^2 = 1 \tag{1.99}$$

Therefore, the various order cumulants of Poisson distribution are the same, and the baseline of Poisson distribution for $\kappa\sigma^2$ and $S\sigma$ are unity.

1.7.3 Skellam Distribution

The Skellam distribution is the distribution of the difference of the two variables follow Poisson distribution. The probability density function of the Skellam distribution are defined as:

$$P(k; \lambda_1, \lambda_2) = e^{-(\lambda_1+\lambda_2)} (\frac{\lambda_1}{\lambda_2})^{k/2} I_k(2\sqrt{\lambda_1\lambda_2}) \tag{1.100}$$

where $I_k(z)$ is the modified Bessel function of the first kind, and λ_1, λ_2 are the mean value of the two idenpendent Poisson distributions.

The moment-generating function of Skellam distribution is:

$$\begin{aligned}
M_{X,Y}(t) &= \sum_k e^{tk} P(k; \lambda_1, \lambda_2) \\
&= \sum_k e^{tk} e^{-(\lambda_1+\lambda_2)} (\frac{\lambda_1}{\lambda_2})^{k/2} I_k(2\sqrt{\lambda_1\lambda_2}) \\
&= e^{-(\lambda_1+\lambda_2)} \sum_k (e^t \sqrt{\frac{\lambda_1}{\lambda_2}})^k I_k(2\sqrt{\lambda_1\lambda_2}) \\
&\Downarrow \sum_k I_k(z) m^k = e^{(\frac{z}{2})(m+\frac{1}{m})} \qquad (1.101) \\
&= e^{-(\lambda_1+\lambda_2)} e^{\sqrt{\lambda_1\lambda_2}(e^t\sqrt{\frac{\lambda_1}{\lambda_2}} + e^{-t}\sqrt{\frac{\lambda_2}{\lambda_1}})} \\
&= e^{-(\lambda_1+\lambda_2)+\lambda_1 e^t + \lambda_2 e^{-t}} \qquad (1.102)
\end{aligned}$$

The cumulant-generating function of Skellam distribution is:

$$K_{X,Y}(t) = lnM_{X,Y}(t) = -(\lambda_1 + \lambda_2) + \lambda_1 e^t + \lambda_2 e^{-t} \tag{1.103}$$

Then the various order cumulants of the Skellam distribution are given by:

$$C_n = \frac{d^n}{dt^n} K_{X,Y}(t)|_{t=0} = \lambda_1 e^t|_{t=0} + (-1)^n \lambda_2 e^{-t}|_{t=0} = \lambda_1 + (-1)^n \lambda_2 \tag{1.104}$$

which also can be obtained from Eq. 1.51. The various order moments and moment products of the Skellam distribution are:

$$M = \lambda_1 - \lambda_2 \tag{1.105}$$
$$\sigma = \sqrt{\lambda_1 + \lambda_2} \tag{1.106}$$
$$S = \frac{\lambda_1 - \lambda_2}{(\lambda_1 + \lambda_2)^{\frac{3}{2}}} \tag{1.107}$$
$$\kappa = \frac{1}{\lambda_1 + \lambda_2} \tag{1.108}$$
$$S\sigma = \frac{C_3}{C_2} = \frac{\lambda_1 - \lambda_2}{\lambda_1 + \lambda_2} \tag{1.109}$$
$$\kappa\sigma^2 = \frac{C_4}{C_2} = 1 \tag{1.110}$$

Therefore, the even and odd order cumulants of Skellam distribution are the sum and difference of cumulants of the two random variables, and the baseline of Skellam distribution for $\kappa\sigma^2$ is unity.

1.7.4 Gaussian Distribution

The probability density function of Gaussian distribution of random variable $X = x$ is:

$$G(x; \mu, \sigma^2) = \frac{1}{\sqrt{2\pi\sigma^2}} e^{-\frac{(x-\mu)^2}{2\sigma^2}} \tag{1.111}$$

where μ and σ are the mean and standard deviation of the distribution.

The moment-generating function of Gaussian distribution is:

$$\begin{aligned} M_G(t) = Ee^{tx} &= \int_{-\infty}^{\infty} e^{tx} \frac{1}{\sqrt{2\pi\sigma^2}} e^{-\frac{(x-\mu)^2}{2\sigma^2}} dx \\ &= e^{\mu t + \frac{1}{2}\sigma^2 t^2} \end{aligned} \tag{1.112}$$

The cumulant-generating function of Gaussian distribution is:

$$K_G(t) = lnM_G(t) = \mu t + \frac{1}{2}\sigma^2 t^2 \tag{1.113}$$

So the cumulants can be written as:

$$C_1 = \mu \tag{1.114}$$
$$C_2 = \sigma^2 \tag{1.115}$$
$$C_n = 0 \tag{1.116}$$

Only the first two cumulants are non-zero, the higher-order cumulants are zero. Non-zero skewness and kurtosis indicates non-Gaussianity. That is to say, the measured higher-order cumulants are "non-Gaussianity".

Chapter 2

The STAR Experiment

2.1 The Relativistic Heavy-Ion Collider (RHIC)

Fig. 2.1 is the overview picture of the Relativistic Heavy Ion Collider (RHIC) at Brookhaven National Laboratory (BNL)[36]. The RHIC rings consists of two independent rings called "Blue" and "Yellow" rings, which carry heavy ions and proton in opposite direction. It accelerates heavy ions up to a top energy of 100 GeV per nucleon. A large number of particles are generated in each collision. There are six intersection points, and four different detectors (STAR, PHENIX, BRAHMS and PHOBOS) were located at four of the intersection points. The Solenoid Track at RHIC (STAR) detector is located at 6 o'clock of RHIC and is the only detector that's still operating.

2.2 The STAR Detector

STAR was constructed to measure many observables, and to understand the space-time evolution of heavy ion collisions. Further more, to investigate the properties of QGP and search for the critical point. STAR has many sub-detectors, such as Time Projection Chamber (TPC)[37], Time Of Flight (TOF)[38–40], Vertex Position Detector (VPD)[41]. Each sub-detector has its specific function, such as TPC can be used to track tracing, measure momentum of charged particle at lower transverse momentum range, TOF can identify charged particles at higher transverse momentum range, and VPD can measure the primary vertex position, which is suitable for the event-by-event features in the heavy ion collisions. Fig. 2.2 is the schematic diagram of the STAR detector.

2.2.1 Time Projection Chamber (TPC)

TPC is the main tracking detector at STAR, and is used to track the charged particles. TPC can reconstruct the vertex, measure momentum and identify charged particles with ionization energy loss ($d\mathrm{E}/dx$). It has a large acceptance with pseudo-rapidity of $-1 < \eta < 1$ and full azimuthal coverage ($0 < \phi < 2\pi$). Thus, the full azimuthal angles and different multiplicity will be covered. The transverse momentum of proton can be identified from 100 MeV/c to 1 GeV/c, and transverse momentum of charged particles can be measured over a range of 100 MeV/c to 30 GeV/c. The schematic profile of TPC is shown in Fig. 2.3. TPC is located in a solenoidal magnet with a uniform magnet field of $|\mathrm{B}| = 0.5$ T along the beam pipe (z-axis) direction. It's a cylinder with a diameter of 4

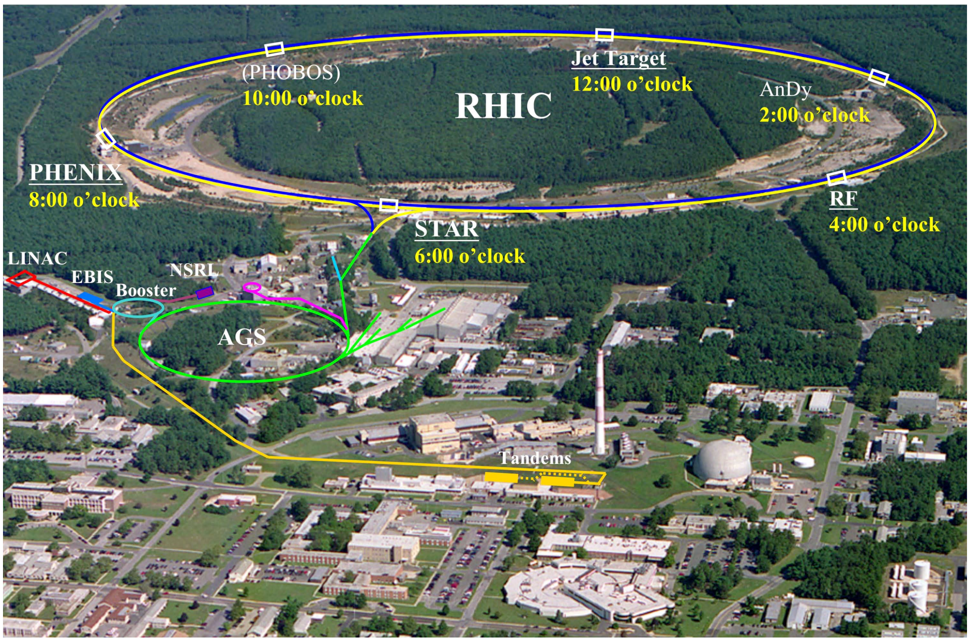

Fig. 2.1: (color online) The overview of the Relativistic Heavy Ion Collider (RHIC) at Brookhaven National Laboratory (BNL).

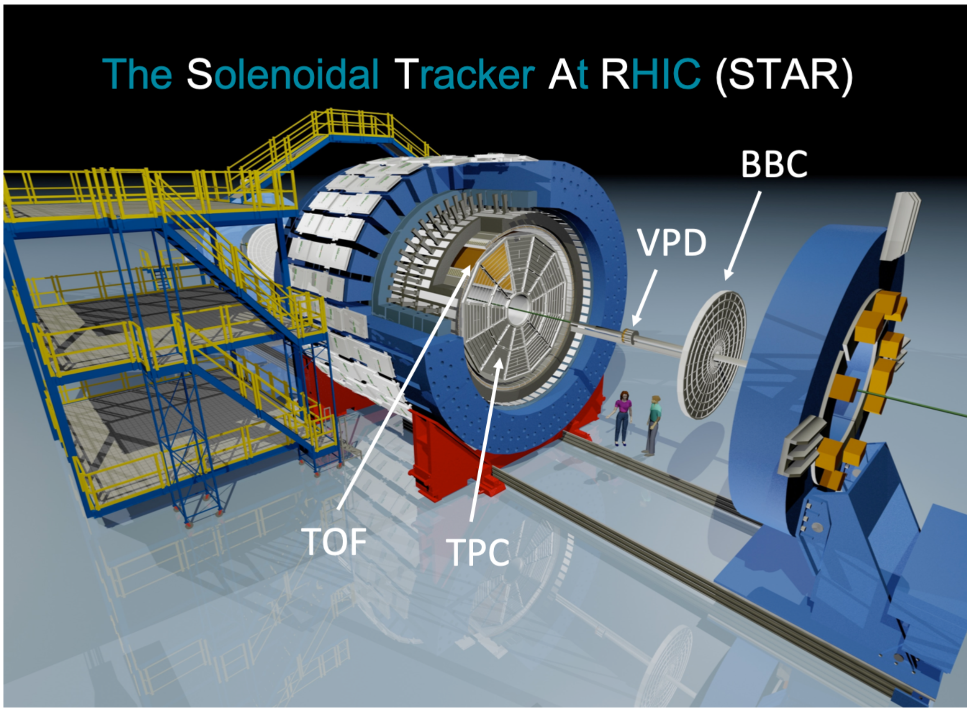

Fig. 2.2: (color online) The schematic diagram of the STAR detector. The figure is taken from [42].

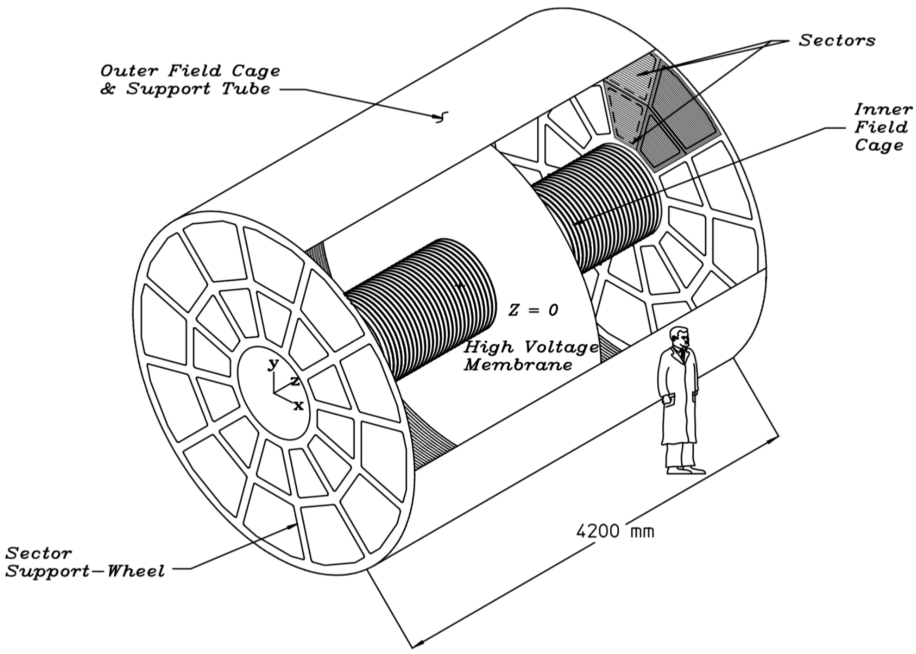

Fig. 2.3: (color online) The schematic profile of STAR TPC detector. The figure is taken from [37].

m and 4.2 m long (TPC spans from z = -210 cm to z = 210 cm). The inner field cage is 50 cm from the center of the beam pipe and the outer field cage is 200 cm from the center of the beam pipe. The central membrane (CM) is located at the center of TPC (z = 0) and operates at a high voltage of 28 kV. TPC is filled with P10 gas (10% methane CH_4 and 90% argon Ar) and an uniform electric field of $|E| = 135V/$cm. The uniform electric field of TPC are generated by the central membrane (CM), the outer field cage, the inner field cage and the end caps. The collisions take place near the center of TPC. When the charged particles transverse the TPC, will interact with the gas. The secondary electrons released by the ionized gas atoms will drift to the readout end caps at the bottom of TPC under the uniform electric field, and the track of particles will be reconstructed with high resolution. The drift velocity of the gas in the TPC is typically 5.45 cm/μs. The readout system is based on Multi-Wire Proportional Chambers (MWPC) with readout pads.

The anode pad plane with one full sector of TPC is shown in Fig. 2.4. The inner sub-sector is on the right and it has small pads arranged in widely spaced rows. The outer sub-sector is on the left and it is densely packed with larger pads. The inner sector can detect the particles with lower momentum. The inner sector has 13 pad rows and the outer sector has an additional 32 pad rows, so there is 45 pad rows in total.

The induced signals in a single pad row can determine the x and y coordinates of electron clusters. Suppose the signals are Gaussian, the position on the x-axis and the width of the signal σ with pad h_2 centered at y = 0 are given by:

$$x = \frac{\sigma^2}{2w} ln(\frac{h_3}{h_1}) \tag{2.1}$$

$$\sigma^2 = \frac{w^2}{ln(h_2^2/h_1 h_3)}, \tag{2.2}$$

where h_1, h_2 and h_3 are amplitudes on three pads and w is the pad width. When a track pass through the pad rows at large angles, it deposits ionization on many pads, and

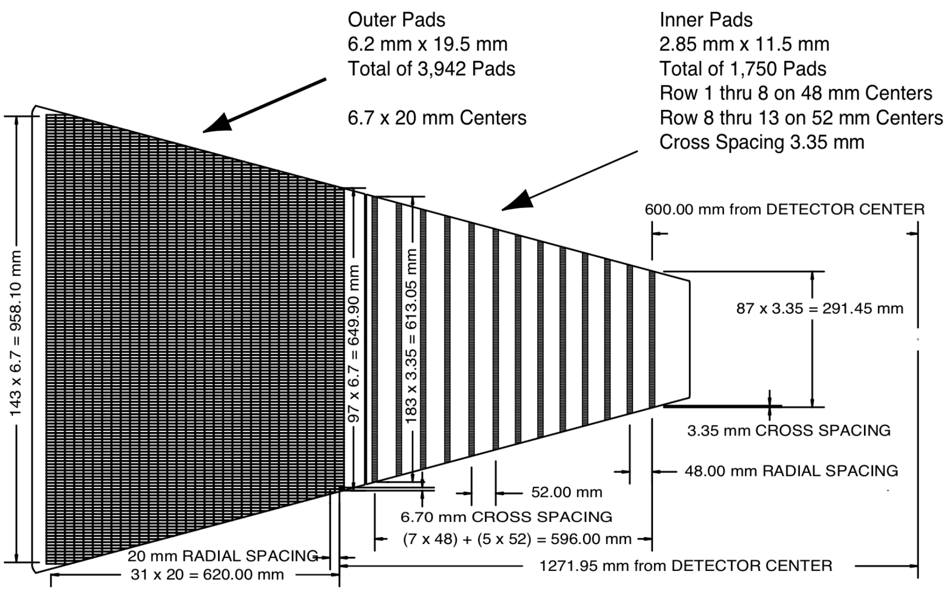

Fig. 2.4: (color online) The anode pad plane with one full sector. The inner sub-sector is on the right and the outer sub-sector is on the left. The figure is taken from [37].

any three adjacent pads will have signals with similar amplitudes. The crossing angle is the angle between the particle momentum and the pad row direction. Thus the weighted mean algorithm will be better. The drift velocity divided by the drift time of the electrons from the original point to the anode on the endcap can determine the position on the z-coordinate.

Assume the initial primary vertex is located at the center of TPC, the reconstructed tracks will start from the outermost hit points in the TPC, and then project inward. The hit points in the pad rows are formed into reconstructed tracks, which are known as the global tracks. The primary interaction vertex is fit from the global tracks with at least ten hits. The primary vertex is found by considering all of the tracks reconstructed in the TPC and then extrapolating them back to the origin. The global average is the vertex position[37]. For each global track, the closest distance to the primary vertex is called the distance of closest approach (d_{ca}). The global tracks refitted with $d_{ca} < 3$ cm including the primary vertex are the primary tracks. In our analysis, we will discard the tracks with $d_{ca} > 3$ cm and consider the primary tracks only, which will help determine the momentum of the particle tracks.

The ionized energy loss(dE$/dx$) is used to identify charged particles. Bethe-Bloch formula[43] gives the mean rate of energy loss for a charged particle:

$$-\left\langle \frac{dE}{dx} \right\rangle = 2\pi N_a r_e^2 m_e c^2 \rho \frac{Z}{A} \frac{z^2}{\beta^2} \left[ln \left(\frac{2 m_e \gamma^2 v^2 W_{max}}{I} \right) - 2\beta^2 \right] \tag{2.3}$$

with $2\pi N_a r_e^2 m_e c^2 = 0.1535$ MeV cm$^2/g$ and $\gamma = 1/\sqrt{1-\beta^2} = 1/\sqrt{1-(v/c)^2}$.

m_e : electron mass	W_{max} : maximum energy transfer in a single collision
I: mean excitation potential	z: charge of incident particle in units of e
ρ : density of absorbing material	Z: atomic number of absorbing material
r_e : classical electron radius	A: atomic weight of absorbing material
N_a : Avogadro's number	

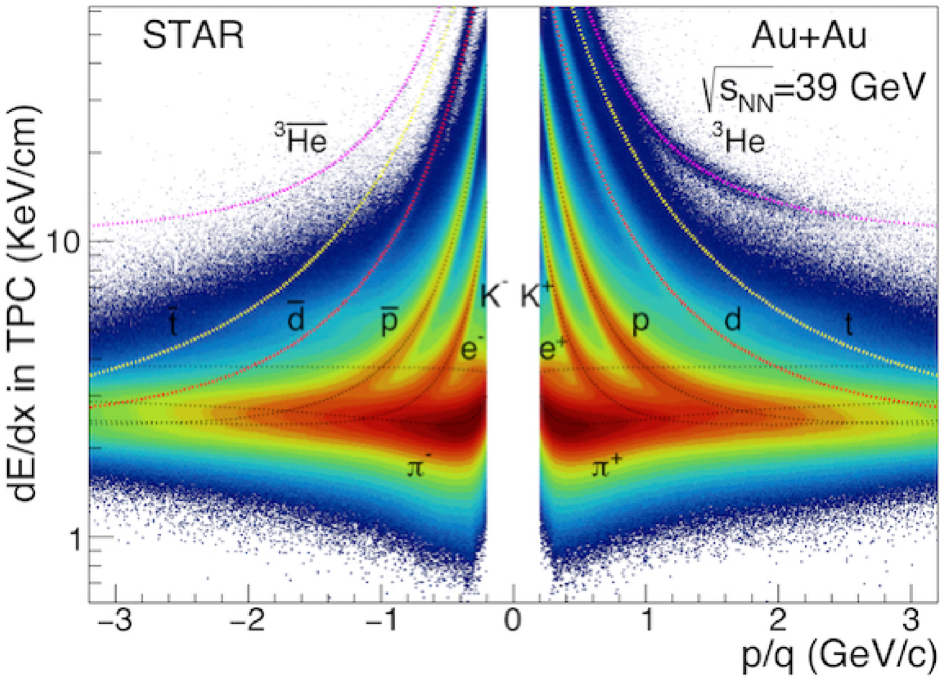

Fig. 2.5: (color online) The ionization energy loss distribution of charged particles at $\sqrt{s_{\mathrm{NN}}}$ = 39 GeV. The solid lines are from the Bichsel functions.

In the calculation, the energy transfer is parameterized in terms of momentum transfer rather than impact parameters. Of course, this is more realistic because momentum transfer is a measurable quantity, whereas the impact parameter sits. Different kinds of particles with the same momentum have different ionization energy losses ($d\mathrm{E}/dx$).

However, the Bethe-Bloch formula gives an inaccurate representation of energy dependence, which is different from that of the Bichsel functions ($d\mathrm{E}/dx/\mathrm{x}$)[44]. In the STAR experiment, the Bichsel functions are used to fit the $d\mathrm{E}/dx$. the average $d\mathrm{E}/dx$ cannot be accurately measured experimentally because of the Landau distribution with a long tail. Thus a 70% truncated mean (typically 30% is removed before it's averaged) is used to measure the most probable $d\mathrm{E}/dx$.

Fig. 2.5 shows the the ionization energy loss ($d\mathrm{E}/dx$) distributions of charged particles as a function of rigidity at $\sqrt{s_{\mathrm{NN}}}$ = 39 GeV. These lines are fitted by the Betha-Bloch function. We can see that the proton can be clearly identified at momentum below 1 GeV/c. But they can not be identified clearly above 1 GeV/c due to the merged bands. In order to clearly identify charged particles at higher momentum range, we add the Time of Flight detector.

2.2.2 Time of Flight (TOF)

As is shown before, TPC can identify the charged particles within p $\leq$ 1 GeV/c, but not for particles in p $\geq$ 1 GeV/c. However, the design of TOF detector can achieve this goal.

The TOF detector is located outside of the TPC. Fig. 2.6 shows the geometry of TOF trays, modules and pads at STAR. There are 120 trays mounted on the east and west sides of the TPC (60 on each side), with pseudo-rapidity coverage $-1 < \eta < 1$ and full azimuthal angles. Every TOF tray is consisted of 32 Multi-gap Resistive Plate Chamber

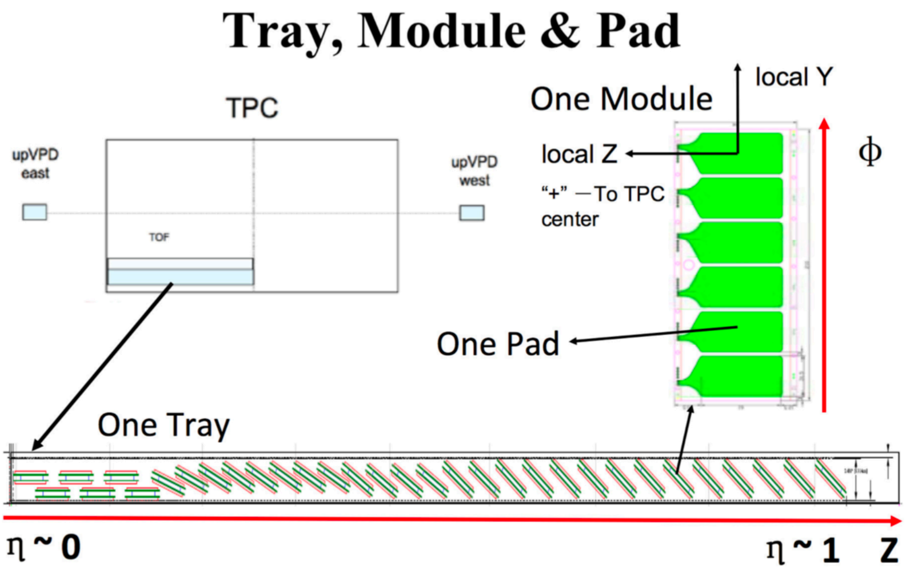

Fig. 2.6: (color online) The details of TOF trays, modules and pads at STAR. The figure is taken from [45].

(MRPC) modules, the side view of one MRPC module is shown in Fig. 2.7. MRPC mainly contains the two electrodes with a voltage of 7kV applied and a stack of resistive glass plates with six uniform gas gaps between them. Then every small gas gap is filled with the high and uniform electric fields and MRPC works in avalanche mode. When the charged particles pass through the module, there will be simultaneous avalanches in the six gas gaps. The corresponding signal is the superposition of all avalanches in these gas gaps. We already know the distance (L) between TOF and collision vertex, thus the speed (β) of the particles and their mass can be calculated:

$$\beta = \frac{v}{c} = \frac{L}{c\Delta t} \tag{2.4}$$

$$m^2 = p^2(\frac{1}{\beta} - 1) \tag{2.5}$$

where $\beta = p/E$ and $E = \sqrt{p^2 + m^2}$, p is the momentum of the particles measured by TPC and Δt is the difference between the start time (measured by TOF) and the stop tome (measured by VPD, which will be discussed later). Fig. 2.8 shows the mass square distribution measured by TOF as a function of rigidity at $\sqrt{s_{\rm NN}}$ = 39 GeV. It's obviously to see that protons, kaons and pions are clearly separated at high momentum region.

2.2.3 Vertex Position Detector (VPD)

The VPD has two identical detector components, which are mounted symmetrically on the east and west sides of STAR center at a distance of 5.7m. Fig. 2.9 shows the the front view of one of the VPD assemblies. Each VPD assembly consists of nineteen detectors, which corresponds to approximately half of the solid angle in a pseudo-rapidity range of $4.24 \leq \eta \leq 5.1$.

VPD can measure the primary vertex position (Z_{vtx}) along the beam pipe and the

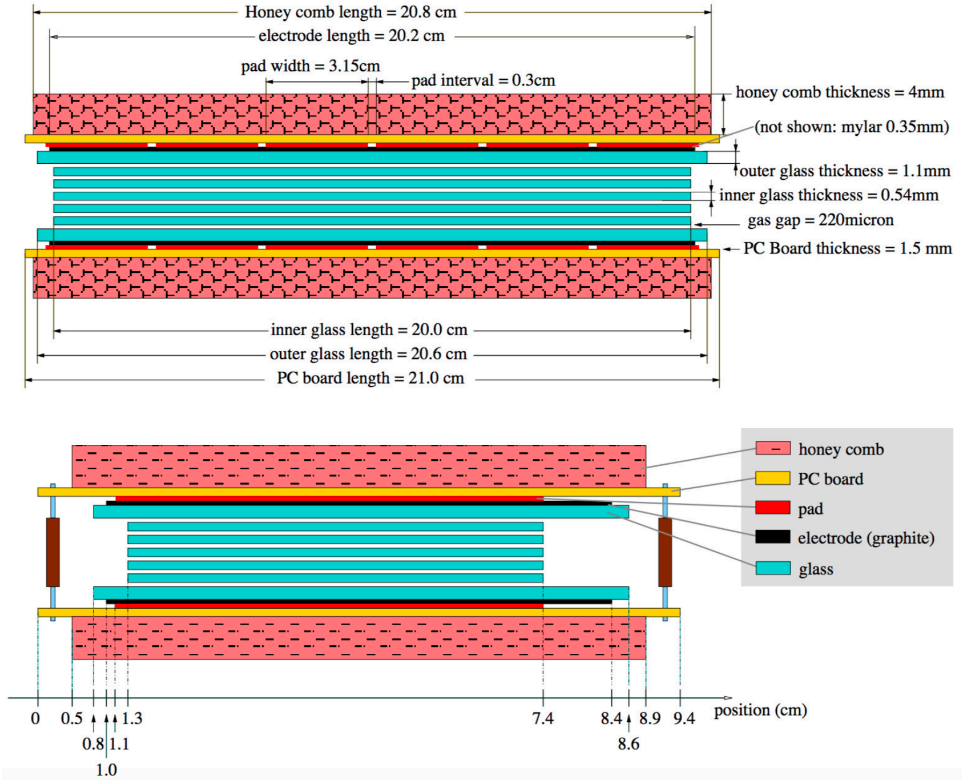

Fig. 2.7: (color online) The two-side view on the Multi-gap Resistive Plate Chamber (MRPC) modules. The figure is taken from [45].

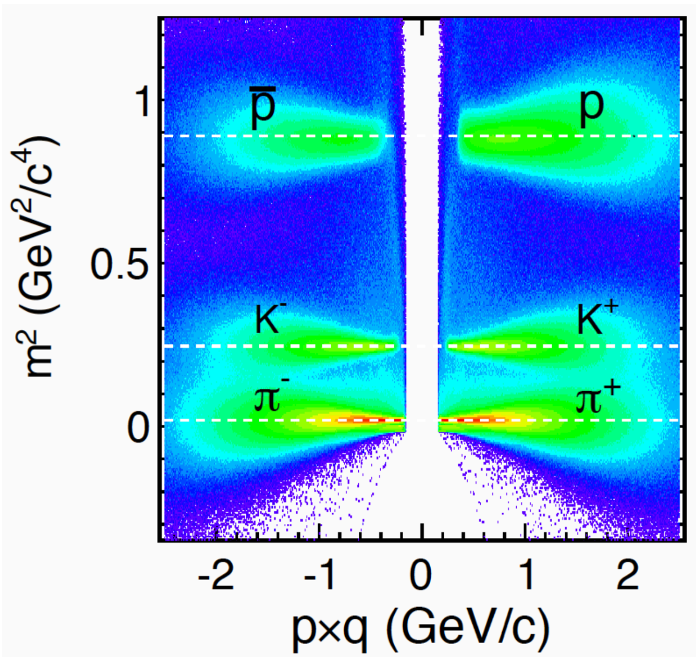

Fig. 2.8: (color online) The mass square distribution as a function of rigidity at $\sqrt{s_{\mathrm{NN}}}$ = 39 GeV.

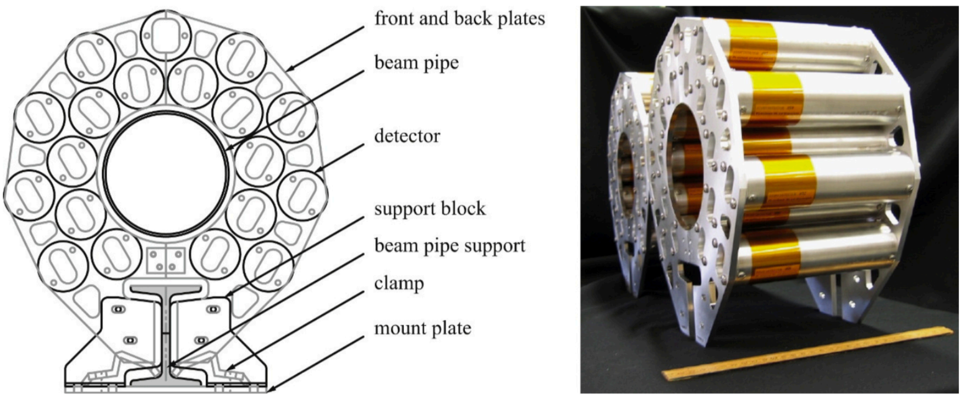

Fig. 2.9: (color online) (left) The schematic front view of a VPD assembly. (right) The photo of the two VPD assemblies. The figure is taken from [41].

start time (T_{start}) for TOF can be obtained by the following two formulas:

$$Z_{vtx} = c(T_{east} - T_{west})/2 \tag{2.6}$$

$$T_{start} = (T_{east} + T_{west})/2 - L/c, \tag{2.7}$$

where T_{east} and T_{west} are the measured times from the east and west VPD assemblies respectively, c is the speed of light and L is the distance between VPD assembly and the center of the STAR.

2.3 The Fixed-Target (FXT) Program at STAR

In this section we will discuss the Fixed-Target (FXT) program at STAR. Just as its name implies, the collision mode of FXT is different from the centroid collision mode. The FXT program will approach higher μ_B range. Its main aim is to search for the evidence of the first entrance into the QGP, and confirm the onsets of de-confinement and the critical point.

On May 20, 2015, STAR performed its first test run for FXT program, and the test run is successful. Fig. 2.10 shows the schematic of the FXT program at STAR. The target is located at the edge of TPC, 211 cm from the center of TPC. And the incident beam is from the right side of the figure (west side of the detector) and hits the target. The target is a 1mm thick gold foil with 1 cm high and 4 cm wide. The mid-rapidity for the FXT program is $|y_{mid}| = 1.52$ at $\sqrt{s_{\mathrm{NN}}} = 4.5$ GeV.

Tab. 2.1 shows the TOF multiplicity cut for FXT program in Au+Au collisions at $\sqrt{s_{\mathrm{NN}}} = 4.5$ GeV. There are six runs available for the analysis, runs from 16140033 to 16140036 have only one trigger and runs 16140037 and 16140038 have both a FXT and a laser trigger. The last column is the number of the vertices within 210 cm $< V_z <$ 212 cm.

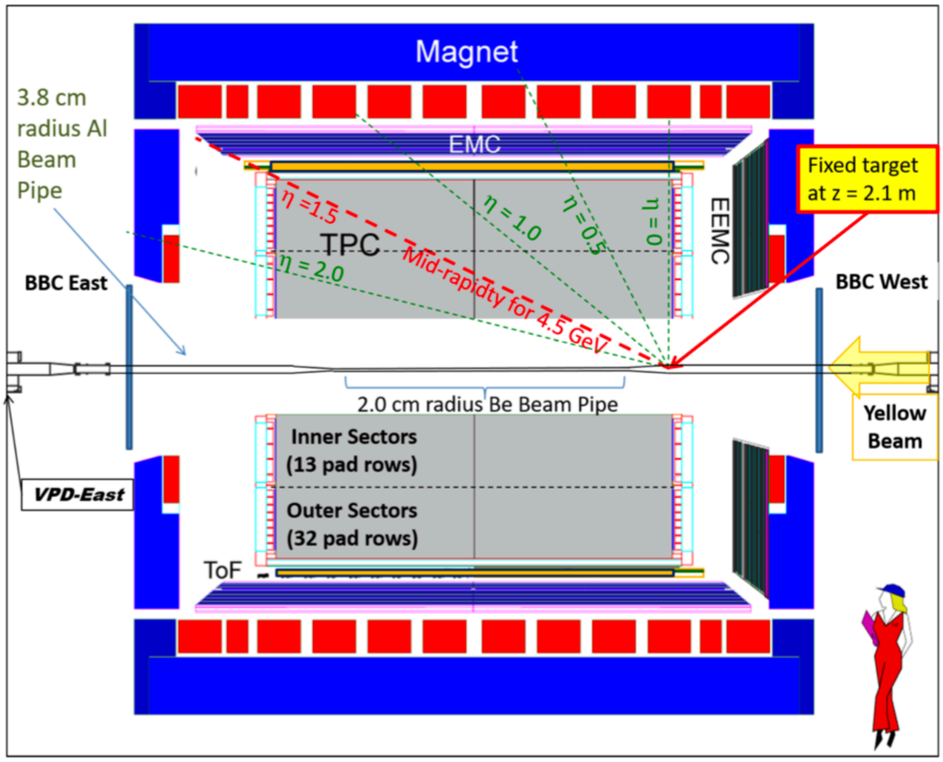

Fig. 2.10: (color online) Schematic of the STAR experiment for the Fixed-Target program. The figure is taken from [46].

Tab. 2.1: TOF multiplicity cut and the total number of triggers for FXT program in Au+Au Collisions

Run #	**# of Bunches**	**TOF multiplicity cut**	**# of Trigger**	**# of Vertices**
16140033	1	130	89294	89240
16140034	1	50	116629	108888
16140035	1	200	4909	4908
16140036	1	130	119238	119201
16140037	6	160	603721*	603658
16140038	6	130	414977	414796
Total			1348768	1340691

Chapter 3

Analysis Details

3.1 Data Sets

The datasets collected with a minimum bias trigger[47] at the STAR experiment in Au+Au collisions are $\sqrt{s_{\mathrm{NN}}}$ = 4.5, 7.7, 11.5, 14.5, 19.6, 27, 39, 54.4, 62.4 and 200 GeV, and in Cu+Cu collisions at $\sqrt{s_{\mathrm{NN}}}$ = 22.4, 62.4 and 200 GeV. The 7.7, 11.5, 39, 62.4 and 200 GeV data were taken in 2010, the 19.6 and 27 GeV data were taken in 2011, the 14.5 GeV data was taken in 2014, the offline 4.5 GeV data was taken in 2015, and the 54.4 GeV data were taken in 2017. The Cu+Cu data at $\sqrt{s_{\mathrm{NN}}}$ = 22.4, 62.4 and 200 GeV were collected in 2005. Minimum bias trigger is used in the data taking, its definition is the coincidence of zero degree calorimeters (ZDC), VPD and beam-beam counters (BBC). The details of these datasets are shown in the Tab. 3.1.

Tab. 3.1: Data sets in Au+Au collisions at $\sqrt{s_{\mathrm{NN}}}$ = 7.7−200 GeV, in FXT collisions at $\sqrt{s_{\mathrm{NN}}}$ = 4.5 GeV and in Cu+Cu collisions at $\sqrt{s_{\mathrm{NN}}}$ = 22.4, 62.4 and 200 GeV .

	$\sqrt{s_{\mathrm{NN}}}$ (GeV)	Trigger Setup name	Year	Production Tag	TriggerID
Au+Au	**7.7**	AuAu7_Production	2010	P10ih	290001 290004
	11.5	AuAu11_Production			310004 310014
	14.5	production_15GeV_2014	2014	P14ii	440015 440016
	19.6	AuAu19_Production	2011	P11id	340001 340011 340021
	27	AuAu27_Production_2011			360001
	39	AuAu39_Production	2010	P10ik	280001
	54.4	AuAu54_Production_2017	2017	P17ii	580001 580011 580021
	62.4	AuAu62_Production	2010	P10ik	270001 27001 270021
	200	AuAu200_Production			260001 260011 260021 260031
Au+Au FXT	**4.5**	fixedTarget2015	2015	P16ia	1
Cu+Cu	**22.4**	Cu22ProductionMinBias	2005	P17ii	86011
	62.4	Cu62productionMinBias	2005	P17ii	76002 76007 76011
	200	CuProductionMinBias	2005	P17ii	66007

Tab. 3.1 shows the details of data sets in Au+Au collisions at $\sqrt{s_{\mathrm{NN}}}$ = 7.7−200 GeV, in FXT collisions at $\sqrt{s_{\mathrm{NN}}}$ = 4.5 GeV and in Cu+Cu collisions at $\sqrt{s_{\mathrm{NN}}}$ = 22.4, 62.4 and 200 GeV .

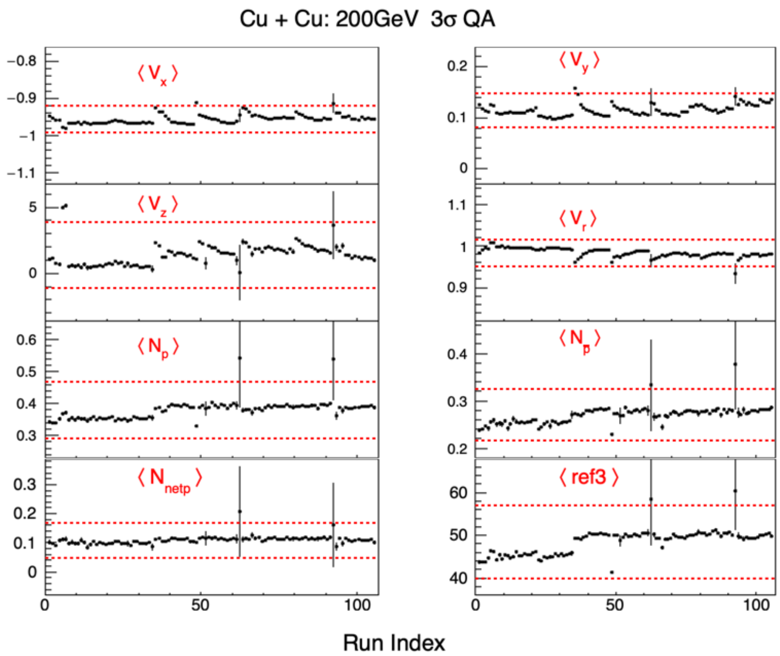

Fig. 3.1: (color online) Run by run QA in Cu+Cu collisions at $\sqrt{s_{\mathrm{NN}}}$ = 200 GeV.

3.1.1 Run by Run QA

We applied some Quality Assurance (QA) studies on the datasets to remove events with the bad runs. Fig. 3.1 shows the averaged vertex position, number of proton, anti-proton and net-proton as a function of run index in Cu+Cu collisions at $\sqrt{s_{\mathrm{NN}}}$ = 200 GeV. We take out the runs that are out of 3σ, which are shown as red lines.

Bad run lists for BES-I energies: `https://www.star.bnl.gov/protected/bulkcorr/luoxf/PaperProposal2018/QA/BadRunList_3sig.txt`

3.1.2 Signed DCA_{xy} Cuts

According to the unfolding study for most central collisions at $\sqrt{s_{\mathrm{NN}}}$ = 7.7 GeV, predicted two-component structure[48] is likely there. Fig. 3.2 shows the net-proton distributions for most central collisions without CBWC with unfolding method at $\sqrt{s_{\mathrm{NN}}}$ = 7.7 GeV.

In order to investigate the origin of the second component at smaller part of the net-proton distribution, we have checked the run log(Fig. 3.3) and plotted events having the number of protons less than 10 at most central (0-5%) collisions as a function of run index, which is shown in Fig. 3.4. It is found that those events with extremely small number of protons are mainly coming from specific run durations. Within runs #11125089 − #11126067, we picked up 15 events having protons less than 10, and plotted various track-wise quantities for each event, see here. It was found in those strange events, DCA distribution looks strange, which has mean value about 1.0. Since in higher-moment analysis DCA cut < 1.0 cm is applied, number of protons become extremely small for those events. In addition, the strange DCA distribution is found to be caused by the shift of signed DCA$_{xy}$ distribution (normally around zero), which is shown in Fig. 3.7.

$\langle \mathrm{DCA}_{xy} \rangle$ as a function of event ID for each run has been checked at $\sqrt{s_{\mathrm{NN}}}$ = 7.7 GeV for most central $(0-5\%)$ centrality, which is summarized here. The left panel of Fig. 3.6 is an example of $\langle \mathrm{DCA}_{xy} \rangle$ distributions for strange events. It is found that $\langle \mathrm{DCA}_{xy} \rangle$ show

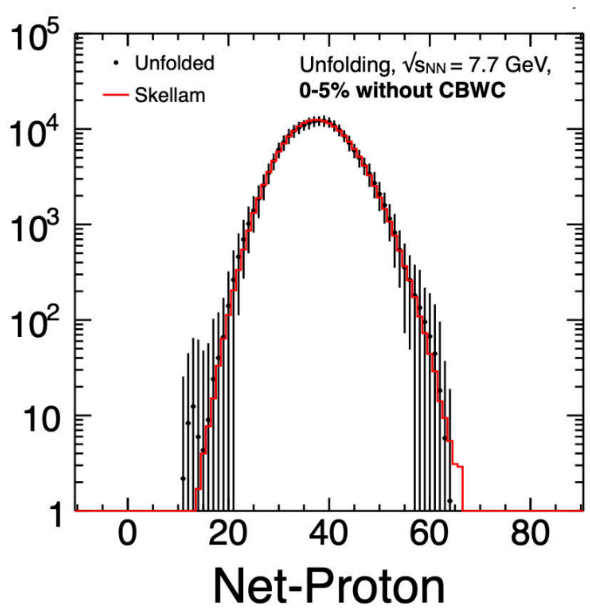

Fig. 3.2: (color online) The net-proton distributions for most central collisions without CBWC with unfolding method at $\sqrt{s_{\mathrm{NN}}}$ = 7.7 GeV.

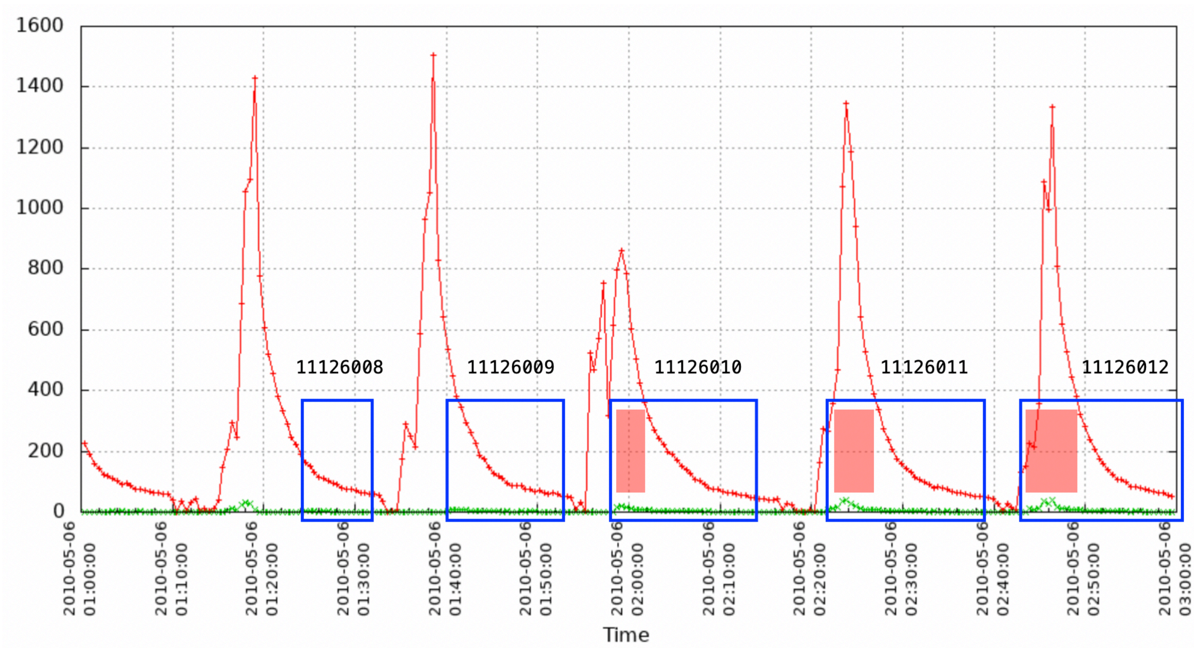

Fig. 3.3: (color online) Run log

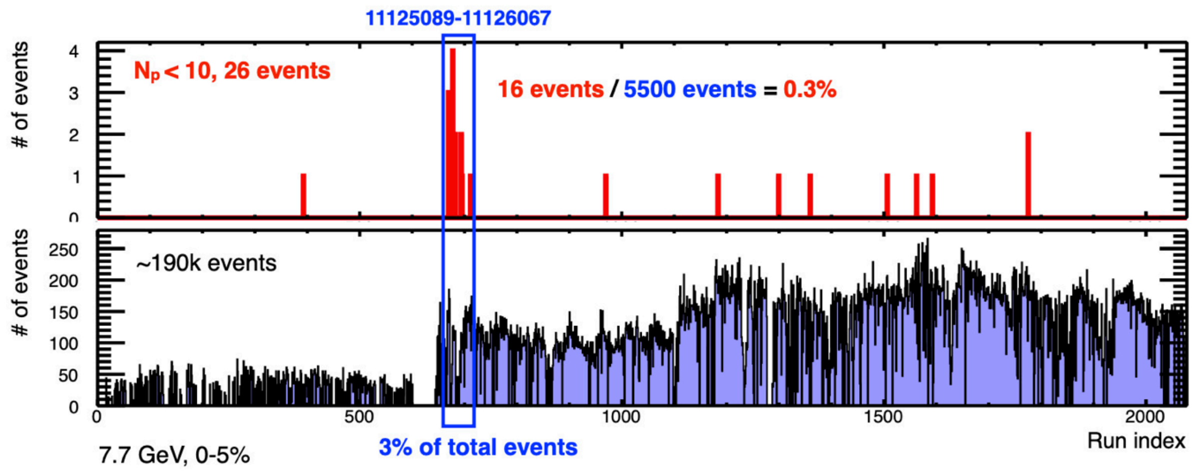

Fig. 3.4: (color online) The number of events with the number of protons less than 10 at most central (0-5%) collisions is plotted as a function of run index.

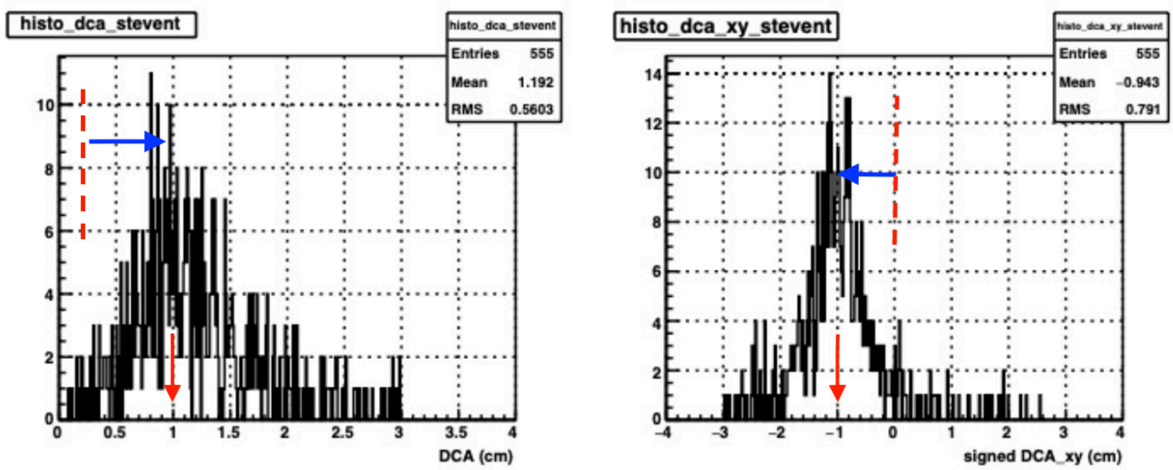

Fig. 3.5: (color online) (left) The DCA distributions with strange events per event at most central $(0-5\%)$ collisions at $\sqrt{s_{\mathrm{NN}}}$ = 7.7 GeV, which has mean value about 1.0. (right) The strange $\langle \mathrm{DCA}_{xy} \rangle$ distributions per event at most central $(0-5\%)$ at $\sqrt{s_{\mathrm{NN}}}$ = 7.7 GeV. The strange DCA distribution is found to be caused by the shift of signed DCA_{xy} distribution (normally around zero).

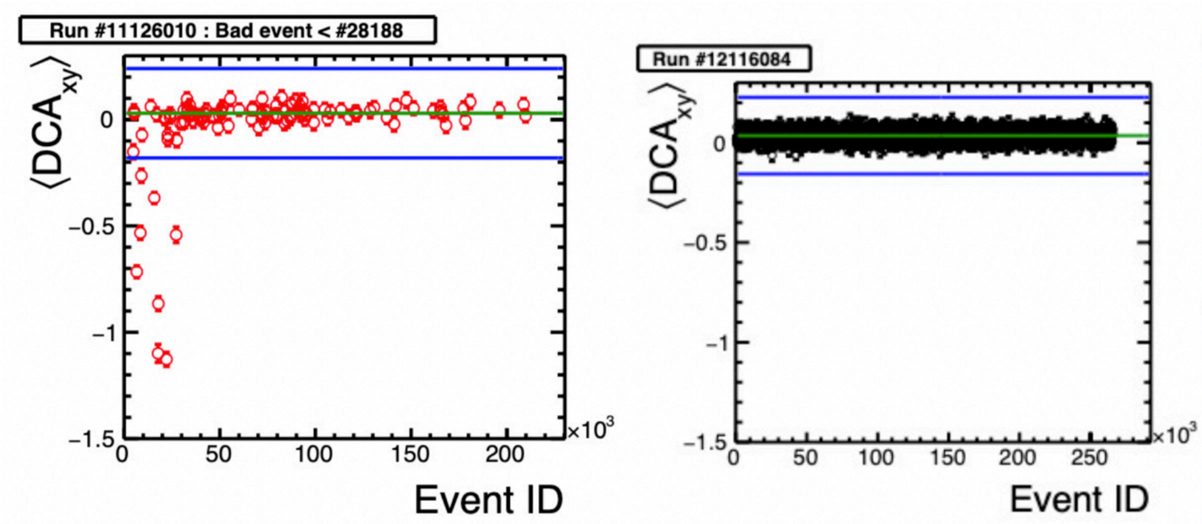

Fig. 3.6: (color online) (left) $\langle \mathrm{DCA}_{xy} \rangle$ vs event ID distributions for strange events, $\langle \mathrm{DCA}_{xy} \rangle$ shows negative values at the beginning of those runs. (right) The $\langle \mathrm{DCA}_{xy} \rangle$ distributions for normal runs (shown in black), where all events show $\langle \mathrm{DCA}_{xy} \rangle \sim 0$.

negative values at the beginning of those runs. Green and blue solid lines are mean and $+/-7\sigma$ determined for whole data sets (note that in some other energies mean and sigma are determined for each run, since those are unstable). The last event ID which deviates from mean $+/-7\sigma$, plus 20k (for safety) is defined as a "event boundary". For 7.7 GeV, all events before the event boundary are removed from the cumulant calculations. You can find the specific event boundary in the Tab. B.1 at $\sqrt{s_{\mathrm{NN}}} = 7.7$ GeV. The first column is the (bad) run number, and the second column shows the event ID, we need to remove all events before that event ID. The right panel of Fig. 3.6 is the $\langle \mathrm{DCA}_{xy} \rangle$ distributions for normal runs (shown in black), where all events show $\langle \mathrm{DCA}_{xy} \rangle \sim 0$.

Fig. 3.7 shows the averaged DCA_{XY} distributions with spoiled and good events at $\sqrt{s_{\mathrm{NN}}} = 7.7$ GeV. Fig. 3.8 and Fig. 3.9 show the correlation between the number of proton and averaged DCA_{XY} with total, good and removed events for most central collisions at $\sqrt{s_{\mathrm{NN}}} = 7.7$ GeV and 62.4 GeV. The same checks have also been done at $\sqrt{s_{\mathrm{NN}}} = 11.5$, 14.5, 19.6, 27, 54.4 and 62.4 GeV, please find the details here. You can find the eventId cut in the Tab. B.2 at $\sqrt{s_{\mathrm{NN}}} = 11.5$, 14.5, 19.6, 27, 39 and 62.4 GeV.

3.1.3 Event Selection

There are some pile up events where TPC tracks do not match the TOF (If (nFitPts > 10 && Tofmatchflag > 0 && $|\eta| < 0.5$) nTofMatch++;), and other pile up events where TPC tracks match the TOF but the velocity (β) is not calculated correctly (If (nFitPts > 10 && $\beta > 0.1$ && $|\eta| < 1$) Beta_eta1++;).

Then we can get the correlation between the number of primary TPC tracks matched to TOF and number of primary TPC tracks with $\eta < 1$ (TPC Refmult), which is shown in the left Fig. 3.10. And the correlation between the number of primary TPC tracks with wrong β and TPC Refmult is shown in the right Fig. 3.10. Events below the red lines are need to be rejected. The additional two cuts should be placed in the analysis.
if (nTofmatch ≤ 1 || nTofmatch $< 0.5\times$(Refmult$-$20)) continue;
if (Beta_eta1 ≤ 0 || Beta_eta1 $< 26\times$(Refmult$-$20)/33.)) continue;

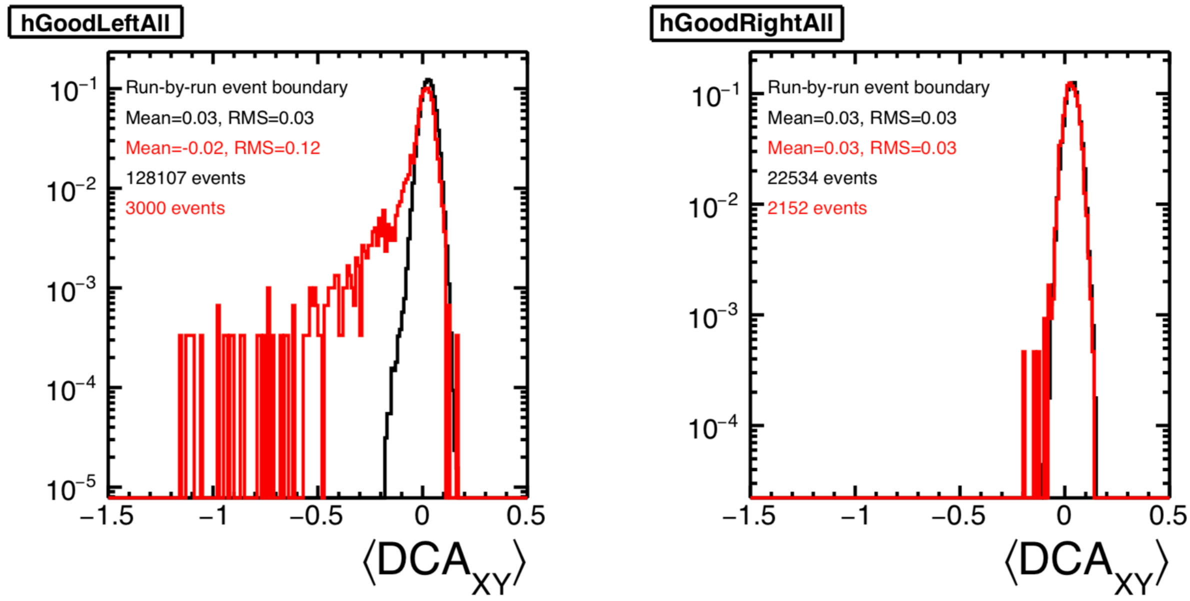

Fig. 3.7: (color online) (left) The $\langle \mathrm{DCA}_{xy} \rangle$ distributions with boundary offset for 50k with strange events for most central $(0-5\%)$ collisions at $\sqrt{s_{\mathrm{NN}}}\ = 7.7$ GeV. (right) The strange $\langle \mathrm{DCA}_{xy} \rangle$ distributions for most central ($0-5\%$) at $\sqrt{s_{\mathrm{NN}}}\ = 7.7$ GeV.

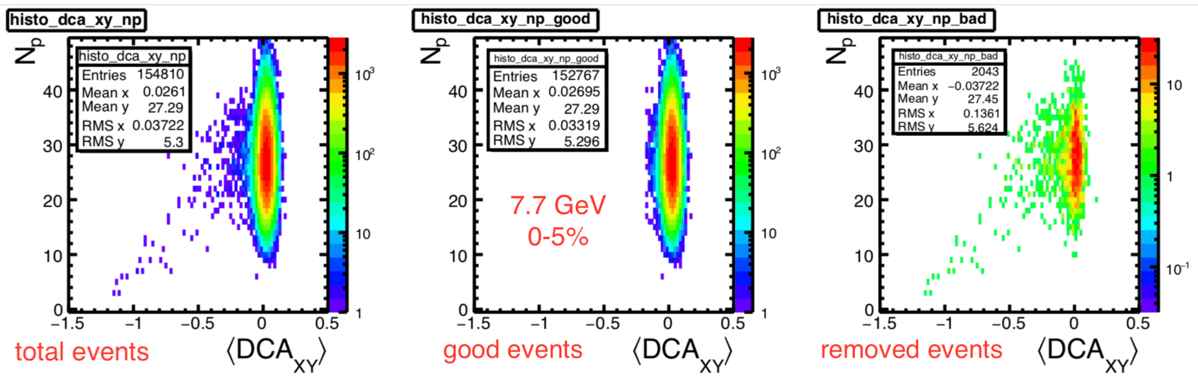

Fig. 3.8: (color online) The correlation between the number of proton and averaged DCA_{XY} with total (left panel), good (right panel) and removed (right panel) events for most central collisions at $\sqrt{s_{\mathrm{NN}}}\ = 7.7$ GeV

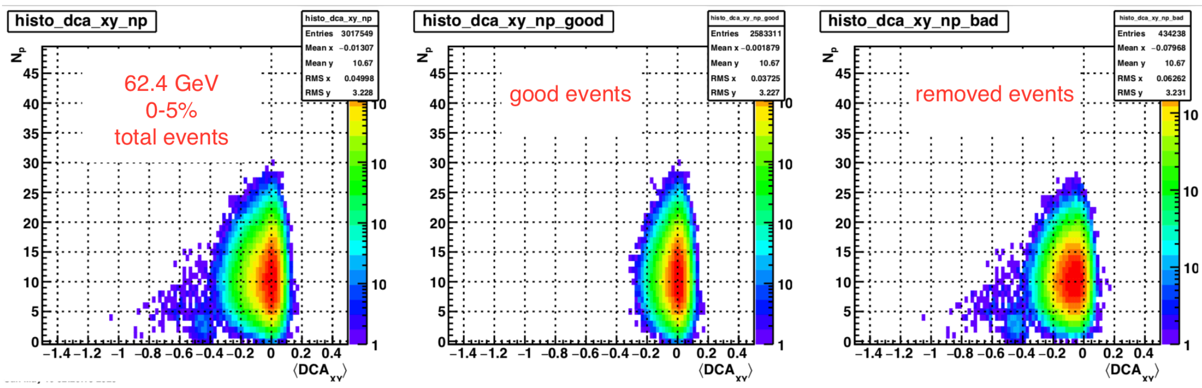

Fig. 3.9: The correlation between the number of proton and averaged DCA_{XY} with total (left panel), good (right panel) and removed (right panel) events for most central collisions at $\sqrt{s_{\mathrm{NN}}}\ = 62.4$ GeV.

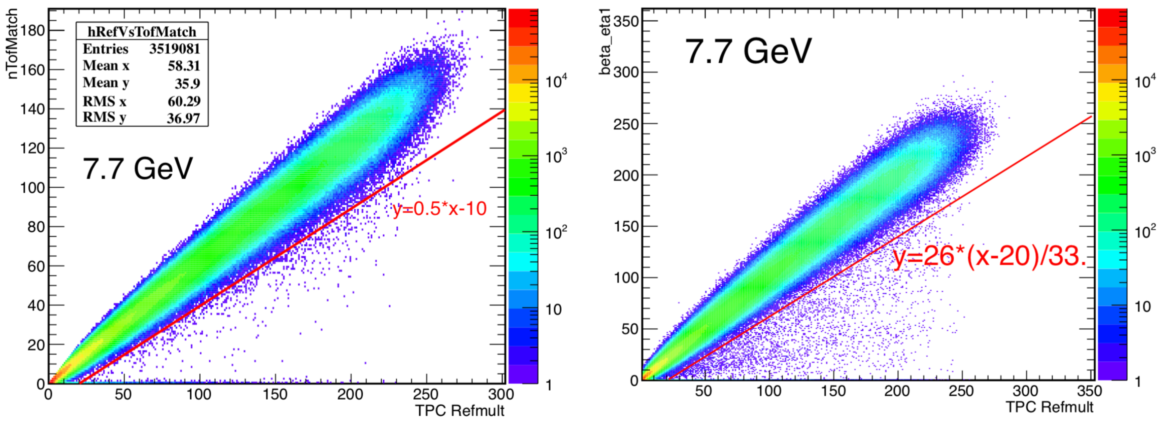

Fig. 3.10: (color online) (left) Correlation between number of tofmatched tracks and number of primary tracks in Au+Au collisions at $\sqrt{s_{\mathrm{NN}}}$ = 7.7 GeV. (right) Correlation between number of tracks with $\beta > 0.1$ and number of primary tracks in Au+Au collisions at $\sqrt{s_{\mathrm{NN}}}$ = 7.7 GeV.

You can find the rejected events for all the BES-I energies in the Tab. B.3, which shows the additional two cuts used in the analysis in Au+Au collisions at $\sqrt{s_{\mathrm{NN}}}$ = 7.7, 11.5, 14.5, 19.6, 27, 39, 54.4, 62.4 and 200 GeV.

Tab. 3.2: Event Selection in Au+Au collisions at $\sqrt{s_{\mathrm{NN}}}$ = 7.7–200 GeV, in FXT collisions at $\sqrt{s_{\mathrm{NN}}}$ = 4.5 GeV and in Cu+Cu collisions at $\sqrt{s_{\mathrm{NN}}}$ = 22.4, 62.4 and 200 GeV .

<table>
<tr><th></th><th>$\sqrt{s_{\mathrm{NN}}}$ (GeV)</th><th>V_z(cm)</th><th>V_r(cm)</th><th>$|VpdV_z - V_z|$ (cm)</th><th># of events (million)</th></tr>
<tr><td rowspan="9">Au+Au</td><td>7.7</td><td>$|V_z| < 40$</td><td rowspan="2">< 2</td><td rowspan="5">nan</td><td>3</td></tr>
<tr><td>11.5</td><td rowspan="8">$|V_z| < 30$</td><td>6.6</td></tr>
<tr><td>14.5</td><td>< 1</td><td>20</td></tr>
<tr><td>19.6</td><td rowspan="6">< 2</td><td>15</td></tr>
<tr><td>27</td><td>30</td></tr>
<tr><td>39</td><td rowspan="4">< 3</td><td>86</td></tr>
<tr><td>54.4</td><td>470</td></tr>
<tr><td>62.4</td><td>47</td></tr>
<tr><td>200</td><td>238</td></tr>
<tr><td>Au+Au FXT</td><td>4.5</td><td>$210 < V_z < 212$</td><td>nan</td><td>nan</td><td>1.355</td></tr>
<tr><td rowspan="3">Cu+Cu</td><td>22.4</td><td rowspan="3">$|V_z| < 30$</td><td rowspan="3">< 2</td><td rowspan="3">nan</td><td>0.64</td></tr>
<tr><td>62.4</td><td>1.46</td></tr>
<tr><td>200</td><td>5.377</td></tr>
</table>

Tab. 3.2 shows the details of the event cuts and statistics after event selection in Au+Au collisions at $\sqrt{s_{\mathrm{NN}}}$ = 7.7–200 GeV, in FXT collisions at $\sqrt{s_{\mathrm{NN}}}$ = 4.5 GeV and in Cu+Cu collisions at $\sqrt{s_{\mathrm{NN}}}$ = 22.4, 62.4 and 200 GeV . It's well known that the radius of the beam pipe is 3.95 cm, the proton sample contains background knocked out from the beam pipe and detector material by interactions of produced hadrons in these material[49, 50].

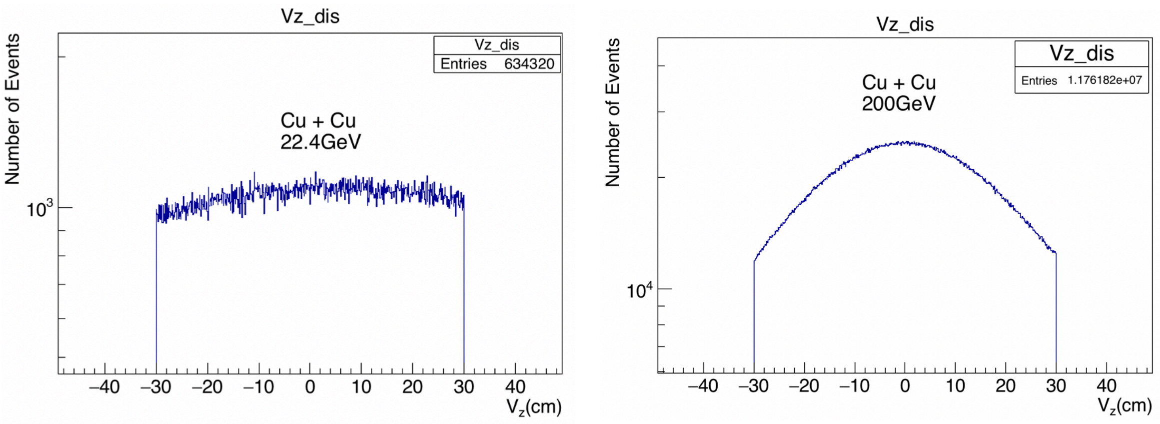

Fig. 3.11: (color online) V_z distribution after event cuts in Cu+Cu collisions at $\sqrt{s_{\rm NN}} = 22.4$ (left) and 200 GeV(right).

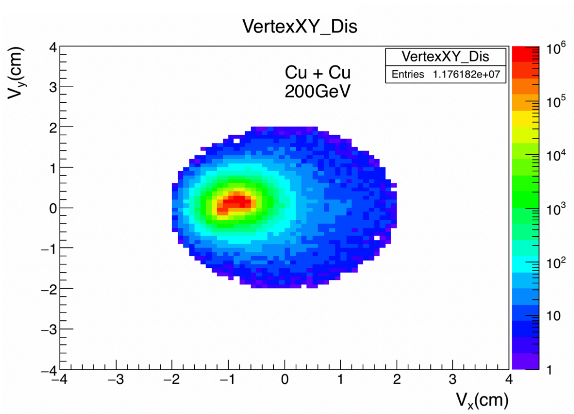

Fig. 3.12: (color online) V_y vs V_x distribution after event cuts in Cu+Cu collisions at $\sqrt{s_{\rm NN}} = 200$ GeV.

In order to reject these background, the event vertex radius ($V_r = \sqrt{V_x^2 + V_y^2}$) is required to be within 2 cm of the center of STAR[47]. At $\sqrt{s_{\mathrm{NN}}}$ = 14.5 GeV, the mean vertex position for all events is centered at (0, -0.89) cm in the $x-y$ plane, $v_r < 1$ cm from the center is applied[51]. In order to achieve uniform detector performance and sufficient statistical of the measured observables, V_z within 30 cm are applied except for the 7.7 GeV ($V_z \leq 40$ cm) to select the minimum bias trigger events. However, for FXT program, the z-vertex cut should be 210 cm $< V_z <$ 212 cm due to the target is located at at the edge of TPC, 211 cm from the center of TPC. The difference between vertex along the beam direction measured by TPC and VPD are less than 3 cm to eliminate pile up events for energies greater than 39 GeV.

Fig. 3.11 shows the distributions of the reconstructed primary vertex along the beam direction after event selection in Cu+Cu collisions at $\sqrt{s_{\mathrm{NN}}}$ = 22.4 and 200 GeV. The V_z distribution at low energy is more wider, flatter than its distribution at high energy, this is mainly because that the beam is harder to focus at lower energy. Fig. 3.12 shows the V_y vs V_x distribution after event selection in Cu+Cu collisions at $\sqrt{s_{\mathrm{NN}}}$ = 200 GeV. $V_r(\sqrt{V_x^2 + V_y^2}) < 2$ cm is applied.

3.1.4 Track Quality Cuts

Tab. 3.3: Track quality cuts, kinematic and PID cuts in Au+Au collisions at $\sqrt{s_{\mathrm{NN}}}$ = 7.7−200 GeV, in FXT collisions at $\sqrt{s_{\mathrm{NN}}}$ = 4.5 GeV and in Cu+Cu collisions at $\sqrt{s_{\mathrm{NN}}}$ = 22.4, 62.4 and 200 GeV .

$\sqrt{s_{\mathrm{NN}}}\,(GeV)$	Track Quality Cuts	Kinematic Cuts			PID Cuts	
Au+Au 7.7−200	d_{ca} < 1 cm nFitPts > 20 nhitdEdx > 5 ratio > 0.52	|y| < 0.5	$0.4 < p_{\mathrm{T}} < 0.8\,(\mathrm{GeV}/c)$	p < 1(GeV/c)	**TPC**	$\|n\sigma_p\| < 2$
			$0.8 < p_{\mathrm{T}} < 2.0\,(\mathrm{GeV}/c)$	p < 3(GeV/c)	**TPC+TOF**	$\|n\sigma_p\| < 2$ $0.6 < m^2 < 1.2(\mathrm{GeV}^2/c^2)$
Au+Au FXT: 4.5	d_{ca} < 1 cm nFitPts > 20 nhitdEdx > 5 ratio > 0.52	-2 < y < 0	$0.4 < p_{\mathrm{T}} < 0.8\,(\mathrm{GeV}/c)$	p < 1(GeV/c)	**TPC**	$\|n\sigma_p\| < 2$
			$0.8 < p_{\mathrm{T}} < 2.0\,(\mathrm{GeV}/c)$	p < 3(GeV/c)	**TPC+TOF**	$\|n\sigma_p\| < 2$ $0.6 < m^2 < 1.2(\mathrm{GeV}^2/c^2)$
Cu+Cu 22.4, 62.4 and 200	d_{ca} < 1 cm nFitPts > 20 nhitdEdx > 5 ratio > 0.52	|y| < 0.5	$0.4 < p_{\mathrm{T}} < 0.8\,(\mathrm{GeV}/c)$		**TPC**	$\|n\sigma_p\| < 2$

Tab. 3.3 shows the track quality, kinematic and PID cuts in Au+Au collisions at $\sqrt{s_{\mathrm{NN}}}$ = 7.7−200 GeV, in FXT collisions at $\sqrt{s_{\mathrm{NN}}}$ = 4.5 GeV and in Cu+Cu collisions at $\sqrt{s_{\mathrm{NN}}}$ = 22.4, 62.4 and 200 GeV . The distance of closet approach (d_{ca}) to the reconstructed primary tracks is required to be less than 1 cm to eliminate the effects of secondary charged particles. The number of the points hit in the TPC used for track fitting should be at least 20. The number of hit points for calculating the dE/dx is not less than 5. To avoid the track splitting, the ratio of the number of points used in the track fitting to the number of possible hits greater than 0.52 is required.

3.2 Particle Indentification

The two main detectors at STAR [36] are TPC (Time Projection Chamber) [37] and TOF (Time Of Flight) [38], which can provide excellent particle identification and identify charged particles within mid-rapidity window ($|y| < 0.5$).

3.2.1 For Au+Au Collisions

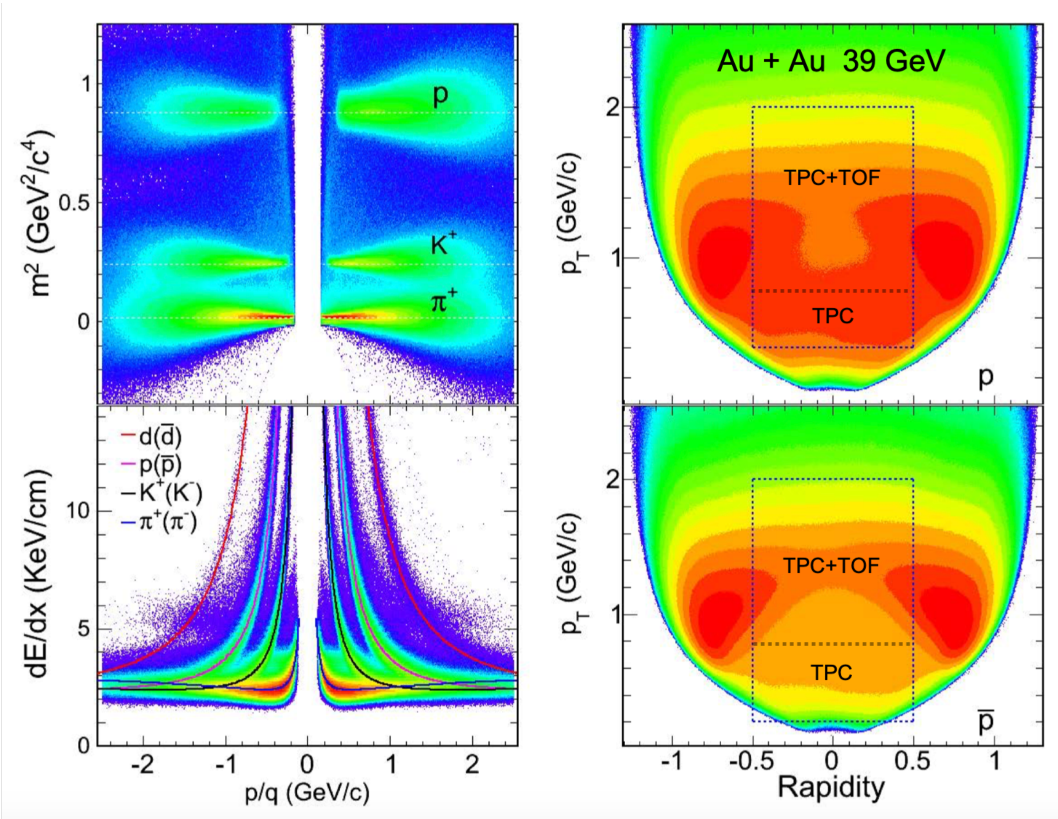

Fig. 3.13: (color online) (left bottom) The ionization energy loss (dE/dx) distributions in Au+Au collisions at $\sqrt{s_{\mathrm{NN}}}$ = 39 GeV, the solid lines in the figure are expectation line from bichsel formula. (Left top) The mass square distributions in Au+Au collisions at $\sqrt{s_{\mathrm{NN}}}$ = 39 GeV. (right) The phase acceptance of (anti−) proton for Au+Au collisions at $\sqrt{s_{\mathrm{NN}}}$ = 39 GeV.

The top left panel of Fig. 3.13 shows the ionization energy loss ($d\mathrm{E}/dx$) distributions measured by STAR TPC in Au+Au collisions at $\sqrt{s_{\mathrm{NN}}}$ = 39 GeV. It was found that at higher p_{T} range, protons and kaons can not be identified clearly because of merged bands. The left upper panel of Fig. 3.13 shows the mass square distributions measured by STAR TOF in Au+Au collisions at $\sqrt{s_{\mathrm{NN}}}$ = 39 GeV. We can use mass square cut to select protons and kaons within high momentum range. So, In order to maximize the purity and efficiency of charged particles, we split the momentum into two intervals: the lower p_{T} range ($0.4 < p_{\mathrm{T}} < 0.8\,(\mathrm{GeV}/c)$) with TPC, and the higher p_{T} range ($0.8 < p_{\mathrm{T}} < 2.0\,(\mathrm{GeV}/c)$) with both TPC and TOF. The right panel of Fig. 3.13 shows the phase acceptance of (anti−)proton. The (anti−)proton included in the blue box are used for the moment analysis. The particles included in the red line without (anti-)proton are used to determine the centrality to avoid the effect of auto-correlation. After particle identification, we can get the purity of the proton and anti-proton.

3.2.2 For Fixed-Target Collisions

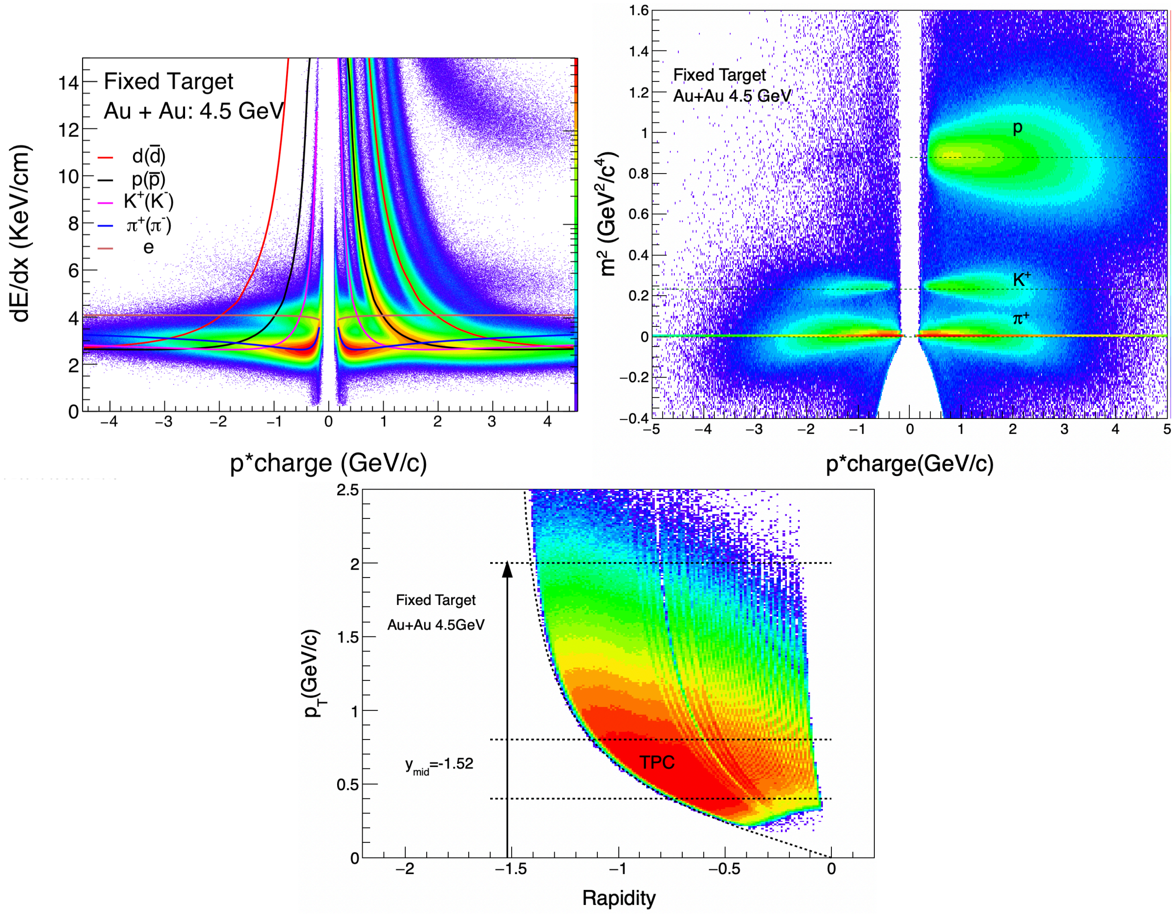

Fig. 3.14: (color online) (left top) The ionization energy loss (dE/dx) distribution. (right top) The mass square distribution.(bottom) The phase acceptance of proton for Au+Au FXT collisions at $\sqrt{s_{\rm NN}}$ = 4.5 GeV.

Fig. 3.14 shows the particle identification for Au+Au FXT collisions at $\sqrt{s_{\rm NN}}$ = 4.5 GeV. The left top panel shows the ionization energy loss (dE/dx) distribution for Au+Au FXT collisions at $\sqrt{s_{\rm NN}}$ = 4.5 GeV, which are measured by STAR TPC. The right top panel shows the mass square distribution for Au+Au FXT collisions at $\sqrt{s_{\rm NN}}$ = 4.5 GeV. The bottom panel shows the proton acceptance.

3.2.3 For Cu+Cu collisions

Fig. 3.15 shows the particle identification for Cu+Cu collisions at $\sqrt{s_{\rm NN}}$ = 22.4 GeV.

3.3 Centrality Determination

In heavy ion collisions, centrality determination is very important. A participant is defined that a nucleon participanted in at least one collision. We usually use the N_{part} and

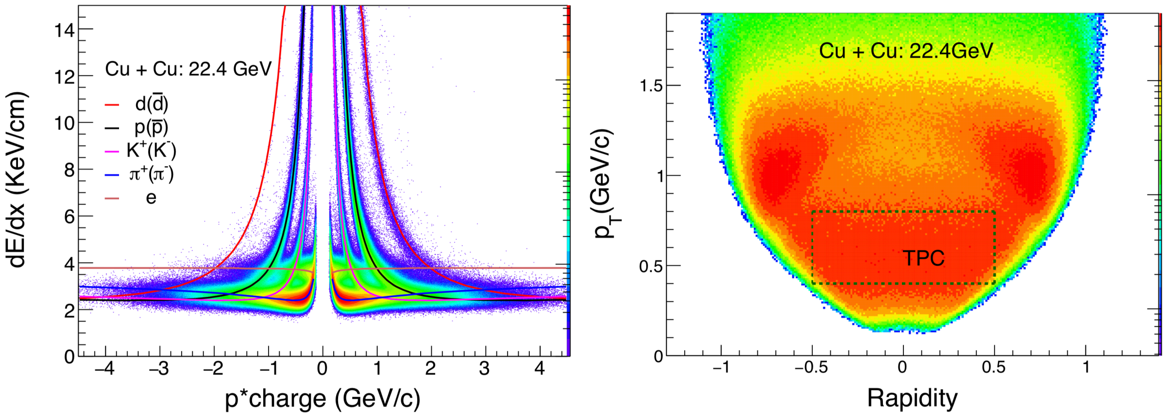

Fig. 3.15: (color online) (left) The ionization energy loss (dE/dx) distributions. (right) The phase acceptance of (anti−)proton for Cu+Cu collisions at $\sqrt{s_{\rm NN}}$ = 22.4 GeV.

N_{coll} to describe the centrality of nucleus+nucleus collisions, where N_{part} is the number of participants and N_{coll} is the number of binary nucleon-nucleon collisions . The impact parameter b is another parameter to describe the centrality and can be calculated in the Glauber model [52, 53].

$$\frac{dN_{ch}}{d\eta} = n_{pp}[xN_{coll} + (1-x)\frac{N_{part}}{2}], \tag{3.1}$$

which are expressed in reference [50, 54], where n_{pp} is the measured multiplicity in pp collisions per unit of pesudo-rapidity, x is the fraction of n_{pp}. N_{part} and N_{coll} can not be directly measured in the heavy ion collision experiment,

$$\frac{dN_{ch}}{d\eta} \propto (N_{part} \longleftrightarrow N_{coll}) \propto b \longrightarrow \textbf{Centrality} \tag{3.2}$$

The number of charged particles created in the collision, which is the experimental observable, is used as an indicator to determine the centrality. Fig. 3.16 is the cartoon of charged particles N_{ch} with Glauber quantities (b and $\langle N_{part}\rangle$) and centrality determination.

Tab. 3.4: Centrality determination in Au+Au collisions at $\sqrt{s_{\rm NN}}$ = 7.7−200 GeV, in FXT collisions at $\sqrt{s_{\rm NN}}$ = 4.5 GeV and in Cu+Cu collisions at $\sqrt{s_{\rm NN}}$ = 22.4, 62.4 and 200 GeV .

$\sqrt{s_{\rm NN}}$ (GeV)	**Track Quality Cuts**	**Kinematic Cuts**	**PID Cuts**
Au+Au 7.7−200	d_{ca} <3 cm nFitPts>10	$\|\eta\| < 1$	$n\sigma_p < -3$ $m^2 < 0.4$
Au+Au FXT: 4.5	d_{ca} <3 cm nFitPts>10	$\|\eta\| < 1$	$n\sigma_p < -3$
Cu+Cu 22.4, 62.4 and 200	d_{ca} <3 cm nFitPts>10	$\|\eta\| < 1$	$n\sigma_p < -3$

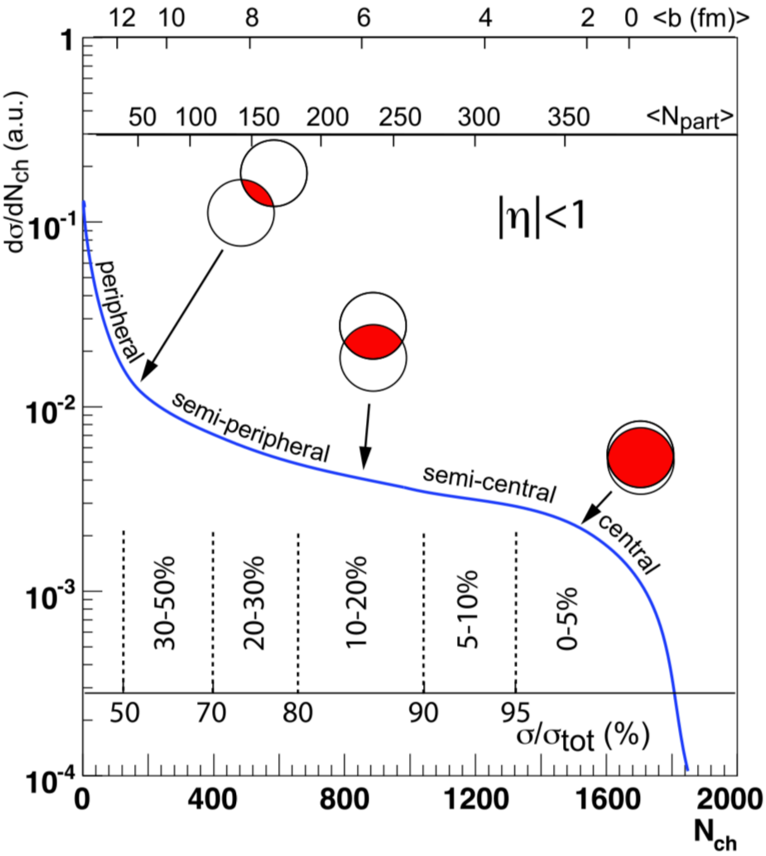

Fig. 3.16: (color online) The cartoon of charged particles N_{ch} with Glauber quantities (b and $\langle N_{part} \rangle$). The figure is taken from [52].

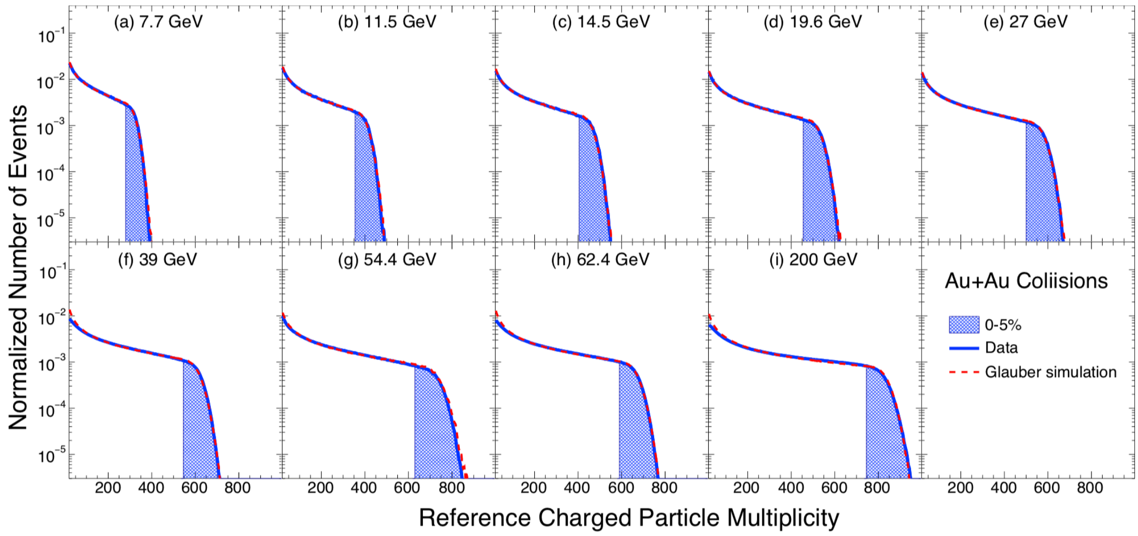

Fig. 3.17: (color online) Normalized reference charged particle multiplicity (N_{ch}) distributions using only kaons and pions in $|\eta| < 1.0$ in Au+Au collisions at $\sqrt{s_{\mathrm{NN}}} = 7.7$, 11.5, 14.5, 19.6, 27, 39, 54.4, 62.4 and 200 GeV.

3.3.1 For Au+Au Collisions

Fig. 3.17 shows the normalized reference charged particle multiplicity (N_{ch}) distributions using only kaons and pions in $|\eta| < 1.0$ in Au+Au collisions at $\sqrt{s_{\mathrm{NN}}} = 7.7$, 11.5, 14.5, 19.6, 27, 39, 54.4, 62.4 and 200 GeV. The red lines are from Glauber simulation. Tab. 3.5 shows the $\langle N_{part}\rangle$ and N_{ch} for Au+Au collisions at $\sqrt{s_{\mathrm{NN}}} = 7.7$, 11.5, 14.5, 19.6, 27, 39, 54.4, 62.4 and 200 GeV.

3.3.2 For Fixed-Target Collisions

Fig. 3.18 shows the normalized reference charged particle multiplicity (N_{ch}) distributions using only kaons and pions in $|\eta| < 1.0$ in FXT collisions at $\sqrt{s_{\mathrm{NN}}} = 4.5$GeV. The red lines are from Glauber simulation. In order to remove the pile-up events, the upper limit on the reference multiplicity for an event in the most centrality bin was set to be 150. Tab. 3.6 shows the $\langle N_{part}\rangle$ and N_{ch} for FXT collisions at $\sqrt{s_{\mathrm{NN}}} = 4.5$ GeV.

3.3.3 For Cu+Cu Collisions

Fig. 3.19 shows the normalized reference charged particle multiplicity (N_{ch}) distributions using only kaons and pions in $|\eta| < 1.0$ in Cu+Cu collisions at $\sqrt{s_{\mathrm{NN}}} = 22.4$, 62.4 and 200 GeVThe red lines are from Glauber simulation. Tab. 3.7 shows the $\langle N_{part}\rangle$ and N_{ch} for Cu+Cu collisions at $\sqrt{s_{\mathrm{NN}}} = 22.4$, 62.4 and 200 GeV.

3.4 Net-Proton Multiplicity Distributions

3.4.1 For Au+Au Collisions

Fig. 3.20 shows event-by-event net-proton multiplicity distributions for Au+Au collisions at $\sqrt{s_{\mathrm{NN}}} = 7.7$, 11.5, 14.5, 19.6, 27, 39, 54.4, 62.4 and 200 GeV for three centralities (0-5%, 30-40% and 70-80%) at mid-rapidity. The error bars are statistical errors. The

Tab. 3.5: $\langle N_{part} \rangle$ and N_{ch} for Au+Au collisions at $\sqrt{s_{\mathrm{NN}}}$ = 7.7, 11.5, 14.5, 19.6, 27, 39, 54.4, 62.4 and 200 GeV.

	Centrality / $\sqrt{s_{\mathrm{NN}}}$ (GeV)	0-5%	5-10%	10-20%	20-30%	30-40%	40-50%	50-60%	60-70%	70-80%
$\langle N_{part} \rangle$	**7.7**	337	290	226	160	110	72	45	26	14
	11.5	338	291	226	160	110	73	45	26	14
	19.6	338	289	225	158	108	71	44	26	14
	27	343	299	234	166	114	75	47	27	14
	39	342	294	230	162	111	74	46	26	14
	54.4	346.2	292.2	227.7	160.9	110.5	72.7	44.8	25.5	13.2
	62.4	346.5	293.9	229.8	164.1	114.3	76.3	47.9	27.8	15.3
	200	350.6	298.6	234.3	167.6	117.1	78.3	49.3	28.8	15.7
N_{ch}	**7.7**	270	225	155	105	68	41	23	11	5
	11.5	343	287	199	134	87	53	30	15	7
	19.6	448	376	263	178	116	71	40	20	7
	27	490	412	289	196	127	78	44	22	10
	39	522	439	308	209	136	83	47	24	11
	54.4	621	516	354	237	151	90	50	24	10
	62.4	571	482	338	230	149	91	51	26	12
	200	725	618	440	301	196	120	67	34	16

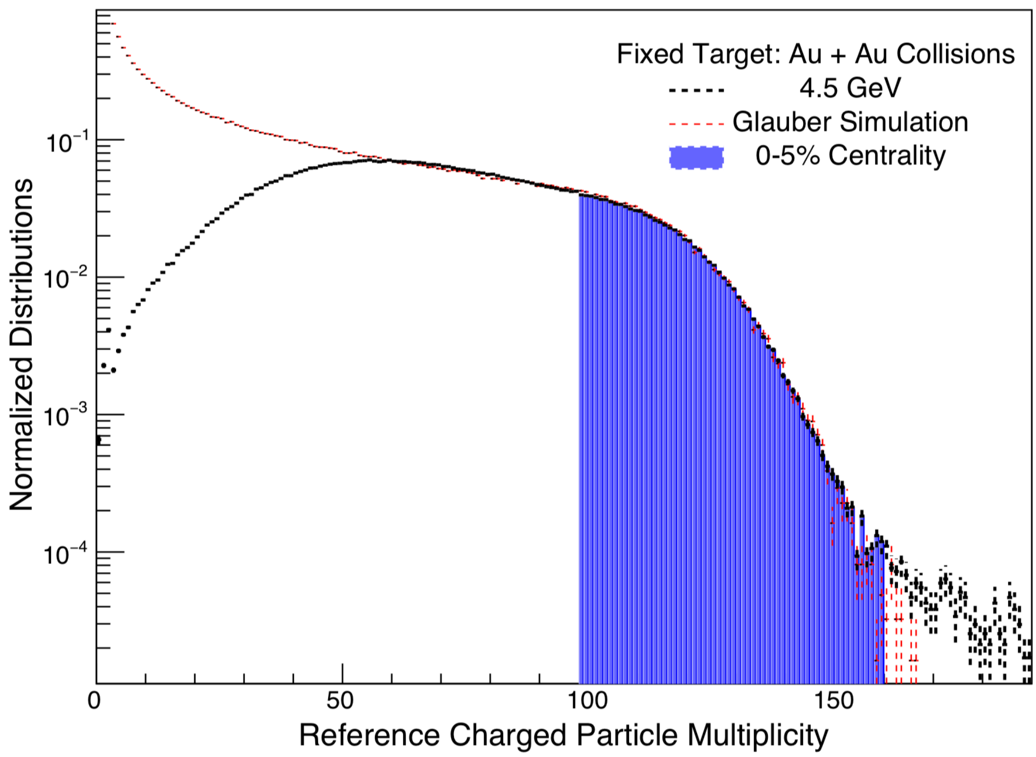

Fig. 3.18: (color online) Reference charged particle multiplicity (N_{ch}) distributions using only kaons and pions in $|\eta| < 1.0$ in FXT collisions at $\sqrt{s_{\mathrm{NN}}}$ = 4.5 GeV.

Tab. 3.6: $\langle N_{part} \rangle$ and N_{ch} for FXT collisions at $\sqrt{s_{\mathrm{NN}}} = 4.5$ GeV

Centrality	0-5%	5-10%	10-20%	20-30%	30-40%	40-50%	50-60%	60-70%	70-80%
$\langle N_{part} \rangle$	331	286	223	157	111	73	46	23	12
N_{ch}	99	82	56	37	24	14	8	4	2

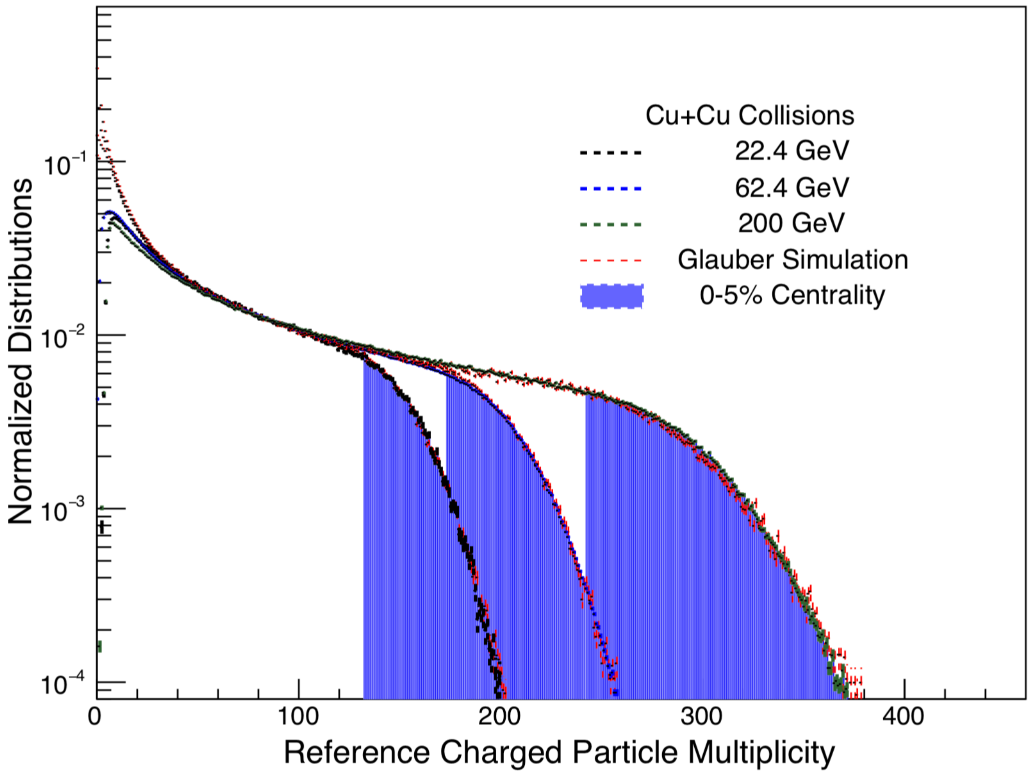

Fig. 3.19: (color online) Reference charged particle multiplicity (N_{ch}) distributions using only kaons and pions in $|\eta| < 1.0$ in Cu+Cu collisions at $\sqrt{s_{\mathrm{NN}}} = 22.4$, 62.4 and 200 GeV.

Tab. 3.7: $\langle N_{part} \rangle$ and N_{ch} for Cu+Cu collisions at $\sqrt{s_{\mathrm{NN}}} = 22.4$, 62.4 and 200 GeV.

	Centrality / $\sqrt{s_{\mathrm{NN}}}$ (GeV)	0-5%	5-10%	10-20%	20-30%	30-40%	40-50%	50-60%	60-70%	70-80%
$\langle N_{part} \rangle$	22.4	109	106	98	81	59	41	27	18	11
	62.4	113	110	102	86	62	42	28	18	11
	200	113	110	99	76	54	36	24	15	9
N_{ch}	22.4	128	108	76	53	36	23	15	9	5
	62.4	174	153	115	85	58	38	24	15	9
	200	236	198	138	80	53	34	21	13	7

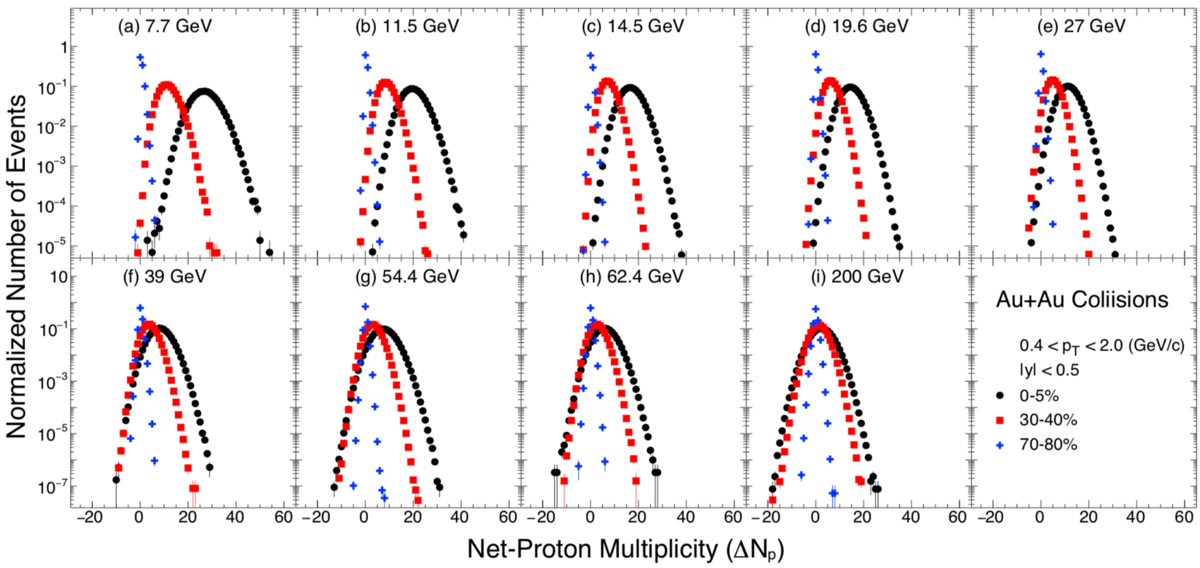

Fig. 3.20: (color online) Net-proton multiplicity distributions for Au+Au collisions at $\sqrt{s_{\mathrm{NN}}} = 7.7$, 11.5, 14.5, 19.6, 27, 39, 54.4, 62.4 and 200 GeV for three centralities (0-5%, 30-40% and 70-80%) at mid-rapidity. The distributions are not corrected for the finite centrality width effect nor for (anti-)proton reconstruction efficiency.

distributions are not corrected for the finite centrality width effect nor for (anti-)proton reconstruction efficiency. The center and width of a distribution are the mean value and standard deviation of the distribution correspondingly. It's easily to see that, the most central (0-5%) collisions have the more larger mean value and more widder distribution for a fixed energy. The net-proton multiplicity distribution has the more larger mean value and more wider distribution for a fixed centrality at low energy.

3.4.2 For Fixed-Target Collisions

Fig. 3.21 shows event-by-event proton multiplicity distributions for Au+Au collisions FXT mode at $\sqrt{s_{\mathrm{NN}}} = 4.5$ GeV for three centralities (0-5%, 30-40% and 70-80%). The distributions are not corrected for the finite centrality width effect nor for proton reconstruction efficiency. The center and width of a distribution are the mean value and standard deviation of the distribution correspondingly. It's easily to see that, the most central (0-5%) collisions have the more larger mean value and more width distribution for a fixed energy. The low energy has the more larger mean value and more width distribution for a fixed centrality.

3.4.3 For Cu+Cu Collisions

Fig. 3.22 shows event-by-event net-proton multiplicity distributions for Cu+Cu collisions at $\sqrt{s_{\mathrm{NN}}} = 22.4$, 62.4 and 200 GeV for three centralities (0-5%, 30-40% and 70-80%) at mid-rapidity within $0.4 < p_{\mathrm{T}} < 0.8\,(\mathrm{GeV}/c)$. The distributions are not corrected for the finite centrality width effect. The center and width of a distribution are the mean value and standard deviation of the distribution correspondingly. It's easily to see that, the most central (0-5%) collisions have larger mean value and wider distribution for a fixed energy. The low energy has the more larger mean value and more width distribution for a fixed centrality.

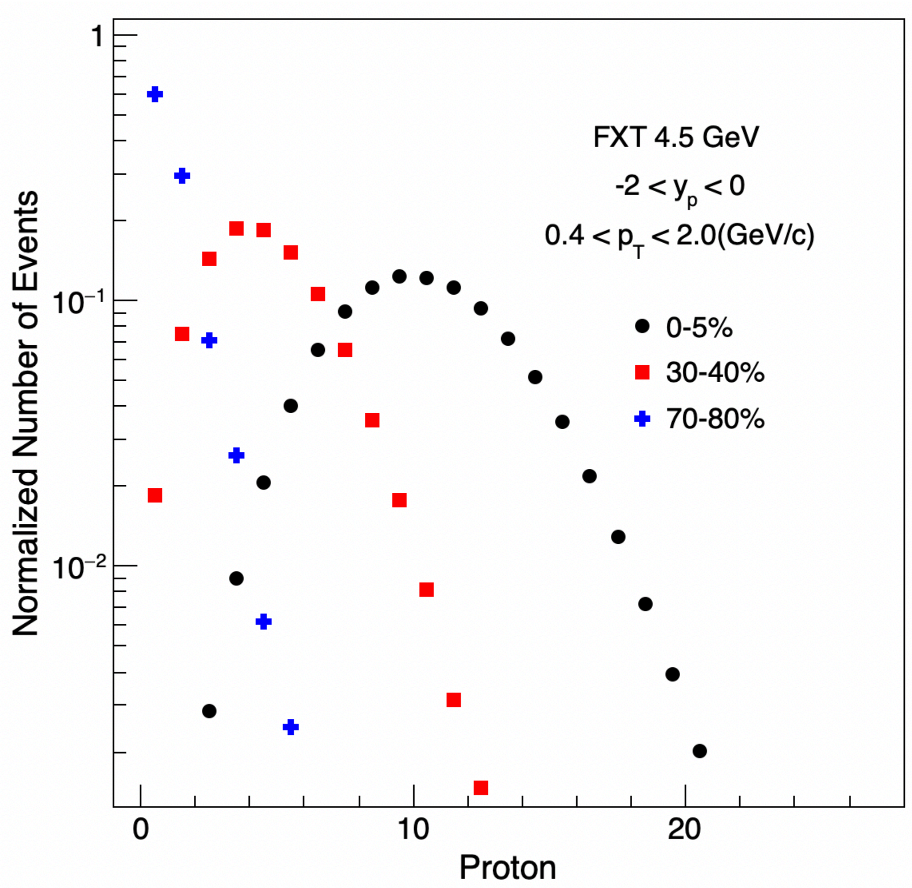

Fig. 3.21: (color online) Proton multiplicity distributions for Au+Au collisions FXT mode at $\sqrt{s_{\mathrm{NN}}} = 4.5$ GeV for three centralities (0-5%, 30-40% and 70-80%). The distributions are not corrected for the finite centrality width effect nor for proton reconstruction efficiency.

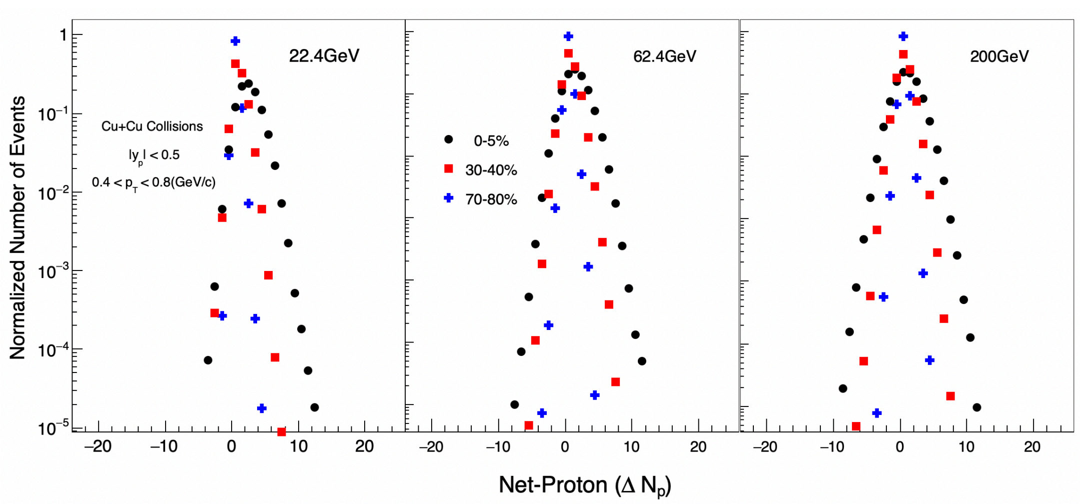

Fig. 3.22: (color online) Net-proton multiplicity distributions for Cu+Cu collisions at $\sqrt{s_{\mathrm{NN}}} = 22.4$, 62.4 and 200 GeV for three centralities (0-5%, 30-40% and 70-80%) at mid-rapidity within $0.4 < p_{\mathrm{T}} < 0.8\,(\mathrm{GeV}/c)$. The distributions are not corrected for the finite centrality width effect nor for (anti-)proton reconstruction efficiency.

3.5 Centrality Bin Width Correction

Usually, we present results in a wider centrality bin, such as 0-5%, 5-10%,...to have smaller statistical error. However, different centrality bin width will have different results. So, in order to decrease the centrality bin width effect, we have proposed a analysis approach to calculate the moments, that is the Centrality Bin Width Correction (CBWC)[55, 56]. The basic idea is in every centrality bin, taking weighted averaged for every multiplicity bins:

$$C_n = \sum_i w_i C_{n,i} \tag{3.3}$$

$$w_i = \frac{n_i}{\sum_i n_i}, \tag{3.4}$$

where $C_{n,i}$ is the n-th cumulant in i-th multiplicity bins in the centrality determination, n_i is the number of events in the i-th multiplicity bin and w_i is the corresponding weight. Fig. 3.23 shows cumulants of net-proton distributions as a function of $\langle N_{part}\rangle$ from Au+Au collisions at $\sqrt{s_{\mathrm{NN}}} = 7.7$, 19.6 and 62.4 GeV. The results are shown with a default centrality bin width corrected one and three different centrality bins (10%, 5% and 2.5%) without centrality bin width correction. The results from the largest centrality bin without CBWC have larger deviation from the default one with CBWC, and the results from smallest centrality bin without CBWC are close to the default one with CBWC. So the CBWC is important for the higher moments analysis.

3.6 Efficiency Correction

All the detectors at STAR have finite detecting efficiency in tracking the charged particles. Usually, it's not straightforward to get the efficiency corrected results for higher cumulants directly, the basic idea is to treat the probability of detection efficiency as a function of binomial distribution[57–62]. According to the definition Eq. 1.76, we usually use ε to represent the detecting efficiency of the detector, then the the probability distribution function of the binomial distribution can be expressed as:

$$B(k; N, \varepsilon) = \frac{N!}{k!(N-k)!}\varepsilon^k(1-\varepsilon)^{N-k} \tag{3.5}$$

where N is the produced particles and k is the measured particles.

3.6.1 For Au+ Au Collisions

In the STAR experiment, the TPC tracking efficiency are estimated by embedding technique.

$$\varepsilon_{TPC}(p_T) = \frac{N_{reconstruction}}{N_{embed}} \tag{3.6}$$

Fig. 3.24 shows the TPC efficiency as a function of p_T for proton and anti-proton within mid-rapidity at $\sqrt{s_{\mathrm{NN}}} = 7.7$, 11.5, 14.5, 19.6, 27, 39, 62.4 GeV.

The TOF efficiency is given by the ratio between the number of tracks detected by TOF and the number of tracks detected by TPC. It can be written as:

$$\varepsilon_{TOF} = \frac{N_{(|n\sigma_p|<2\&0.6<m^2<1.2)}}{N_{(|n\sigma_p|<2)}} \tag{3.7}$$

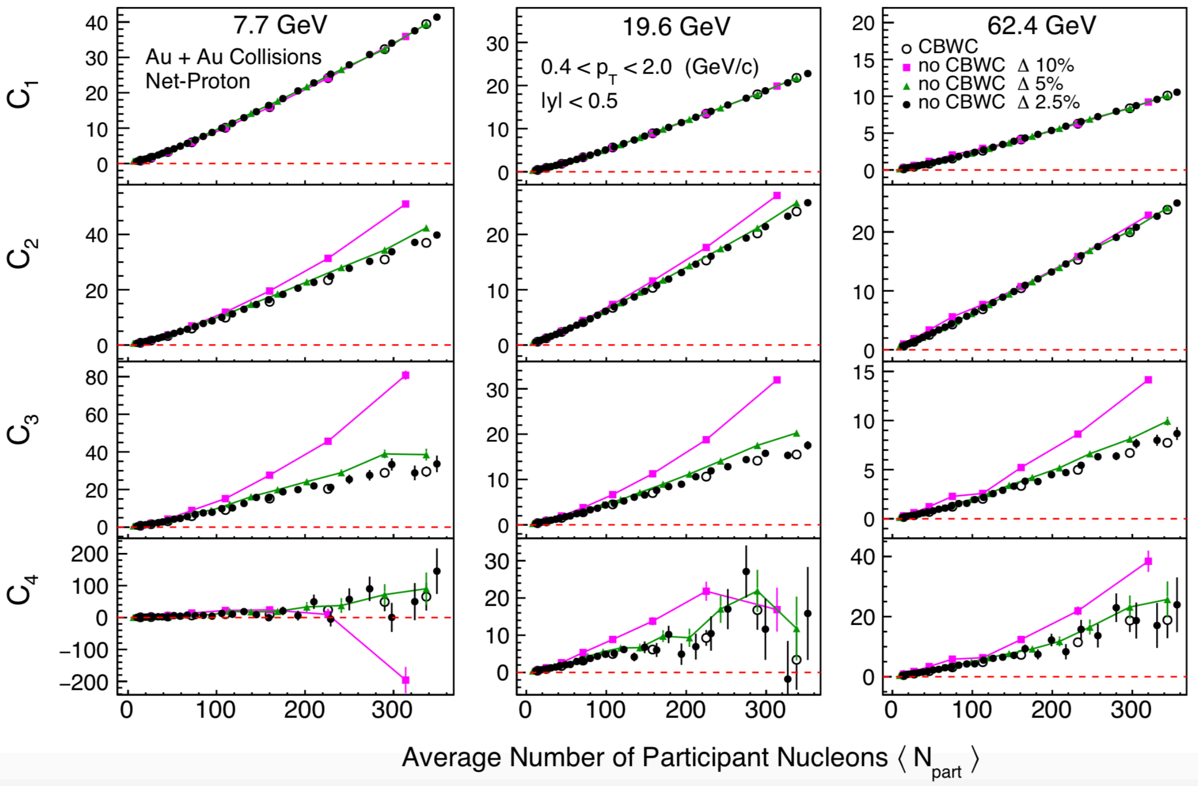

Fig. 3.23: (color online) C_1, C_2, C_3 and C_4 of net-proton distributions from Au+Au collisions at $\sqrt{s_{\rm NN}}$ = 7.7, 19.6 and 62.4 GeV as a function of $\langle N_{part} \rangle$. The results are shown for 10%, 5% and 2.5% centrality bins without CBWC and for 9 centrality with CBWC. The bars are statistical errors.

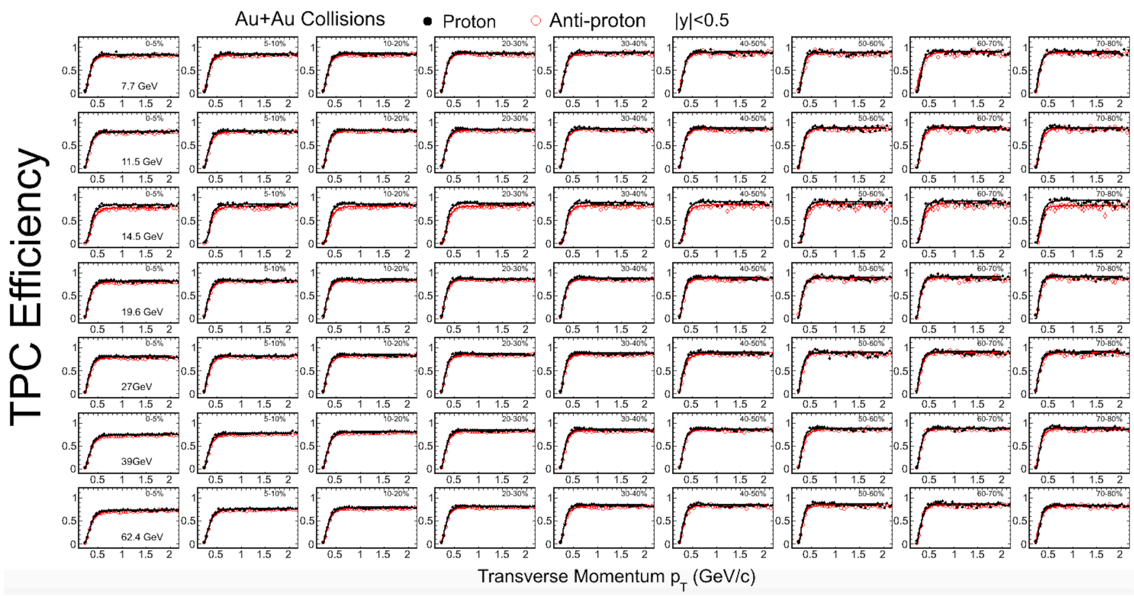

Fig. 3.24: The efficiencies for detecting protons and anti-protons as a function of p_T for proton and anti-proton within mid-rapidity at $\sqrt{s_{\rm NN}}$ = 7.7, 11.5, 14.5, 19.6, 27, 39, 62.4 GeV.

The final efficiency used in our analysis is the averaged efficiency of TPC and TOF, the formula is:

$$\langle\varepsilon\rangle = \frac{\int_a^b \varepsilon(p_T)f(p_T)p_T dp_T}{\int_a^b f(p_T)p_T dp_T} \tag{3.8}$$

where $\varepsilon(p_T)$ is the transverse momentum dependence efficiency, $f(p_T)$ is the efficiency corrected transverse momentum spectra for (anti-)proton, (a, b) is the momentum range.

In the momentum analysis, if the spectra of proton and anti-proton is known. And in the lower p_T range, only TPC is used, in the higher p_T range, both TPC and TOF are used. Thus, according the above efficiency formula, we can obtain the averaged efficiency for proton and anti-proton at low and high p_T range. Then, we can get the various order efficiency corrected cumulants for proton, anti-proton and net-proton.

The averaged efficiency for proton and anti-proton at low and high p_T range can be written as:

$$\langle\varepsilon_{p(\bar{p})l}\rangle = \frac{\int_{0.4}^{0.8} \varepsilon_{TPC} f(p_T)p_T dp_T}{\int_{0.4}^{0.8} f(p_T)p_T dp_T} \tag{3.9}$$

$$\langle\varepsilon_{p(\bar{p})h}\rangle = \frac{\int_{0.8}^{2.0} \varepsilon_{TPC}\varepsilon_{TOF} f(p_T)p_T dp_T}{\int_{0.8}^{2.0} f(p_T)p_T dp_T} \tag{3.10}$$

Fig. 3.25 shows the averaged efficiency as a function of collision centrality for proton and anti-proton for lower p_T range $(0.4 < p_{\mathrm{T}} < 0.8\,(\mathrm{GeV}/c)\,)$ and higher p_T range $(0.8 < p_{\mathrm{T}} < 2.0\,(\mathrm{GeV}/c)\,)$ at $\sqrt{s_{\mathrm{NN}}} = 7.7$, 11.5, 14.5, 19.6, 27, 39, 54.4, 62.4 and 200 GeV.

If the proton and anti-proton have same detecting efficiency, $\varepsilon_p = \varepsilon_{\bar{p}}$, then the various order efficiency corrected cumulants for net-proton can be expressed as the terms of the efficiency and the measured cumulants:

$$C_1^{N_p-N_{\bar{p}}} = \frac{\langle n_p\rangle - \langle n_{\bar{p}}\rangle}{\varepsilon} \tag{3.11}$$

$$C_2^{N_p-N_{\bar{p}}} = \frac{C_2^{n_p-n_{\bar{p}}} + (\varepsilon-1)(\langle n_p\rangle + \langle n_{\bar{p}}\rangle)}{\varepsilon^2} \tag{3.12}$$

$$C_3^{N_p-N_{\bar{p}}} = \frac{C_3^{n_p-n_{\bar{p}}} + 3(\varepsilon-1)(C_2^{n_p} - C_2^{n_{\bar{p}}}) + (\varepsilon-1)(\varepsilon-2)(\langle n_p\rangle - \langle n_{\bar{p}}\rangle)}{\varepsilon^3} \tag{3.13}$$

$$\begin{aligned} C_4^{N_p-N_{\bar{p}}} &= \frac{C_4^{n_p-n_{\bar{p}}} - 2(\varepsilon-1)C_3^{(n_p-n_{\bar{p}}} + 8(\varepsilon-1)(C_3^{n_p} + C_3^{n_{\bar{p}}})}{\varepsilon^4} \\ &+ \frac{(5-\varepsilon)(\varepsilon-1)C_2^{n_p-n_{\bar{p}}} + 8(\varepsilon-1)(\varepsilon-2)(C_2^{n_p} + C_2^{n_{\bar{p}}})}{\varepsilon^4} \\ &+ \frac{(\varepsilon^2-6\varepsilon+6)(\varepsilon-1)(\langle n_p\rangle + \langle n_{\bar{p}}\rangle)}{\varepsilon^4} \end{aligned} \tag{3.14}$$

However, the efficiency of proton and anti-proton will depend on the phase space (y, p_T and ϕ). For simplicity, we only consider two subspace phase, the low p_T and high p_T range. In the two subspace, the efficiencies of proton and anti-proton are constant. Then the multivariate factorial moments of proton and anti-proton distributions can be easily corrected according to the efficiency corrected formula:

$$F_{u,v,i,j}(N_{pl}, N_{ph}, N_{\bar{p}l}, N_{\bar{p}h}) = \frac{f_{u,v,i,j}(n_{pl}, n_{ph}, n_{\bar{p}l}, n_{\bar{p}h})}{(\varepsilon_{pl})^u(\varepsilon_{ph})^v(\varepsilon_{\bar{p}l})^i(\varepsilon_{\bar{p}h})^j}$$

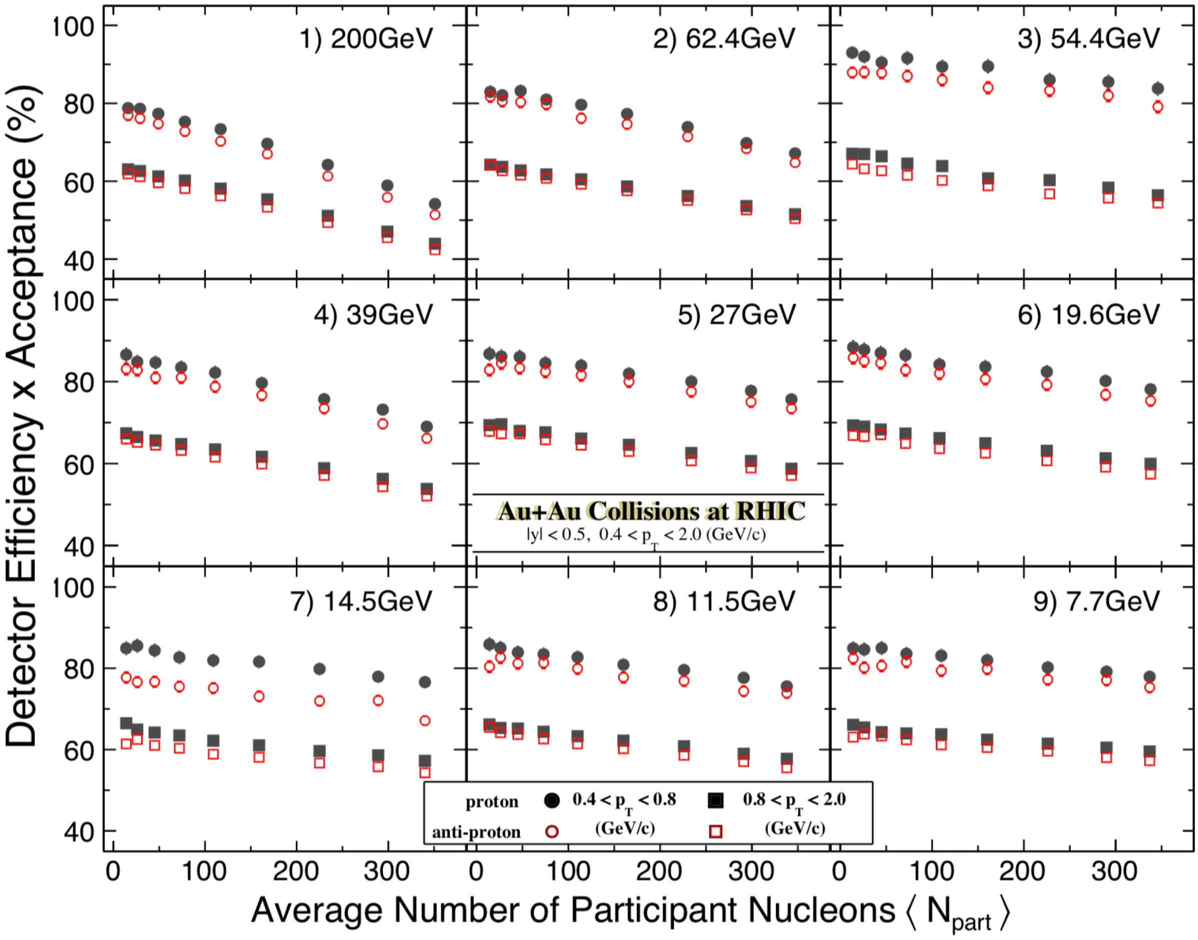

Fig. 3.25: (color online) The averaged efficiency as a function of collision centrality for proton and anti-proton for lower p_T range ($0.4 < p_{\mathrm{T}} < 0.8\,(\mathrm{GeV}/c)$) and higher p_T range ($0.8 < p_{\mathrm{T}} < 2.0\,(\mathrm{GeV}/c)$) at $\sqrt{s_{\mathrm{NN}}}$ = 7.7, 11.5, 14.5, 19.6, 27, 39, 54.4, 62.4 and 200 GeV.

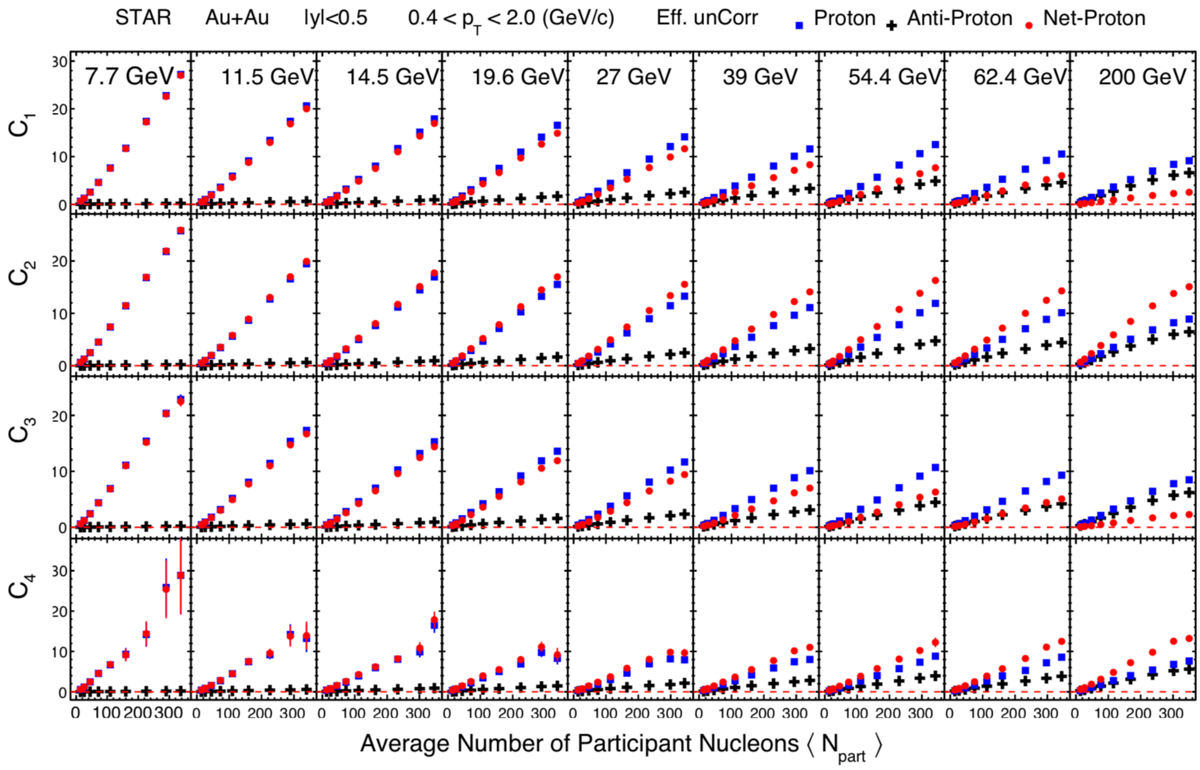

Fig. 3.26: (color online) Centrality dependence of C_1, C_2, C_3 and C_4 for proton, anti-proton and net-proton distributions in Au+Au collisions at $\sqrt{s_{\rm NN}}$ = 7.7 −200 GeV. The results are CBW-corrected but not are corrected for proton and anti-proton reconstruction efficiency. The bars are statistical errors.

where $\varepsilon_{pl}, \varepsilon_{ph}, \varepsilon_{\bar{p}l}$, and $\varepsilon_{\bar{p}h}$ are the proton and anti-proton efficiencies in the two subspace, which we have discussed in the figure Fig. 3.25, $n_{pl}, n_{ph}, n_{\bar{p}l}, n_{\bar{p}h}$ are the number of proton and anti-proton, $f_{u,v,j,k}(n_{pl}, n_{ph}, n_{\bar{p}l}, n_{\bar{p}h})$ is the measured multivariate factorial moments of proton and anti-proton multiplicity distributions and $F_{u,v,i,j}(N_{pl}, N_{ph}, N_{\bar{p}l}, N_{\bar{p}h})$ is the true multivariate factorial moments. More details about the efficiency correction you can find [57]. Fig. 3.26 shows the centrality dependence of efficiency uncorrected C_n for proton, anti-proton and net-proton multiplicity distributions in Au+Au collisions at $\sqrt{s_{\rm NN}}$ = 7.7 −200 GeV. The results are CBW-corrected but not are corrected for proton and anti-proton reconstruction efficiency.

3.6.2 For Fixed-Target Collisions

Fig. 3.27 shows the TPC efficiency for proton as a function of p_T for FXT collisions at $\sqrt{s_{\rm NN}}$ = 4.5 GeV.

3.7 Uncertainty Estimation

3.7.1 Statistical Error Estimation

We usually use the general error formula to calculate the statistical errors of cumulants and cumulant ratios of net-proton multiplicity distributions based on the Delta

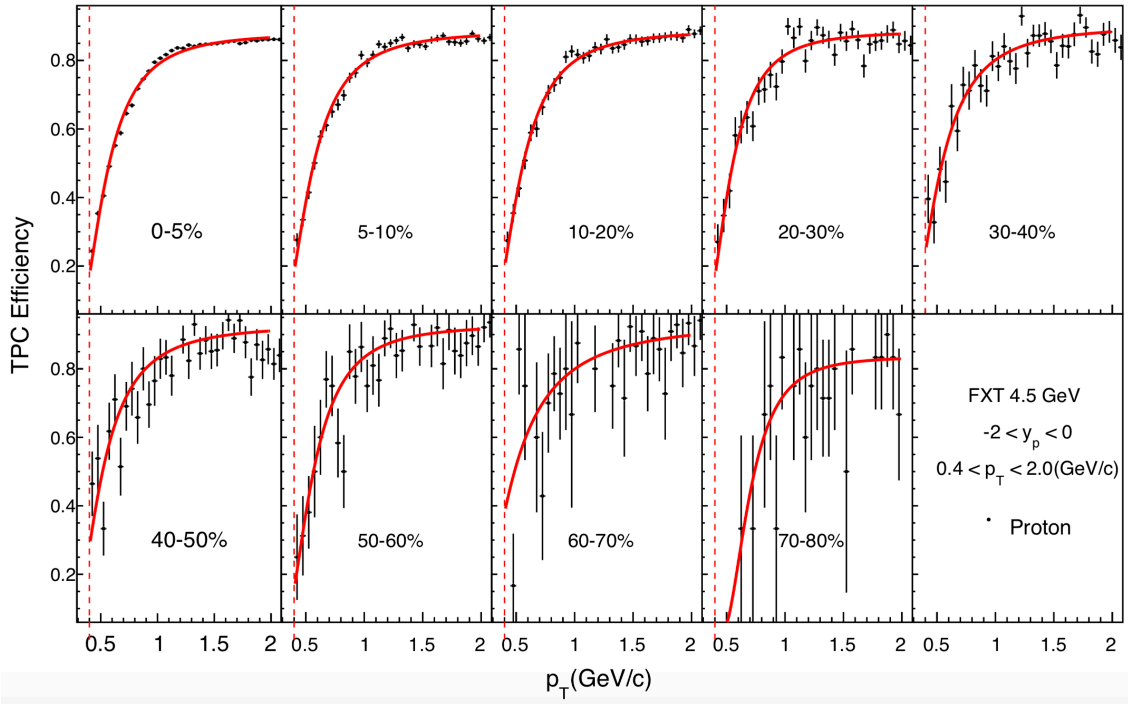

Fig. 3.27: (color online) The TPC efficiency for proton as a function of p_T for FXT collisions at $\sqrt{s_{\mathrm{NN}}} = 4.5$ GeV.

theorem[63]:

$$V(\psi) = \sum_{i=1,j=1}^{n} \frac{\partial \psi}{\partial X_i} \frac{\partial \psi}{\partial Y_i} Cov(X_i, Y_j)$$
$$= \sum_{i=1}^{n} (\frac{\partial \psi}{\partial X_i})^2 V(X_i) + \sum_{i=1,j=1,i \neq j}^{n} \frac{\partial \psi}{\partial X_i} \frac{\partial \psi}{\partial Y_i} Cov(X_i, Y_j) \tag{3.15}$$

where $V(X_i)$ and $V(Y_j)$ are the variance of the random X_i and Y_j, and $Cov(X_i, Y_j)$ is the covariance of random X_i and Y_j. The covariance $Cov(X_i, Y_j)$ can be written as the terms of the multivariate moments, which are easily efficiency corrected. Then we have the following relationship between the statistical errors and the efficiency, the variance and statistics:

$$Error(C_n) \propto \frac{\sigma^n}{\sqrt{n}\varepsilon^n} \tag{3.16}$$

$$Error(S\sigma) \propto \frac{\sigma}{\sqrt{n}\varepsilon^{3/2}} \tag{3.17}$$

$$Error(\kappa\sigma^2) \propto \frac{\sigma^2}{\sqrt{n}\varepsilon^2} \tag{3.18}$$

where σ is the width of the distribution, n is the number of events, and ε is the efficiency. Fig. 3.28 shows the statistical errors of the efficiency corrected cumulant ratios as a function of efficiency for a Skellam distribution with 1 million statistics according to the delta theorem. The statistical errors of the cumulant ratios are proportional to the power of the standard deviation and are dramatically increase with the decreasing efficiency

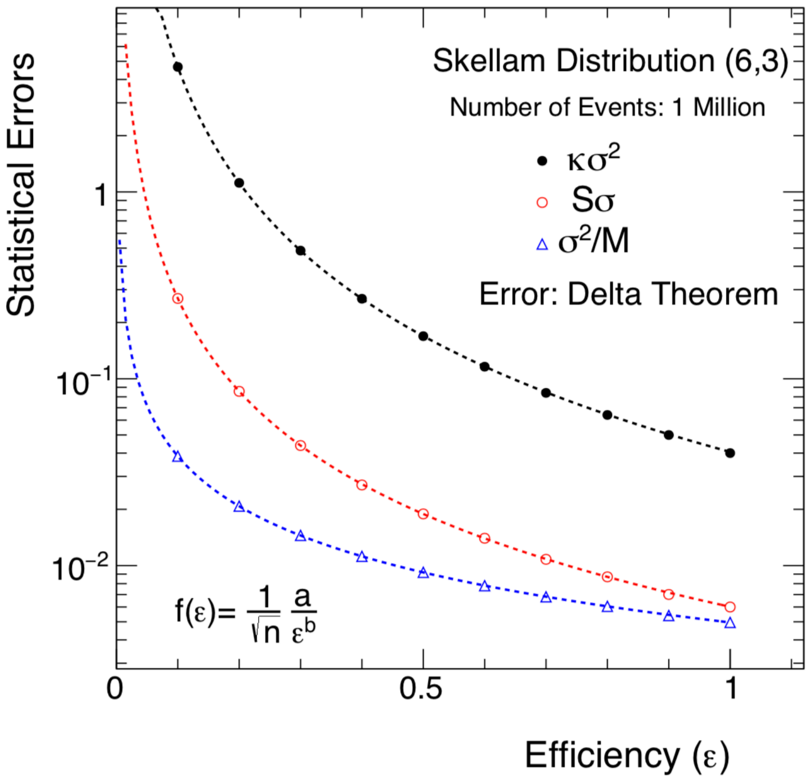

Fig. 3.28: The statistical errors of efficiency corrected cumulant ratios ($\kappa\sigma^2, S\sigma$ and σ^2/M) as a function of efficiency for a Skellam distribution with 1 million statistics according to the Delta theorem[57].

number. These data points can be fitted with functional form:

$$f(\varepsilon) = \frac{1}{\sqrt{n}}\frac{a}{\varepsilon^b} \tag{3.19}$$

where n is the number of events which is fixed to be one million here, a and b are free parameters. The fitting parameters of a and b are 40.6 and 2.06 for $\kappa\sigma^2$, 6.02 and 1.65 for $S\sigma$, 4.96 and 0.89 for σ^2/M, respectively.

3.7.2 Systematic Error Estimation

To estimate systematic uncertainties in the higher moment analysis, we varied 4 track cuts (d_{ca}, nFitPts, $n\sigma_p$, m^2) and TPC/TOF efficiency (ε), which are listed in the Tab. 3.8. The d_{ca} mainly controls the fraction of background protons which are knocked out from the beam pipe by other particles [50]. The selection of a sufficiently large number of fit points can suppress track splitting in the TPC. The purity of the proton samples can be controlled by the Z variable of the ionization energy loss for the protons. The quality cuts such as d_{ca}, nFitPts, $n\sigma_p$, m^2 and $\varepsilon(\varepsilon_l, \varepsilon_h)$ are used to estimate the systematic errors. The default cuts used in the analysis are: $d_{ca} < 1$, nFitPts > 20, $|n\sigma_p| < 2$, $0.6 < m^2 < 1.2$ and $\varepsilon(\varepsilon_l, \varepsilon_h)$. When we vary one set of the cuts, the other sets of cuts stick to the default value. For each set of the cuts, we can calculate the point by point difference between the various cuts and the default cuts. The systematic errors from one kind of cuts σ_{Y_i} can be calculated as the square root of the sum of these

Tab. 3.8: The track cuts (d_{ca}, nFitPts, $n\sigma_p$, m^2) and TPC/TOF efficiency (ε) are used to calculate the systematic errors.

Variable	Default Cut	Changed Cut			
$\boldsymbol{d_{ca}}$	< 1.0	< 0.8	< 0.9	< 1.1	<1.2
nFitPts	> 20	> 15	> 18	> 22	> 25
$\boldsymbol{n\sigma_p}$	<2.0	< 1.6	< 1.8	< 2.2	<2.5
$\boldsymbol{m^2}$	$0.6 < m^2 <1.2$	$0.5 < m^2 < 1.1$		$0.55 < m^2 < 1.15$	
		$0.65 < m^2 < 1.25$		$0.7 < m^2 < 1.3$	
Efficiency$(\boldsymbol{\varepsilon})$	$(\varepsilon_{pl},\ \varepsilon_{ph}, \varepsilon_{\bar{p}l},\ \varepsilon_{\bar{p}h})$	$1.05\ \times(\ \varepsilon_{pl},\ \varepsilon_{ph}, \varepsilon_{\bar{p}l},\ \varepsilon_{\bar{p}h})$			
		$0.95\ \times\ (\varepsilon_{pl},\ \varepsilon_{ph}, \varepsilon_{\bar{p}l},\ \varepsilon_{\bar{p}h})$			

differences:

$$\sigma_{Y_i} = \sqrt{\frac{1}{m}\sum_{j}^{m}(Y_{i,j} - Y_{default})^2} \tag{3.7.20}$$

where $Y_{i,j}$ and $Y_{default}$ are the observables from various sets of systematic cuts (dca, nfitPts, $n\sigma_p$, m^2 and $\varepsilon(\varepsilon_l,\ \varepsilon_h)$) and default cuts respectively, and m is the number of each set of the cuts.

Then the total systematic errors $\sigma_{Y_{sys}}$ can be calculated as the square root of the sum of the errors from all sets of cuts:

$$\sigma_{Y_{sys}} = \sqrt{\sum_{i}^{n}(\sigma_{Y_i})^2} \tag{3.7.21}$$

For example,

$$\sigma_{Y_{dca}} = \sqrt{\frac{1}{4}\sum_{j=1}^{4}(Y_{dca,j} - Y_{default})^2}, \quad \sigma_{Y_\varepsilon} = \sqrt{\frac{1}{2}\sum_{j=1}^{2}(Y_{\varepsilon,j} - Y_{default})^2} \tag{3.7.22}$$

$$\sigma_{Y_{sys}} = \sqrt{\sigma^2_{Y_{dca}} + \sigma^2_{Y_{nFitPts}} + \sigma^2_{Y_{n\sigma_p}} + \sigma^2_{Y_{m^2}} + \sigma^2_{Y_\varepsilon}} \tag{3.7.23}$$

Fig. 3.29 shows the centrality dependence of efficiency corrected cumulants and their ratios for net-proton distributions with the the changes in above selection criteria in Au + Au collisions at $\sqrt{s_{\rm NN}} = 200$ GeV. The systematic uncertainties on the measurements are obtained according to the Eq. 3.7.23. Tab. 3.9 shows the systematic errors of net-proton cumulants for most central $(0-5\%)$ Au + Au collisions at $\sqrt{s_{\rm NN}} = 7.7$, 11.5, 14.5, 19.6, 27, 39, 54.4, 62.4 and 200 GeV.

3.7.3 Barlow Check on Net-Proton Systematic Errors

We must make sure that the systematic errors are not simply accounting for statistical fluctuations. Then the distribution of $\frac{\Delta Y}{\sigma_B}$ for each systematic variation are constructed

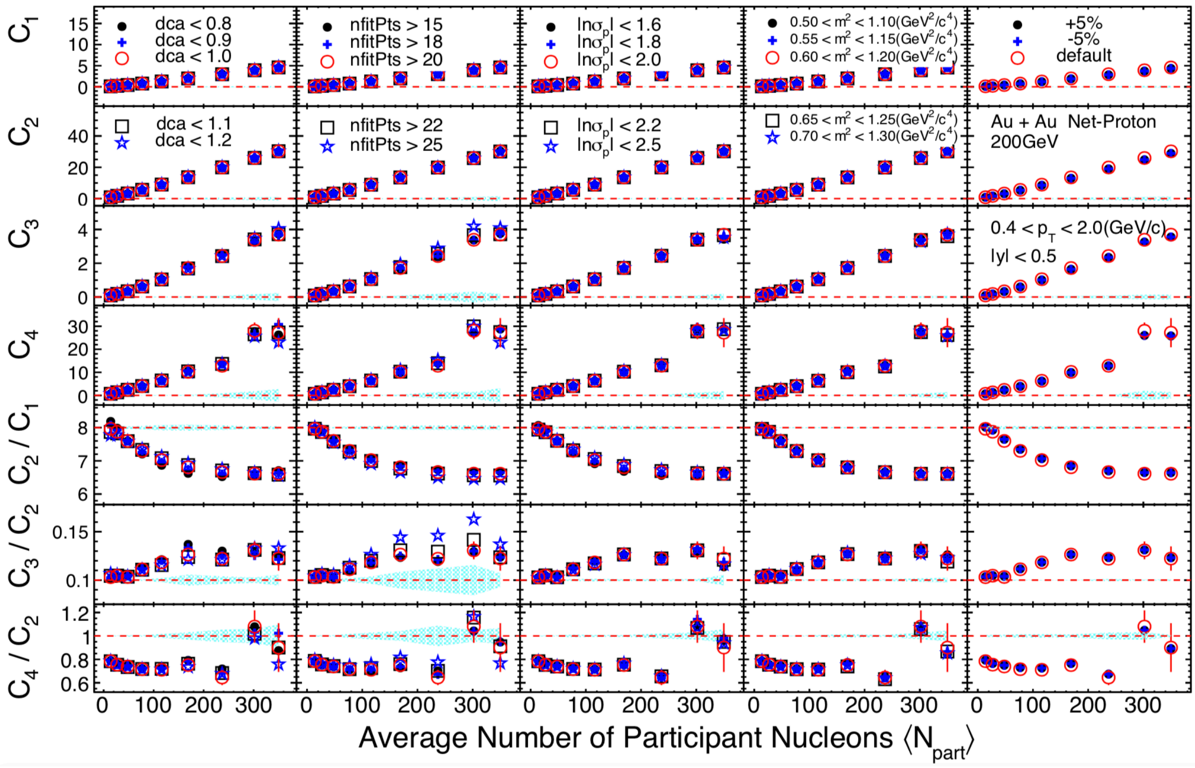

Fig. 3.29: (color online) Cumulants and their ratios as a function of $\langle N_{part} \rangle$, for net-proton distributions with variation of track selection (d_{ca}, nFitPts), particle identification ($n\sigma_p$, m^2) and $\varepsilon(\varepsilon_l, \varepsilon_h)$ and systematic errors within $|y| < 0.5$ and $0.4 < p_{\mathrm{T}} < 2.0\,(\mathrm{GeV}/c)$ in Au + Au collisions at $\sqrt{s_{\mathrm{NN}}} = 200$ GeV.

Tab. 3.9: Total systematic uncertainty as well as uncertainties from individual sources on net-proton C_n in Au+Au collisions at $\sqrt{s_{\mathrm{NN}}} = 7.7 - 200$ GeV.

$\sqrt{s_{\mathrm{NN}}}$ (GeV)	Cumulants	Sys. Uncert.	d_{ca}	nFitPts	$n\sigma_p$	m^2	Efficiency
7.7	C_1	2.42	0.849	0.784	0.987	0.028	1.877
	C_2	2.03	0.724	0.598	0.819	0.032	1.607
	C_3	1.65	0.60	0.971	0.537	0.314	1.02
	C_4	16.20	5.56	12.544	6.40	2.68	5.11
11.5	C_1	2.82	1.76	1.027	1.129	0.033	1.59
	C_2	2.34	1.439	0.733	0.986	0.0197	1.37
	C_3	1.36	0.642	0.195	0.854	0.035	0.822
	C_4	7.37	2.278	4.099	4.941	2.6	1.062
14.5	C_1	1.72	0.766	0.538	0.763	0.029	1.22
	C_2	1.60	0.693	0.494	0.742	0.021	1.13
	C_3	1.16	0.517	0.437	0.511	0.047	0.779
	C_4	8.06	2.89	3.10	5.412	0.714	4.15
19.6	C_1	1.46	0.604	0.618	0.556	0.045	1.03
	C_2	1.46	0.619	0.619	0.573	0.041	1.02
	C_3	0.678	0.363	0.256	0.228	0.132	0.44
	C_4	3.65	0.856	1.987	2.58	0.585	0.89
27	C_1	1.20	0.508	0.527	0.468	0.025	0.832
	C_2	1.44	0.666	0.627	0.568	0.027	0.961
	C_3	0.62	0.332	0.265	0.232	0.035	0.389
	C_4	3.10	1.58	1.36	1.80	0.375	1.360
39	C_1	0.941	0.393	0.446	0.347	0.026	0.641
	C_2	1.48	0.668	0.671	0.594	0.033	0.970
	C_3	0.506	0.287	0.209	0.174	0.041	0.313
	C_4	3.346	0.9996	2.7642	1.428	0.196	0.646
54.4	C_1	0.805	0.430	0.332	0.203	0.034	0.557
	C_2	1.57	0.878	0.646	0.388	0.065	1.06
	C_3	0.418	0.269	0.147	0.078	0.024	0.272
	C_4	2.92	1.17	1.39	1.91	1.23	0.212
62.4	C_1	1.0345	0.449	0.492	0.351	0.044	0.709
	C_2	2.147	1.046	1.087	0.786	0.113	1.306
	C_3	0.575	0.143	0.222	0.297	0.081	0.408
	C_4	3.99	2.40	2.30	1.38	1.21	1.23
200	C_1	0.390	0.190	0.237	0.111	0.01	0.217
	C_2	2.42	1.11	1.53	0.771	0.087	1.31
	C_3	0.390	0.241	0.183	0.192	0.074	0.136
	C_4	4.89	2.69	3.07	1.80	1.41	1.42

as the criteria for passing the Barlow check [64]. And we can calculate $\frac{\Delta Y}{\sigma_B}$ for each set of systematic cuts for all centralities.

$$\Delta Y = Y_{default} - Y_{sys}, \quad \sigma_B = \sqrt{\sigma_{default}^2 - \sigma_{sys}^2} \tag{3.7.24}$$

where $Y_{default}$ is the default value of an observable Y ($C_1, C_2, C_3, C_4, C_2/C_1, C_3/C_2$ and C_4/C_2) with statistical error $\sigma_{default}$, and Y_{sys} is the systematic value with statistical error σ_{sys}.

For the ideal case, the distribution of $\frac{\Delta Y}{\sigma_B}$ is Gaussian and satisfies the following criteria:

(i) Mean = 0

(ii) Std Deviation = 1

(iii) 68% entries within $|\frac{\Delta Y}{\sigma_B}| < 1$

(iv) 95% entries within $|\frac{\Delta Y}{\sigma_B}| < 2$

However, for the common case, criteria loosened in this study because of low counts, the distribution of $\frac{\Delta Y}{\sigma_B}$ satisfies at least 3 of the following 4 criteria for passing Barlow check:

(i) Mean = 0.3

(ii) Std Deviation = 1.3

(iii) $55\% - 68\%$ entries within $|\frac{\Delta Y}{\sigma_B}| < 1$

(iv) $80\% - 95\%$ entries within $|\frac{\Delta Y}{\sigma_B}| < 2$

We don't need to consider that systematic variation in the calculation of systematic errors when systematic variation passing the Barlow check. Fig. 3.30 shows the distribution of $\frac{\Delta Y}{\sigma_B}$ ($C_1, C_2, C_3, C_4, C_2/C_1, C_3/C_2$ and C_4/C_2) for all sets of systematic cuts (dca, nfitPts, $n\sigma_p, m^2$ and ε) in Au+Au collisions at $\sqrt{s_{\mathrm{NN}}}$ = 7.7 GeV for all centralities. It's obvious that the distributions of $\frac{\Delta Y}{\sigma_B}$ for dca, nfitPts, $n\sigma_p$ and m^2 cuts don't satisfy the Barlow check. Although the distributions for efficiency cuts satisfy the first two conditions, but 100% entries within $|\frac{\Delta Y}{\sigma_B}|$, that is to say, all sets of systematic cuts failed the Barlow check.

3.8 Model Study

Although our results can be compared to several models[17, 65–76], we have chosen two different models which do not have phase-transition or critical- point physics. They have contrasting physics processes to understand the following: (a) Effect of measuring net-protons instead of net-baryons [77, 78], (b) Role of resonance decay for net-baryon measurements[79–82], (c) Effect of finite p_{T} acceptance for the measurements[83, 84] and (d) Effect of net-baryon number conservation[77, 85, 86]. The model results also provide an appropriate baseline for comparison to data.

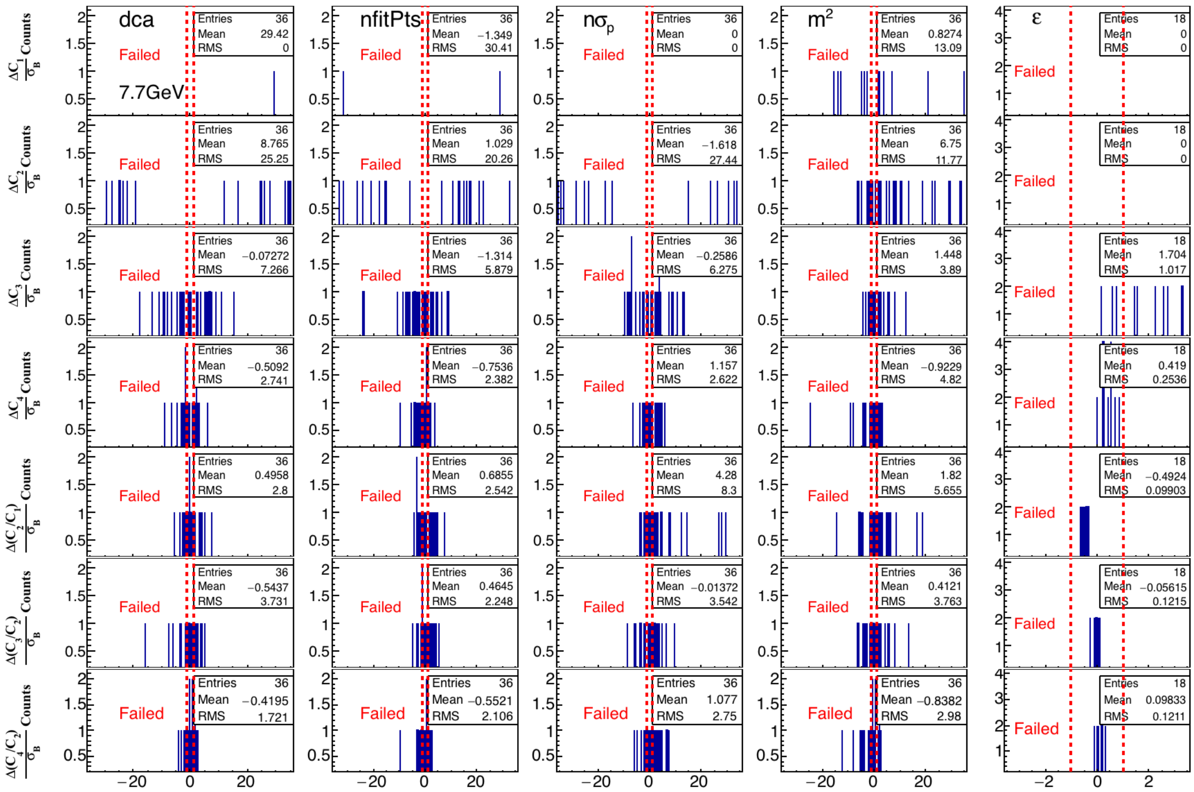

Fig. 3.30: Distribution of $\frac{\Delta Y}{\sigma_B}$(Y $= C_1, C_2, C_3, C_4, C_2/C_1, C_3/C_2$ and C_4/C_2) for all sets of systematic cuts (dca, nfitPts, $n\sigma_p, m^2$ and ε) in Au+Au collisions at $\sqrt{s_{\rm NN}} = 7.7$ GeV for all centralities.

3.8.1 Hadron Resonance Gas Model

The Hadron Resonance Gas (HRG) model includes all the relevant degrees of freedom for the hadronic matter and also implicitly take into account the interactions that are necessary for resonance formation[87, 88]. Hadrons and resonances of masses up to 3 GeV/c are included. Considering a Grand Canonical Ensemble picture, the logarithm of the partition function (Z) in the HRG model is given as:

$$LnZ(T,V,\mu) = \sum_{B} lnZ_i(T,V,\mu_i) + \sum_{Z} lnZ_i(T,V,\mu_i) \tag{3.8.1}$$

where,

$$LnZ_i(T,V,\mu_i) = \pm\frac{Vg_i}{2\pi^2}\int dp^3\{1 \pm exp[(\mu_i - E)/T]\} \tag{3.8.2}$$

T is the temperature, V is the volume of the system, μ_i is the chemical potential, E is the energy and g_i is the degeneracy factor of the i^{th} particle. The total chemical potential $\mu_i = B_i\mu_B + Q_i\mu_Q + S_i\mu_S$, where B_i, Q_i and S_i are the baryon, electric charge and strangeness number of the i^{th} particle, with corresponding chemical potentials μ_B, μ_Q and μ_S, respectively. The "+" and "-" signs are for baryons (B) and mesons (M) respectively. The n^{th} order generalized susceptibility for baryons can be expressed as[88]:

$$\chi^{(n)}_{x,baryon} = \frac{x^n}{VT^3}\int dp^3 \sum_{k=0}^{\infty}(-1)^k(k+1)^n exp\{\frac{-(k+1)E}{T}\}exp\{\frac{(k+1)\mu}{T}\} \tag{3.8.3}$$

And for mesons,

$$\chi^{(n)}_{x,meson} = \frac{x^n}{VT^3}\int dp^3 \sum_{k=0}^{\infty}(k+1)^n exp\{\frac{-(k+1)E}{T}\}exp\{\frac{(k+1)\mu}{T}\} \tag{3.8.4}$$

The factor x represents either B, Q or S of the i^{th} particle depending on whether the computed χ_x represents baryon or electric charge or strangeness susceptibility.

For a particle of mass m with p_T, η and ϕ (azimuthal angle), the volume element (dp^3) and energy (E) can be written as $dp^3 = p_T m_T cosh\eta dp_T d\eta d\phi$ and $E = m_T cosh\eta$, where $m_T = \sqrt{p_T^2 + m^2}$. The experimental acceptance can be incorporated by considering the appropriate integration ranges in p_T, η, ϕ and charge states by considering the values of |x|. The total generalized susceptibilities will then be the sum of the contributions from baryons and mesons as, $\chi^{(n)}_x = \sum\chi^{(n)}_{x,baryon} + \sum\chi^{(n)}_{x,meson}$.

In order to make the connection to the experimental results, the beam-energy dependence of μ_B and T parameters of the HRG model need to be provided. This is obtained from the parameterization of μ_B and T as a function of $\sqrt{s_{\rm NN}}$ [89]. The μ_B dependence of the temperature is given as $T(\mu_B) = a - b\mu_B^2 - c\mu_B^4$ with $a = 0.166 \pm 0.002$ GeV, $b = 0.139 \pm 0.016$ GeV^{-2} and $c = 0.053 \pm 0.028$ GeV^{-3}. The energy dependence of μ_B is parameterized as $\mu_B(\sqrt{s_{\rm NN}}) = \frac{d}{1+e\sqrt{s_{\rm NN}}}$ with $d = (1.308 \pm 0.028)$ GeV and $e = (0.273 \pm 0.008)$ GeV^{-1}. Further, the ratio of baryon to strangeness chemical potential is parameterized as $\frac{\mu_S}{\mu_B} \simeq 0.164 \pm 0.018\sqrt{s_{\rm NN}}$.

3.8.2 UrQMD Model

The UrQMD (Ultra relativistic Quantum Molecular Dynamics) model[90, 91] is a microscopic transport model where the phase space description of the reactions are considered. It treats the propagation of all hadrons as classical trajectories in combination with stochastic binary scattering, color string formation and resonance decays. It incorporates baryon-baryon, meson-baryon and meson-meson interactions. The collisional term includes more than 50 baryon species and 45 meson species. The model preserves the conservation of electric charge, baryon number, and strangeness number as expected for QCD matter. It also models the phenomena of baryon-stopping, an essential feature encountered in heavy-ion collisions, at lower beam energies. In this model, the space-time evolution of the fireball is studied in terms of excitation and fragmentation of color strings and formation and decay of hadronic resonances. It can simulate heavy-ion collisions in the energy range from SIS (SchwerIonen Heavy-ion Synchrotron) to Relativistic Heavy Ion Collider and Large Hadron Collider. Since the model does not include the quark-hadron phase transition or the QCD critical point, the comparison of the data to the results obtained from the UrQMD model will shed light on the contributions from the hadronic phase and its associated processes, baryon number conservation and the effects of measuring only net-protons relative to net-baryons.

Chapter 4

Results

In this chapter, we will present the centrality, energy, rapidity, p_{T} and acceptance dependence of cumulants and cumulant ratios of proton, anti-proton and net-proton for Au+Au collisions at $\sqrt{s_{\mathrm{NN}}}$ = 7.7, 11.5, 14.5, 19.6, 27, 39, 54.4, 62.4 and 200 GeV. And the centrality, energy, rapidity, p_{T} and acceptance dependence of correlation function of proton will also be presented. The centrality dependence of efficiency corrected cumulants and cumulant ratios of proton for FXT collisions at $\sqrt{s_{\mathrm{NN}}}$ = 4.5 GeV and the centrality dependence of efficiency uncorrected cumulants and cumulant ratios of proton, anti-proton and net-proton for Cu+Cu collisions at $\sqrt{s_{\mathrm{NN}}}$ = 22.4, 62.4 and 200 GeV will also be present.

4.1 Results for Au+Au collisions

Fig. 4.1 shows the centrality dependence of cumulants (C_1, C_2, C_3 and C_4) of proton, anti-proton and net-proton multiplicity distributions for Au+Au collisions at $\sqrt{s_{\mathrm{NN}}}$ = 7.7, 11.5, 14.5, 19.6, 27, 39, 54.4, 62.4 and 200 GeV. The measurements are made in mid-rapidity ($|\mathrm{y}| < 0.5$) and $0.4 < p_{\mathrm{T}} < 2.0\,(\mathrm{GeV}/c)$. The error bars are statistical errors and the caps represent systematic errors. The C_n for proton, anti-proton and net-proton increase with N_{part} at all the collision energies. At lower energies, the net-proton cumulants has main contributions from protons. The larger values of C_3 and C_4 for most central (0-5%) collisions shows the distributions are non-Gaussian. At higher energies, the proton and anti-proton are almost pair produced. To make the C_4 values at different centralities have similar Y-axis scales, the values of C_4 at $\sqrt{s_{\mathrm{NN}}}$ = 7.7 GeV are divided by 5.

Fig. 4.2 shows the centrality dependence of scaled correlation functions ($\kappa_2/\kappa_1, \kappa_3/\kappa_1$ and κ_4/κ_1) for proton and anti-proton multiplicity distributions for Au+Au collisions at $\sqrt{s_{\mathrm{NN}}}$ = 7.7, 11.5, 14.5, 19.6, 27, 39, 54.4, 62.4 and 200 GeV. The scaled correlation functions are obtained from the measured C_n of proton and anti-proton distributions in the acceptance $|\mathrm{y}| < 0.5$ and $0.4 < p_{\mathrm{T}} < 2.0\,(\mathrm{GeV}/c)$. The error bars are statistical errors and the caps represent systematic errors.

The scaled two-particle correlation functions (κ_2/κ_1) for protons and anti-protons are shown to be negative. The small values of κ_2/κ_1 for anti-protons at lower energies are because of their low production yield. The scaled two-particle correlation functions (κ_2/κ_1) of anti-protons show weak centrality dependence. The scaled two-particle correlation functions (κ_2/κ_1) of protons decrease with collision centrality except for high energy ($\sqrt{s_{\mathrm{NN}}}$ = 200 GeV), and increase with the increasing energy for the most central

4.1.1 Centrality Dependence

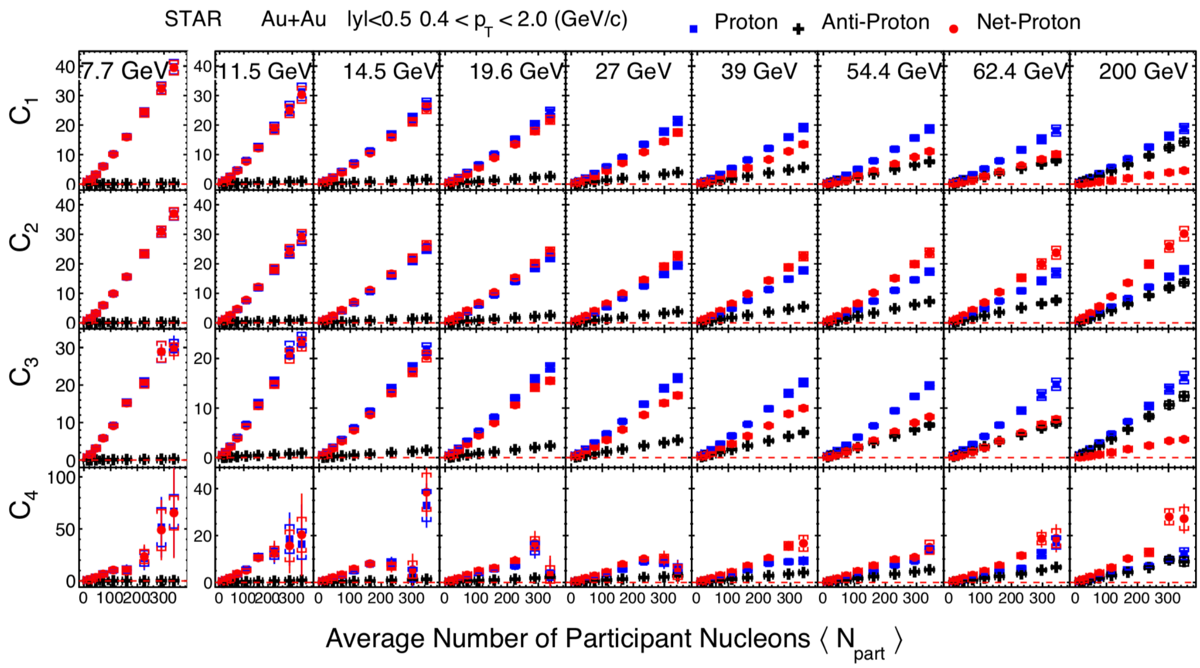

Fig. 4.1: (color online) Centrality dependence of C_1, C_2, C_3 and C_4 of proton, anti-proton and net-proton multiplicity distributions for Au+Au collisions at $\sqrt{s_{\mathrm{NN}}}$ = 7.7, 11.5, 14.5, 19.6, 27, 39, 54.4, 62.4 and 200 GeV. The measurements are made in mid-rapidity (|y| < 0.5) and 0.4 < p_{T} < 2.0 (GeV/c). The error bars are statistical errors and the caps represent systematic errors.

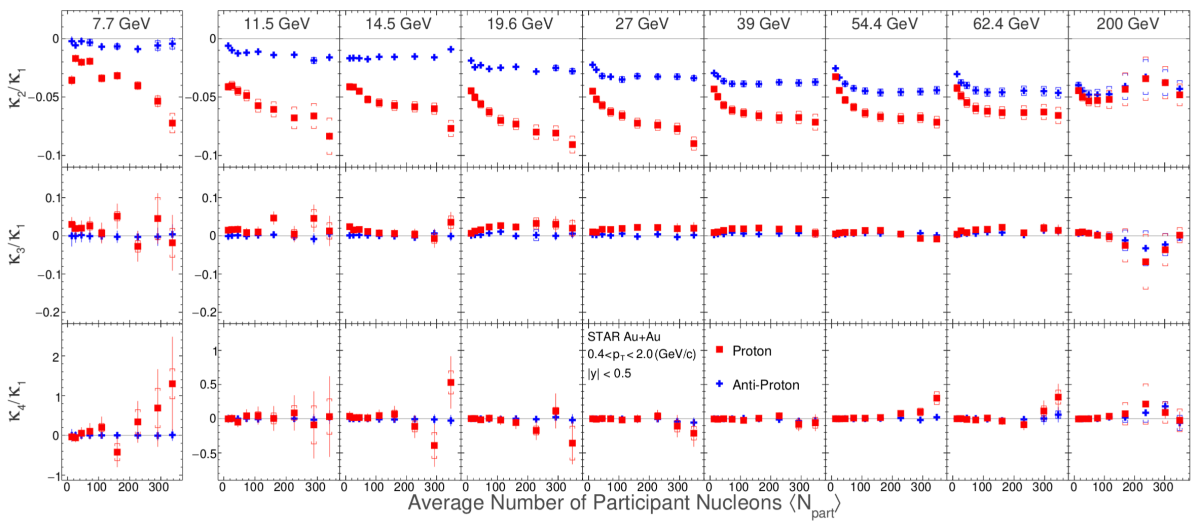

Fig. 4.2: (color online) Centrality dependence of scaled correlation functions ($\kappa_2/\kappa_1, \kappa_3/\kappa_1$ and κ_4/κ_1) for proton and anti-proton multiplicity distributions for Au+Au collisions at $\sqrt{s_{\mathrm{NN}}}$ = 7.7, 11.5, 14.5, 19.6, 27, 39, 54.4, 62.4 and 200 GeV. The correlation function ratios are obtained from the measured C_n of proton and anti-proton distributions in the acceptance |y| < 0.5 and 0.4 < p_{T} < 2.0 (GeV/c). The error bars are statistical errors and the caps represent systematic errors.

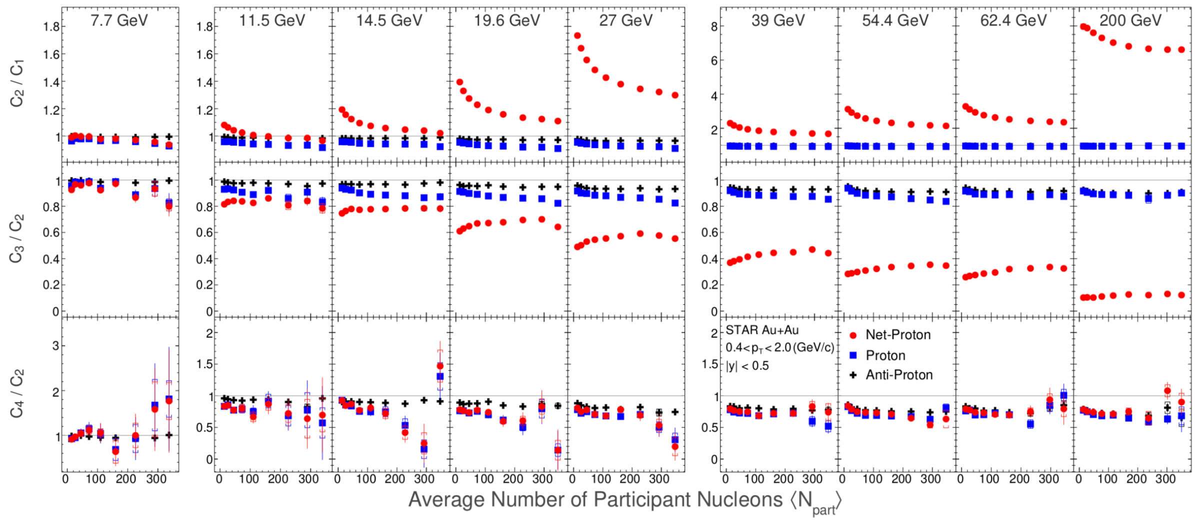

Fig. 4.3: Centrality dependence of cumulant ratios ($C_2/C_1, C_3/C_2$ and C_4/C_2) of proton, anti-proton and net-proton multiplicity distributions for Au+Au collisions at $\sqrt{s_{\rm NN}} = 7.7$, 11.5, 14.5, 19.6, 27, 39, 54.4, 62.4 and 200 GeV. The measurements are made in mid-rapidity (|y| < 0.5) and $0.4 < p_{\rm T} < 2.0\,({\rm GeV}/c)$. The error bars are statistical errors and the caps represent systematic errors.

collision. The κ_2/κ_1 for protons and anti-protons are comparable at $\sqrt{s_{\rm NN}}$ = 200 GeV.

The κ_3/κ_1 for protons and anti-protons are non-significant non-zero values. There is no strong centrality dependence for κ_4/κ_1 observed for all the collision energies.

In order to understand the evolution of centrality dependence of cumulants in Fig. 4.1, we invoke the central limit theoremand consider the distribution at any given centrality i to be a superposition of several independent source distributions[92] . Assuming the average number of the sources for a given centrality are equal up to some number of times the corresponding $\langle N_{part}\rangle$, the cumulants (C_n) should be linearly dependent on $\langle N_{part}\rangle$ and the cumulant ratios ($C_2/C_1, C_3/C_2$ and C_4/C_2) should be constant as a function of $\langle N_{part}\rangle$. Fig. 4.3 shows the centrality dependence of cumulant ratios ($C_2/C_1, C_3/C_2$ and C_4/C_2) of proton, anti-proton and net-proton multiplicity distributions for Au+Au collisions at $\sqrt{s_{\rm NN}} = 7.7$, 11.5, 14.5, 19.6, 27, 39, 54.4, 62.4 and 200 GeV. For higher energies (above 19.6 GeV), the values of C_2/C_1 show a smooth decrease with increasing centrality and for lower energies the dependence is small. The C_3/C_2 values show weak centrality dependence and they are positive below unity for all the collision energies. The C_3/C_2 values of net-proton decrease with the increasing energies for all the centralities. For proton and net-proton, the C_4/C_2 values decrease with increasing centralities except the significant increase at $\sqrt{s_{\rm NN}}$ = 7.7 GeV. Having presented the efficiency corrected results for cumulants and cumulant ratios, we will focus on discussing the energy, rapidity, $p_{\rm T}$ and the acceptance dependence for most central $(0-5\%)$ Au+Au collisions.

4.1.2 Rapidity Dependence

Fig. 4.4 shows the rapidity dependence of cumulants (C_1, C_2, C_3 and C_4) of proton, anti-proton and net-proton multiplicity distributions for most central $(0-5\%)$ Au+Au collisions at $\sqrt{s_{\rm NN}} = 7.7$, 11.5, 14.5, 19.6, 27, 39, 54.4, 62.4 and 200 GeV. The X-axis rapidity cut y_{max} is applied as $|y| < y_{max}$ $(-y_{max} < y < y_{max}, \Delta y = 2y_{max})$. The measure-

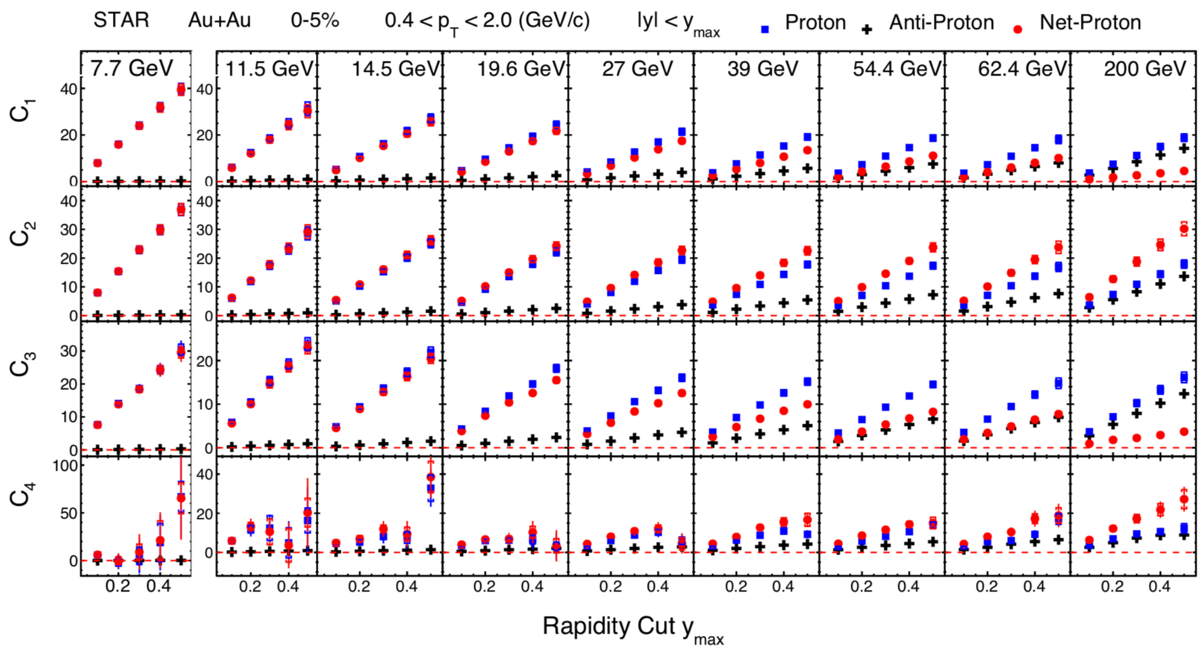

Fig. 4.4: Rapidity dependence of cumulants (C_1, C_2, C_3 and C_4) of proton, anti-proton and net-proton multiplicity distributions for Au+Au collisions at $\sqrt{s_{\rm NN}}$ = 7.7, 11.5, 14.5, 19.6, 27, 39, 54.4, 62.4 and 200 GeV. The error bars are statistical errors and the caps represent systematic errors.

ments are made in the $p_{\rm T}$ range between 0.4 and 2.0 GeV/c ($0.4 < p_{\rm T} < 2.0\,({\rm GeV}/c)$). The C_n values for proton, anti-proton and net-proton increase with the increasing rapidity window. The C_n values for proton and net-proton have similar values at $\sqrt{s_{\rm NN}} < 27$ GeV.

Fig. 4.5 shows the rapidity dependence of scaled correlation functions ($\kappa_2/\kappa_1, \kappa_3/\kappa_1$ and κ_4/κ_1) of proton and anti-proton multiplicity distributions for most central ($0-5\%$) Au+Au collisions at $\sqrt{s_{\rm NN}}$ = 7.7, 11.5, 14.5, 19.6, 27, 39, 54.4, 62.4 and 200 GeV. The κ_2/κ_1 values for protons monotonically decrease as the increasing rapidity acceptance window for all energies. For anti-proton, the κ_2/κ_1 values decrease with the increasing rapidity window except for the low energies ($\sqrt{s_{\rm NN}} < 19.6$ GeV). For anti-proton, the κ_2/κ_1 values show larger deviation from zero at higher energies and larger rapidity window. For proton, the κ_3/κ_1 values start to become negative at $\sqrt{s_{\rm NN}} = 7.7$ GeV when the rapidity window is beyond $y_{max} = 0.2$. The κ_4/κ_1 values for proton show a monotonically increasing behavior for most central ($0-5\%$) Au+Au collisions at larger rapidity window (|y|>0.2) at $\sqrt{s_{\rm NN}} = 7.7$ GeV, however, the κ_4/κ_1 values for proton are almost independence on Δy for other energies except for $\sqrt{s_{\rm NN}} = 54.4$ GeV.

Fig. 4.6 shows the rapidity dependence of cumulant ratios ($C_2/C_1, C_3/C_2$ and C_4/C_2) of proton, anti-proton and net-proton multiplicity distributions for most central ($0-5\%$) Au+Au collisions at $\sqrt{s_{\rm NN}}$ = 7.7, 11.5, 14.5, 19.6, 27, 39, 54.4, 62.4 and 200 GeV. The C_2/C_1 values for net-proton show a monotonic energy dependence, and the C_2/C_1 values show the decrease with the increasing rapidity acceptance at $\sqrt{s_{\rm NN}} < 39$ GeV. The C_3/C_2 values show an energy dependence (decrease with increasing energy) and decrease with increasing Δy except for high energies. The C_3/C_2 values for protons and anti-protons are similar at $\sqrt{s_{\rm NN}}$ =62.4 and 200 GeV. At $\sqrt{s_{\rm NN}}$ = 7.7 and 11.5 GeV, the C_3/C_2 values of proton and net-proton are similar. The C_4/C_2 values for proton, anti-proton and net-

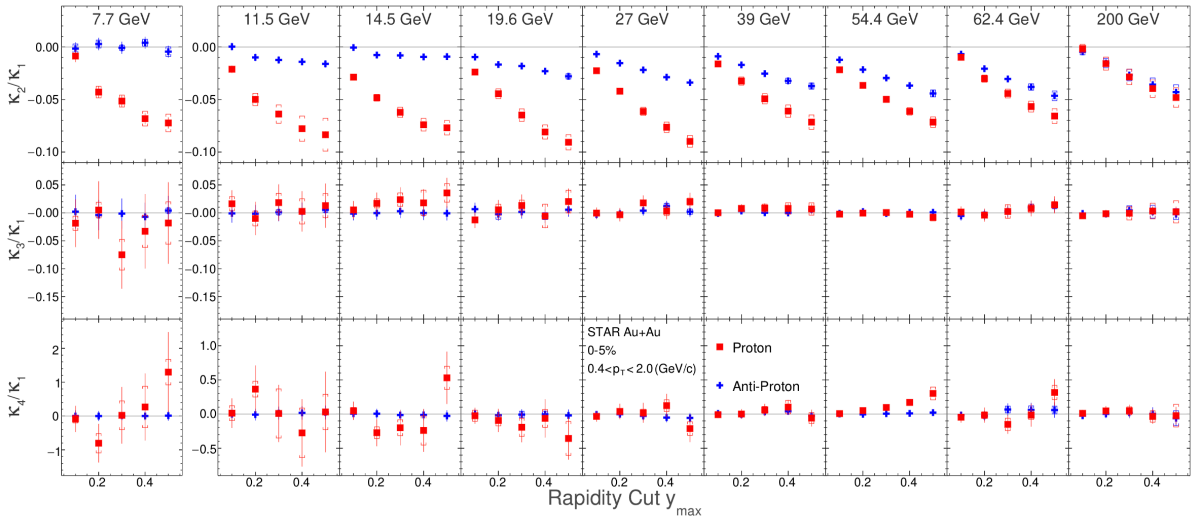

Fig. 4.5: Rapidity dependence of scaled correlation functions ($\kappa_2/\kappa_1, \kappa_3/\kappa_1$ and κ_4/κ_1) of proton and anti-proton multiplicity distributions for most central $(0-5\%)$ Au+Au collisions at $\sqrt{s_{\rm NN}}$ = 7.7, 11.5, 14.5, 19.6, 27, 39, 54.4, 62.4 and 200 GeV. The X-axis rapidity cut y_{max} is applied as $|y| < y_{max}$. The error bars are statistical errors and the caps represent systematic errors.

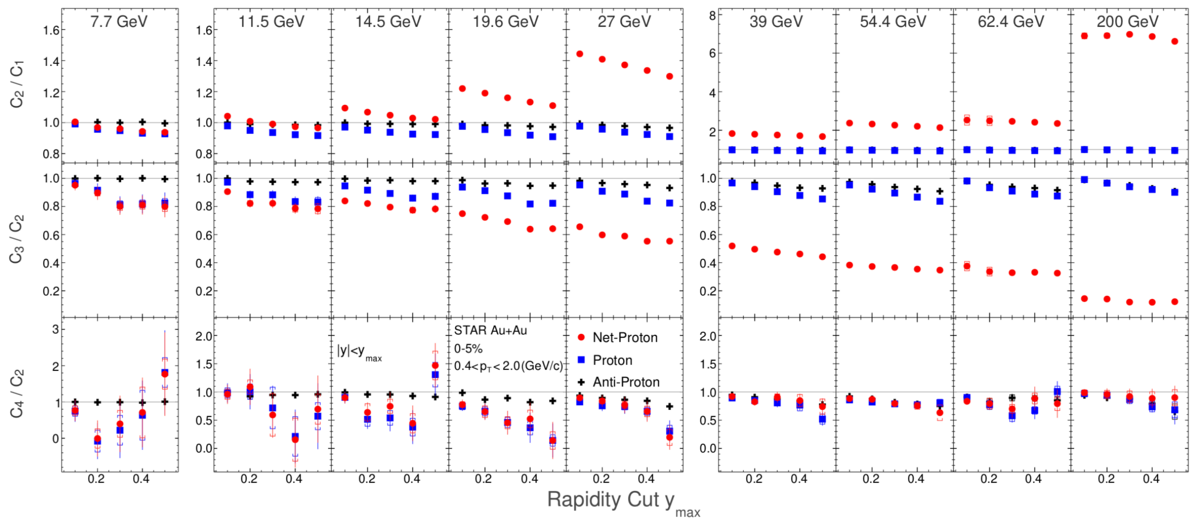

Fig. 4.6: Rapidity dependence of cumulant ratios ($C_2/C_1, C_3/C_2$ and C_4/C_2) of proton, anti-proton and net-proton multiplicity distributions for most central $(0-5\%)$ Au+Au collisions at $\sqrt{s_{\rm NN}}$ = 7.7, 11.5, 14.5, 19.6, 27, 39, 54.4, 62.4 and 200 GeV. The measurements are done for $0.4 < p_{\rm T} < 2.0\,({\rm GeV}/c)$. The error bars are statistical errors and the caps represent systematic errors.

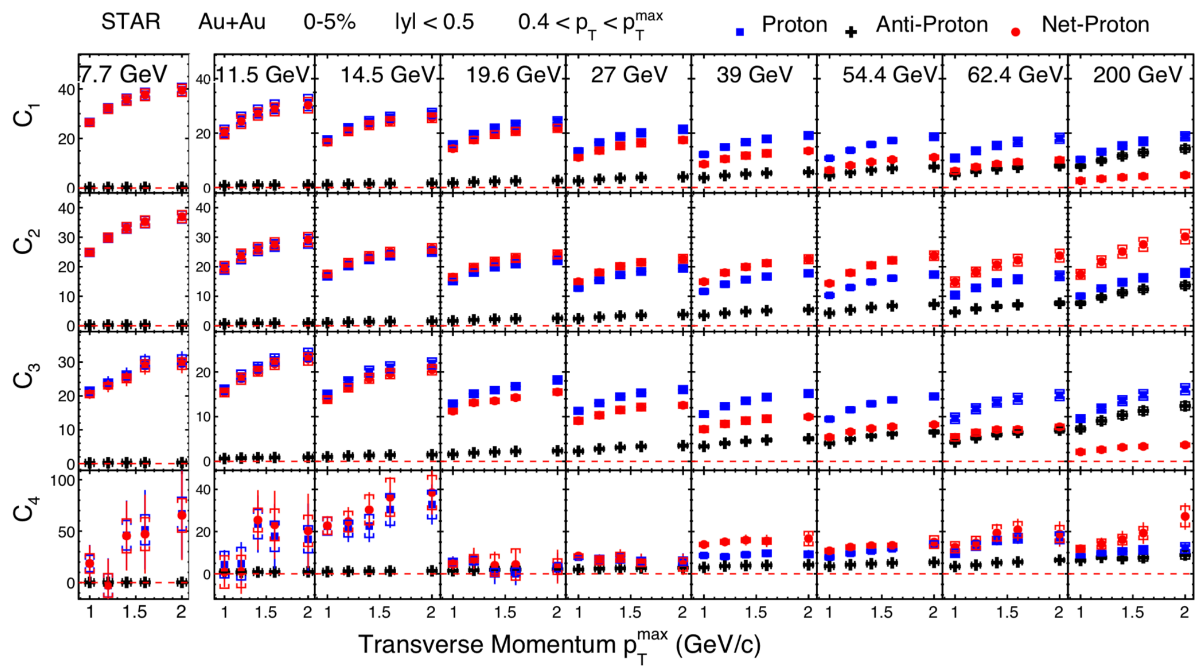

Fig. 4.7: Transverse momentum dependence of cumulants (C_1, C_2, C_3 and C_4) of proton, anti-proton and net-proton multiplicity distributions for most central (0 − 5%) Au+Au collisions at $\sqrt{s_{\mathrm{NN}}}$ = 7.7, 11.5, 14.5, 19.6, 27, 39, 54.4, 62.4 and 200 GeV. The measurements are made in mid-rapidity (|y| < 0.5). The error bars are statistical errors and the caps represent systematic errors.

proton are similar and independent of rapidity window for $\sqrt{s_{\mathrm{NN}}}$ > 39 GeV. The values are close to unity, deviations from unity start to appear for proton and anti-proton at $\sqrt{s_{\mathrm{NN}}}$ = 27 GeV and decrease with the increasing Δy. The C_4/C_2 values for proton and net-proton increase with the increasing Δy at at $\sqrt{s_{\mathrm{NN}}}$ = 7.7 GeV. In Ref. [93], it has been proposed to look at the rapidity dependence of cumulants (C_1, C_2, C_3 and C_4) to understand the character of the system formed in the high energy heavy-ion collisions.

4.1.3 Transverse Momentum (p_T) Dependence

Fig. 4.7 shows the p_{T} dependence of cumulants (C_1, C_2, C_3 and C_4) of proton, anti-proton and net-proton multiplicity distributions for most central (0 − 5%) Au+Au collisions at $\sqrt{s_{\mathrm{NN}}}$ = 7.7, 11.5, 14.5, 19.6, 27, 39, 54.4, 62.4 and 200 GeV. The error bars are statistical errors and the caps represent systematic errors. At higher energies, all of the C_n values of proton, anti-proton and net-proton, except C_4, increase with increasing p_{T} acceptance. The C_4 values are independent of p_{T} . At lower energies, the C_n values of proton and net-proton increase with p_{T} acceptance, however the C_n values of anti-protons remains constant due to their low production.

Fig. 4.8 shows the p_{T} dependence of scaled correlation functions ($\kappa_2/\kappa_1, \kappa_3/\kappa_1$ and κ_4/κ_1) of proton and anti-proton multiplicity distributions for Au+Au collisions at $\sqrt{s_{\mathrm{NN}}}$ = 7.7, 11.5, 14.5, 19.6, 27, 39, 54.4, 62.4 and 200 GeV. The κ_2/κ_1 values for protons and anti-protons are negative and monotonically decrease with increasing p_{T} acceptance at high energies. At lower energies ($\sqrt{s_{\mathrm{NN}}}$ < 19.6 GeV) no such decrease is observed for protons and anti-protons. No significant three-particle correlations are observed as a function as p_{T} for protons and anti-protons for $\sqrt{s_{\mathrm{NN}}}$ > 11.5 GeV. The κ_4/κ_1 values

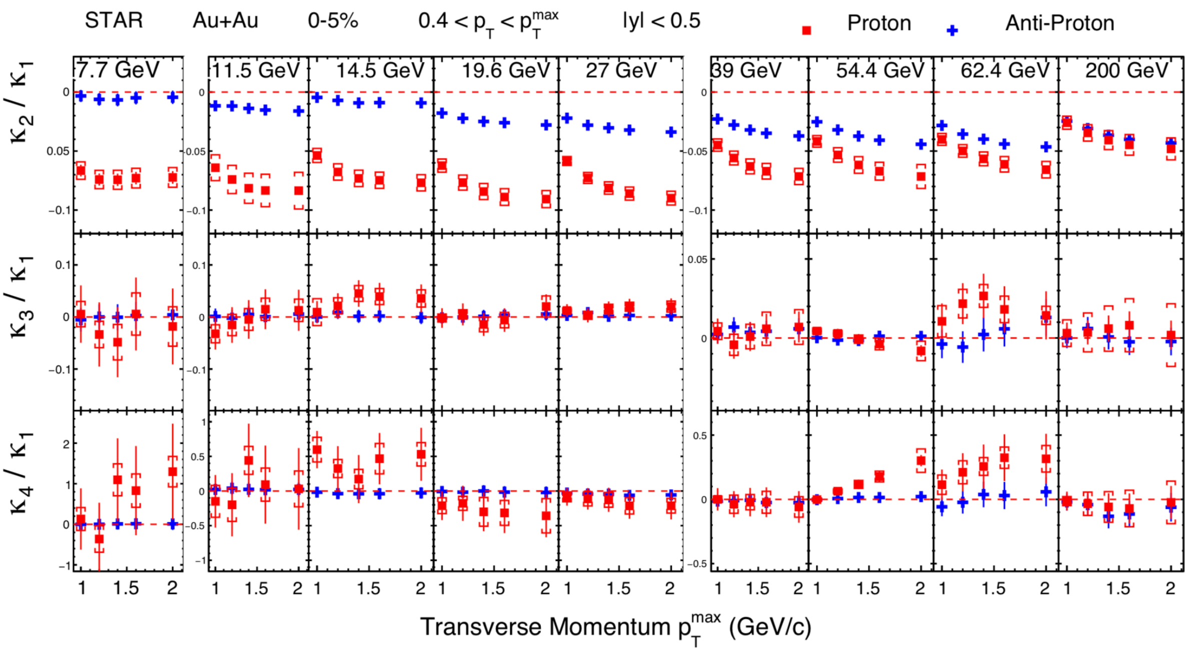

Fig. 4.8: Transverse momentum dependence of scaled correlation functions ($\kappa_2/\kappa_1, \kappa_3/\kappa_1$ and κ_4/κ_1) of proton and anti-proton multiplicity distributions for most central $(0-5\%)$ Au+Au collisions at $\sqrt{s_{\mathrm{NN}}}$ = 7.7, 11.5, 14.5, 19.6, 27, 39, 54.4, 62.4 and 200 GeV. The error bars are statistical errors and the caps represent systematic errors.

for anti-protons are almost zero for all collision energies, and for protons the $\kappa_4\kappa_1$ values increase with the p_{T} acceptance at $\sqrt{s_{\mathrm{NN}}}$ = 54.4 and 62.4 GeV.

Fig. 4.9 shows the p_{T} dependence of cumulant ratios ($C_2/C_1, C_3/C_2$ and C_4/C_2) of proton, anti-proton and net-proton multiplicity distributions for most central $(0-5\%)$ Au+Au collisions at $\sqrt{s_{\mathrm{NN}}}$ = 7.7, 11.5, 14.5, 19.6, 27, 39, 54.4, 62.4 and 200 GeV. It was found that most of the ratios are weak independent on p_{T} acceptance dependence for all the energies. The C_2/C_1 values of protons, anti-protons and net-protons are similar for $\sqrt{s_{\mathrm{NN}}}$ < 27 GeV. The C_3/C_2 values for protons and anti-protons are similar at higher energies, but differ from each other at lower energies. At $\sqrt{s_{\mathrm{NN}}}$ = 7.7 GeV, the C_4/C_2 ratios for protons and net-protons increase with the increasing p_{T} acceptance.

4.1.4 Acceptance Dependence

Fig. 4.10 shows the acceptance dependence (average number of proton, anti-proton and sum of proton and anti-proton) of cumulants (C_1, C_2, C_3 and C_4) of proton, anti-proton and net-proton multiplicity distributions for most central $(0-5\%)$ Au+Au collisions at $\sqrt{s_{\mathrm{NN}}}$ = 7.7, 11.5, 14.5, 19.6, 27, 39, 54.4, 62.4 and 200 GeV. Δy represents the rapidity acceptance, and varied within 0.1 unit (Δy = 0.2, 0.4, 0.6, 0.8 and 1). Δp_T represents the p_T acceptance and varied within 0.4 to 2 GeV/c ($0.4 < p_T < 1.0, 1.2, 1.4, 1.6$ and 2.0 GeV/c). When changing the rapidity and p_T acceptance, the number of protons and anti-protons are varied. The C_1, C_2 and C_3 of proton, anti-proton and net-proton show a linear increase with the number of proton, anti-proton and the sum of them in the acceptance. For C_4 the variations with multiplicity acceptance are small except at $\sqrt{s_{\mathrm{NN}}}$ = 7.7 GeV. It's observed that C_4 values of protons and net-protons increase rapidly with the multiplicity acceptance.

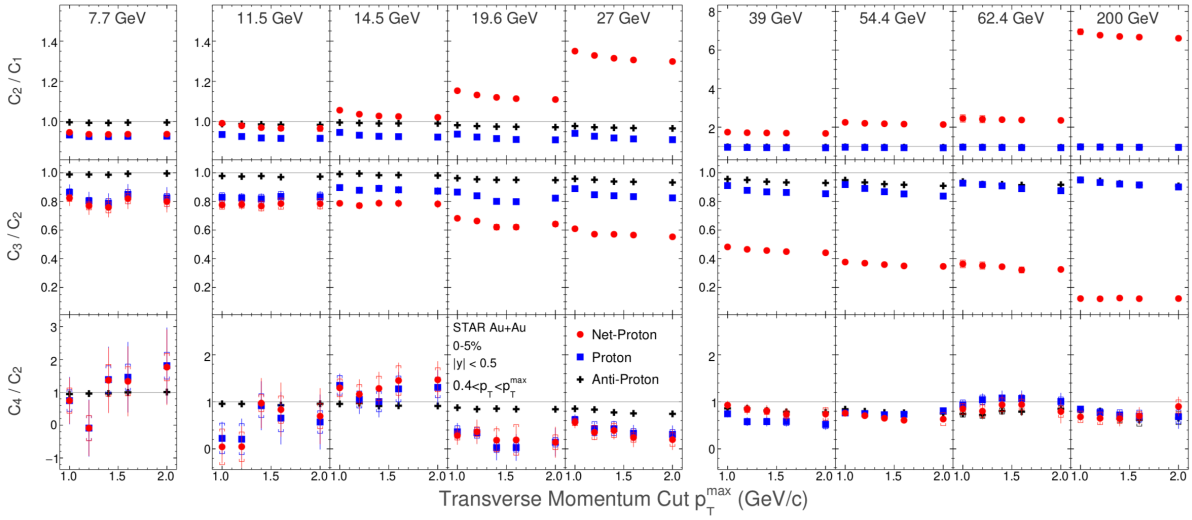

Fig. 4.9: Transverse momentum dependence of cumulant ratios ($C_2/C_1, C_3/C_2$ and C_4/C_2) of proton, anti-proton and net-proton multiplicity distributions for most central $(0-5\%)$ Au+Au collisions at $\sqrt{s_{\mathrm{NN}}}$ = 7.7, 11.5, 14.5, 19.6, 27, 39, 54.4, 62.4 and 200 GeV. The error bars are statistical errors and the caps represent systematic errors.

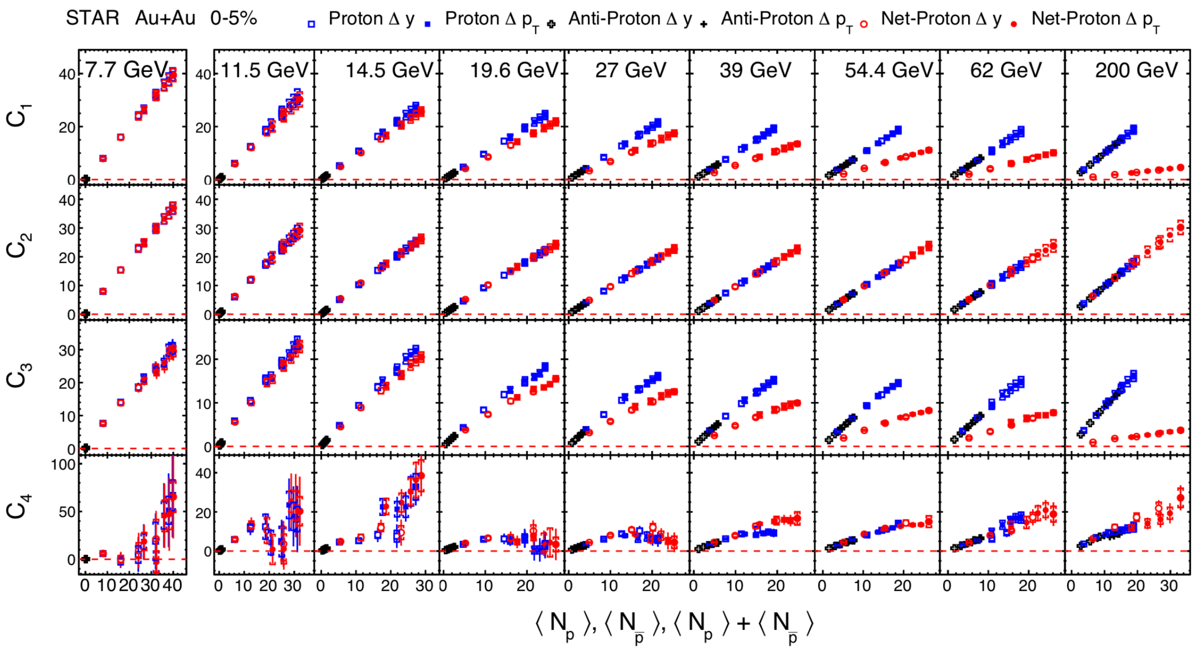

Fig. 4.10: Acceptance dependence (average number of proton, anti-proton and sum of proton and anti-proton) of cumulants (C_1, C_2, C_3 and C_4) of proton, anti-proton and net-proton multiplicity distributions for most central $(0-5\%)$ Au+Au collisions at $\sqrt{s_{\mathrm{NN}}} =$ 7.7, 11.5, 14.5, 19.6, 27, 39, 54.4, 62.4 and 200 GeV. The error bars are statistical errors and the caps represent systematic errors.

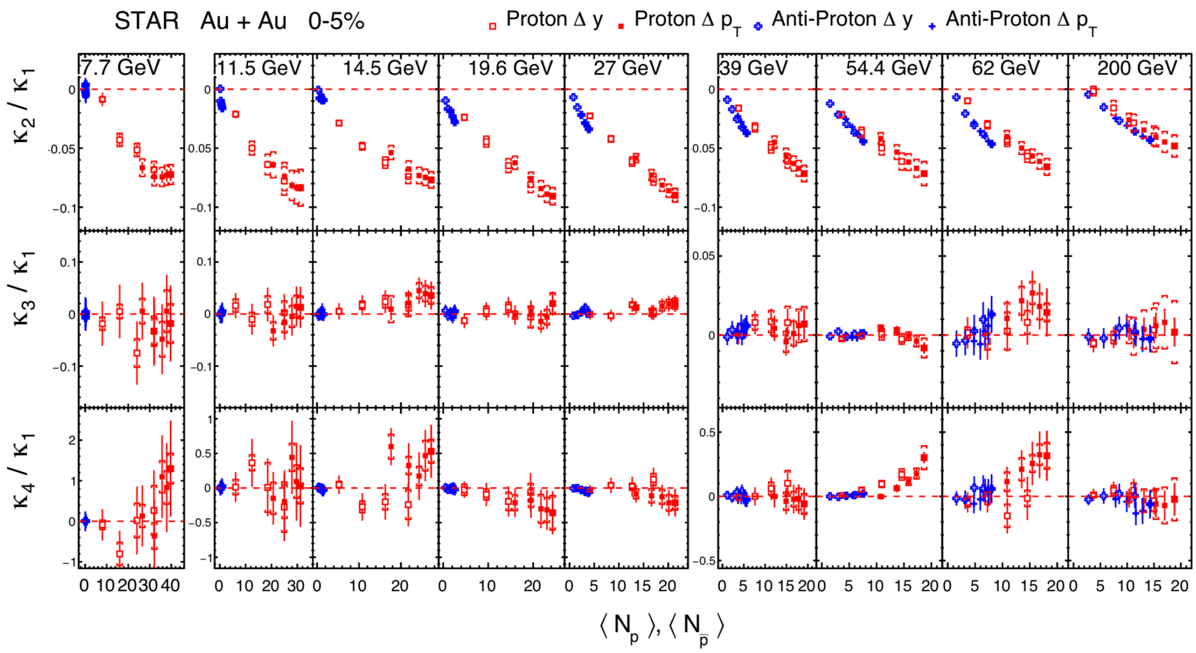

Fig. 4.11: Acceptance dependence (average number of proton and anti-proton) of scaled correlation functions ($\kappa_2/\kappa_1, \kappa_3/\kappa_1$ and κ_4/κ_1) of proton and anti-proton multiplicity distributions for most central $(0-5\%)$ Au+Au collisions at $\sqrt{s_{\rm NN}}$ = 7.7, 11.5, 14.5, 19.6, 27, 39, 54.4, 62.4 and 200 GeV. The error bars are statistical errors and the caps represent systematic errors.

Fig. 4.11 shows acceptance dependence (average number of proton and anti-proton) of scaled correlation functions ($\kappa_2/\kappa_1, \kappa_3/\kappa_1$ and κ_4/κ_1) of proton and anti-proton multiplicity distributions for most central $(0-5\%)$ Au+Au collisions at $\sqrt{s_{\rm NN}}$ = 7.7, 11.5, 14.5, 19.6, 27, 39, 54.4, 62.4 and 200 GeV. The conclusions are similar to as seen for the variation of κ_n/κ_1 with centrality and rapidity acceptance. A strong particle multiplicity dependence of κ_n/κ_1 is observed for proton at $\sqrt{s_{\rm NN}}$ = 7.7 GeV. From the above different studies that scaled correlation functions for proton and anti-proton extracted from the corresponding cumulant measurements, we found that the two-particle correlations of protons are negative for most central $(0-5\%)$ Au+Au collisions at all collision energies, the three-particle correlation for protons are positive and the four-particle for protons have a larger enhancement at $\sqrt{s_{\rm NN}}$ = 7.7 GeV.

Fig. 4.12 shows the acceptance dependence (average number of proton, anti-proton and sum of proton and anti-proton) of cumulant ratios ($C_2/C_1, C_3/C_2$ and C_4/C_2) of proton, anti-proton and net-proton multiplicity distributions for most central $(0-5\%)$ Au+Au collisions at $\sqrt{s_{\rm NN}}$ = 7.7, 11.5, 14.5, 19.6, 27, 39, 54.4, 62.4 and 200 GeV. The C_2/C_1 values are almost independent of multiplicity acceptance. The C_3/C_2 values of net-protons decreases with increase in multiplicity acceptance. The net-proton and proton C_4/C_2 values show weak dependence on multiplicity acceptance except $\sqrt{s_{\rm NN}}$ = 7.7 GeV. A strong increase of net-proton and proton C_4/C_2 ratios are observed when increasing the total number of protons and anti-protons at $\sqrt{s_{\rm NN}}$ = 7.7 GeV.

As discussed in [62, 78, 94, 95], the cumulants (C_n) and correlation functions (κ_n) are expected to grow with increasing in Δy and $p_{\rm T}$ acceptance and then saturate in the limit of full acceptance. When the rapidity acceptance (Δy) is much smaller than the typical correlation length (ξ) of the system ($\Delta y \ll \xi$), the C_n and κ_n should scale with some power

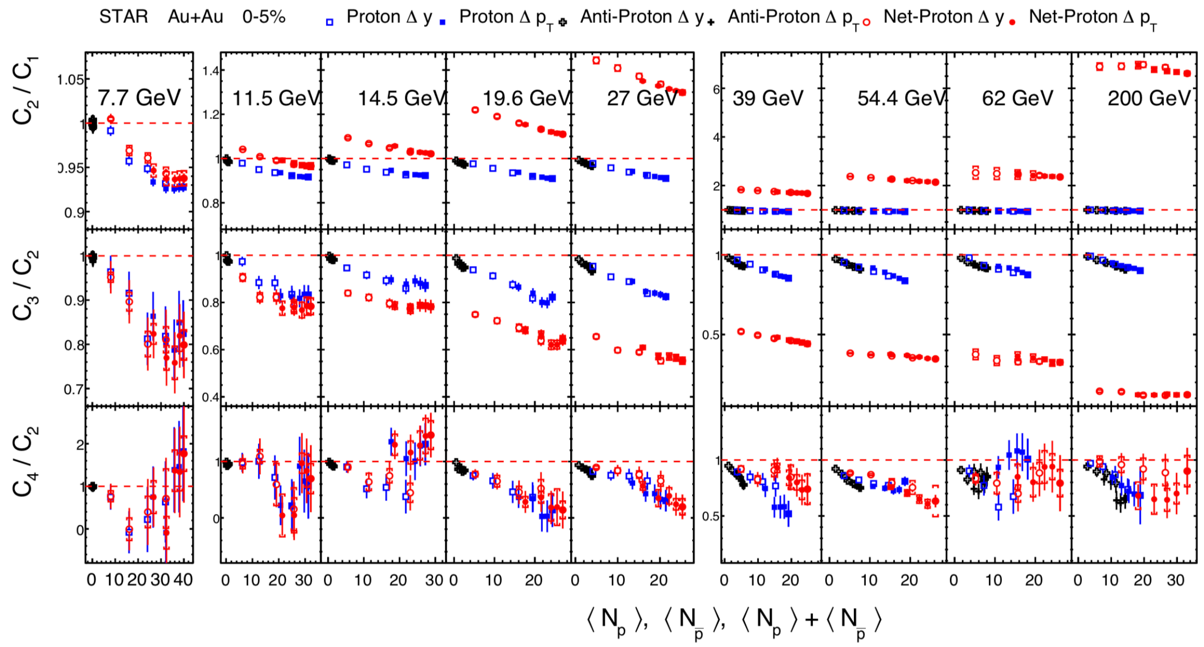

Fig. 4.12: Acceptance dependence (average number of proton, anti-proton and sum of proton and anti-proton) of cumulant ratios ($C_2/C_1, C_3/C_2$ and C_4/C_2) of proton, anti-proton and net-proton multiplicity distributions for most central ($0-5\%$) Au+Au collisions at $\sqrt{s_{\mathrm{NN}}} = 7.7$, 11.5, 14.5, 19.6, 27, 39, 54.4, 62.4 and 200 GeV.

of number of accepted mean particle multiplicities and Δy as C_n, $\kappa_n \propto (\Delta N)^n \propto (\Delta y)^n$. While in the regime where the rapidity acceptance becomes much larger than ξ ($\Delta y \ll \xi$), the C_n, κ_n scale linearly with Δy or mean multiplicity in the acceptance, and cumulant ratios are expected to be acceptance independent. On the other hand, the effect of baryon number conservation plays an important role on proton cumulants and correlation functions in heavy-ion collisions, especially at low energies. It is the main reason for the negative two-particle correlation functions of proton and anti-proton[39, 40]. Dependence of the cumulants and correlation functions on Δy, p and mean proton and anti-proton multiplicities provide data to understand various effects in more detail.

4.1.5 Energy Dependence

Fig. 4.13 shows the variation of $\chi_2^B/\chi_1^B, \chi_3^B/\chi_2^B$ and χ_4^B/χ_2^B as a function of $\sqrt{s_{\mathrm{NN}}}$ from a hadron resonance gas model. The results are shown for different p_T acceptances. The differences due to acceptance are very small, the maximum effect of which is at the level of 5% for $\sqrt{s_{\mathrm{NN}}} = 7.7$ GeV for χ_4^B/χ_2^B. The HRG results also show that the net-proton results with resonance decays are smaller compared to net-baryons and larger than net-protons without the decay effect. Here also the effect is at the level of 5% for the lowest $\sqrt{s_{\mathrm{NN}}}$ and smaller at higher energies in case of χ_4^B/χ_2^B. The corresponding effect on χ_3^B/χ_2^B and χ_2^B/χ_1^B is larger at the higher energies and of the order of 17% for net-proton without resonance decay and net-baryon, while the effect is 10% for net-proton with resonance decays and net-baryons[87].

Fig. 4.14 left shows energy dependence of net-baryon $C_2/C_1, C_3/C_2$ and C_4/C_2 for various p_{T} acceptance from UrQMD model. It was observed that the larger p_{T} acceptance is, the smaller values of cumulant ratios are. Further, with the same p_{T} acceptance, the

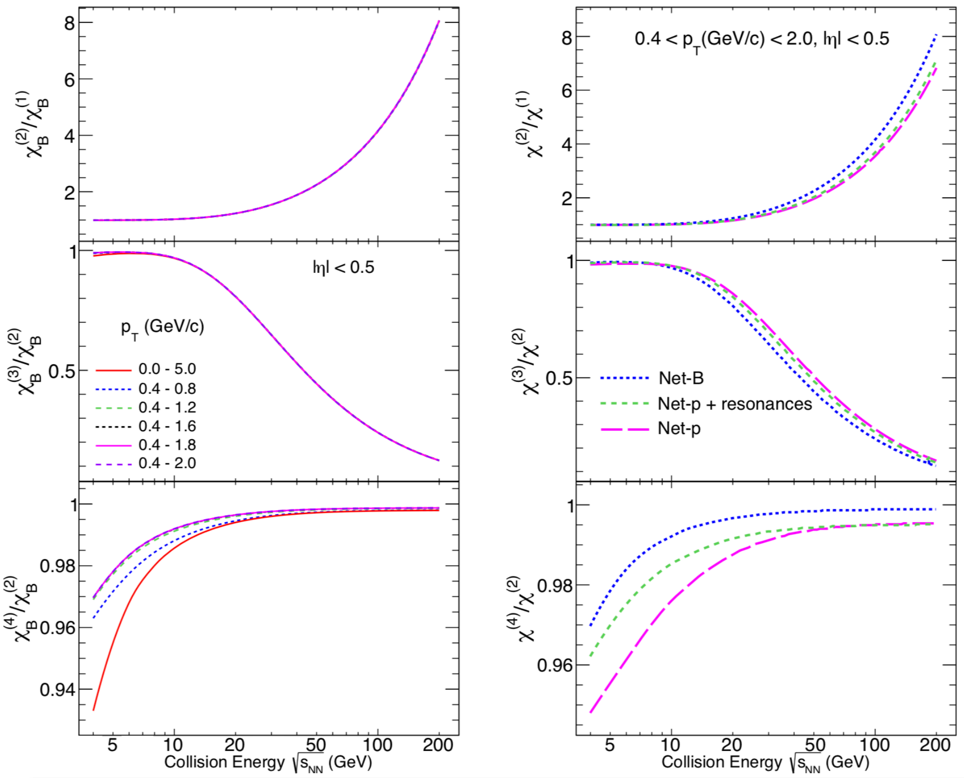

Fig. 4.13: (color line) (left) p_T dependence of $\chi_2^B/\chi_1^B, \chi_3^B/\chi_2^B$ and χ_4^B/χ_2^B with $\sqrt{s_{\mathrm{NN}}}$ from hadron resonance gas model. (right) The energy dependence of $\chi_2^X/\chi_1^X, \chi_3^X/\chi_2^X$ and χ_4^X/χ_2^X within the experimental acceptance. Where X is the net-baryon, net-proton without resonance decay and net-proton with resonance decay[87].

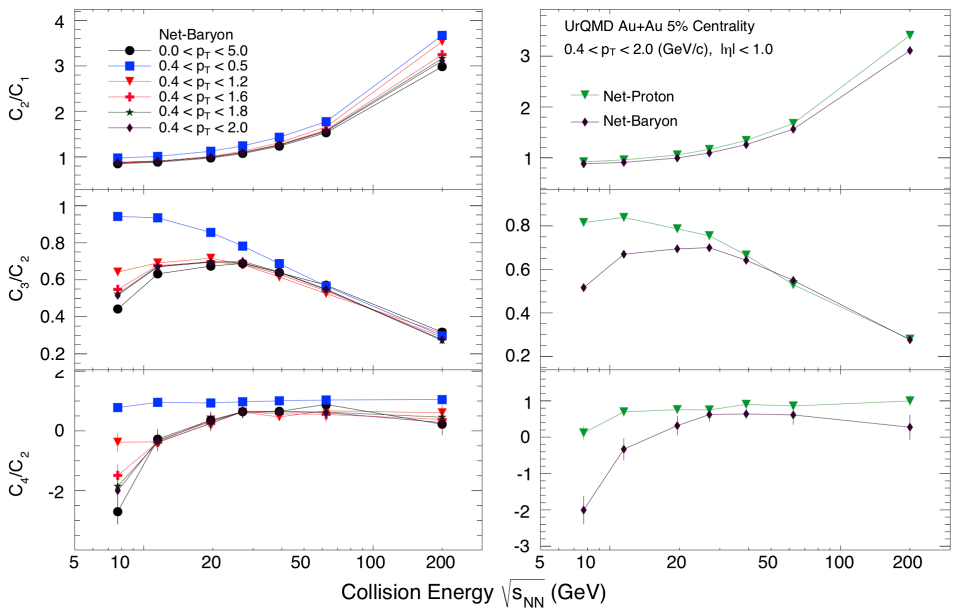

Fig. 4.14: (color line) (left) Energy dependence of $C_2/C_1, C_3/C_2$ and C_4/C_2 of net-baryon from different p_{T} acceptance from UrQMD model[90, 91]. (right) Energy dependence of $C_2/C_1, C_3/C_2$ and C_4/C_2 of net-proton and net-baryon from UrQMD model within experimental acceptance.

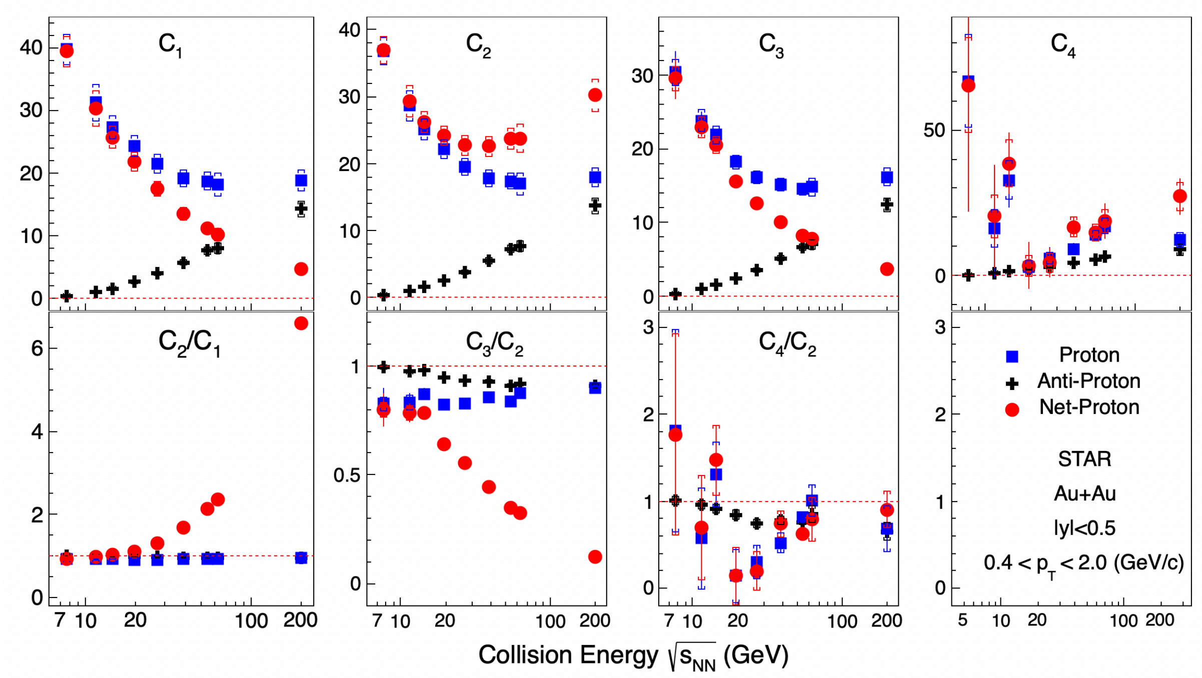

Fig. 4.15: Collision energy dependence of cumulants and cumulant ratios ($C_1, C_2, C_3, C_4, C_2/C_1, C_3/C_2$ and C_4/C_2) of proton, anti-proton and net-proton multiplicity distributions for most central $(0-5\%)$ Au+Au collisions at $\sqrt{s_{\mathrm{NN}}}$ = 7.7, 11.5, 14.5, 19.6, 27, 39, 54.4, 62.4 and 200 GeV from STAR experiment. The measurements are done for |y|< 0.5 and $0.4 < p_{\mathrm{T}} < 2.0\,(\mathrm{GeV}/c)$. The error bars are statistical errors and the caps represent systematic errors.

values of net-baryon C_4/C_2 and C_2/C_1 ratios decrease with decreasing energies. Fig. 4.14 right also shows the comparison of the cumulant ratios for net-baryon and net-proton within the experimental acceptance for various energies. It can be found that the differences between results from different acceptance are larger for UrQMD compared to HRG model. In UrQMD the difference be- tween net-baryon and net-protons are larger at the lower beam energies for a fixed p_{T} and y acceptance. The negative C_4/C_2 values of net-baryons observed at low energies are mainly due to the effect of baryon number conservation.

Fig. 4.15 shows the collision energy dependence of cumulants and cumulant ratios ($C_1, C_2, C_3, C_4, C_2/C_1, C_3/C_2$ and C_4/C_2) of proton, anti-proton and net-proton multiplicity distributions for most central $(0-5\%)$ Au+Au collisions at $\sqrt{s_{\mathrm{NN}}}$ = 7.7, 11.5, 14.5, 19.6, 27, 39, 54.4, 62.4 and 200 GeV. The C_n for anti-proton increase with energies. The C_1 and C_3 values for proton and net-proton decrease with energies, while the C_2 and C_4 for net-proton show a non-monotonic dependence on energies . The C_n values for net-proton and proton are similar for $\sqrt{s_{\mathrm{NN}}}$ < 19.6 GeV. Also shown in Fig. 4.15 are the ratios $C_2/C_1, C_3/C_2$ and C_4/C_2 for proton, anti-proton and net-proton as a function of energies. for most central $(0-5\%)$ Au+Au collisions. The C_2/C_1 values for proton and anti-proton are close to unity, however for net-proton the values increase with energies. The C_3/C_2 values for anti-proton smoothly approach unity with decreasing in energies. While those for proton start to deviate from anti-proton for $\sqrt{s_{\mathrm{NN}}}$ < 54.4 GeV. The net-proton C_3/C_2 shows a non-monotonic variation with energies. The C_4/C_2 values for anti-proton are close to unity. While those for proton and net-proton closely follow the

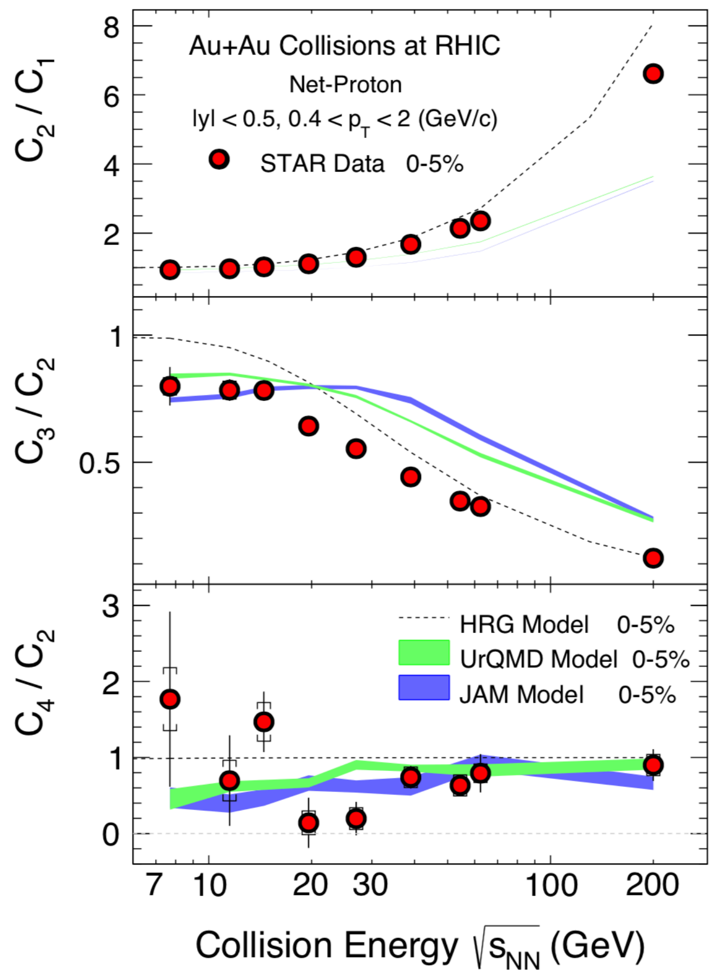

Fig. 4.16: Collision energy dependence of cumulant ratios ($C_2/C_1, C_3/C_2$ and C_4/C_2) of net-proton multiplicity distributions for most central ($0-5\%$) Au+Au collisions at $\sqrt{s_{\mathrm{NN}}}$ = 7.7, 11.5, 14.5, 19.6, 27, 39, 54.4, 62.4 and 200 GeV. The results are compared to corresponding values from UrQMD and HRG models within the experimental acceptances. The bars on the data point are statistical errors and the caps represent systematic errors. The widths of the bands reflect the statistical uncertainties with the model calculations.

non-monotonic variation with $\sqrt{s_{\mathrm{NN}}}$.

Fig. 4.16 shows the comparison between experimental measurements of $C_2/C_1, C_3/C_2$ and C_4/C_2 of net-proton distributions for most central ($0-5\%$) Au+Au collisions as a function of $\sqrt{s_{\mathrm{NN}}}$ with the corresponding results from HRG and UrQMD models. We observe both the models, which do not have phase transition effects, show monotonic variations of the cumulant ratios with beam energy. However the experimental measurements of C_3/C_2 and C_4/C_2 ratios show a non-monotonic variation with $\sqrt{s_{\mathrm{NN}}}$. The C_2/C_1 ratios in both model and data show a smooth increase with $\sqrt{s_{\mathrm{NN}}}$. It may be noted that higher-order cumulants are more sensitive to the correlation length of the system.

Based on Eq. 1.67, the cumulants can be expressed into the sum of various order multi-particle correlation functions. In order to understand the contributions to the (anti-)proton cumulants from different physics effects, one can present different orders of

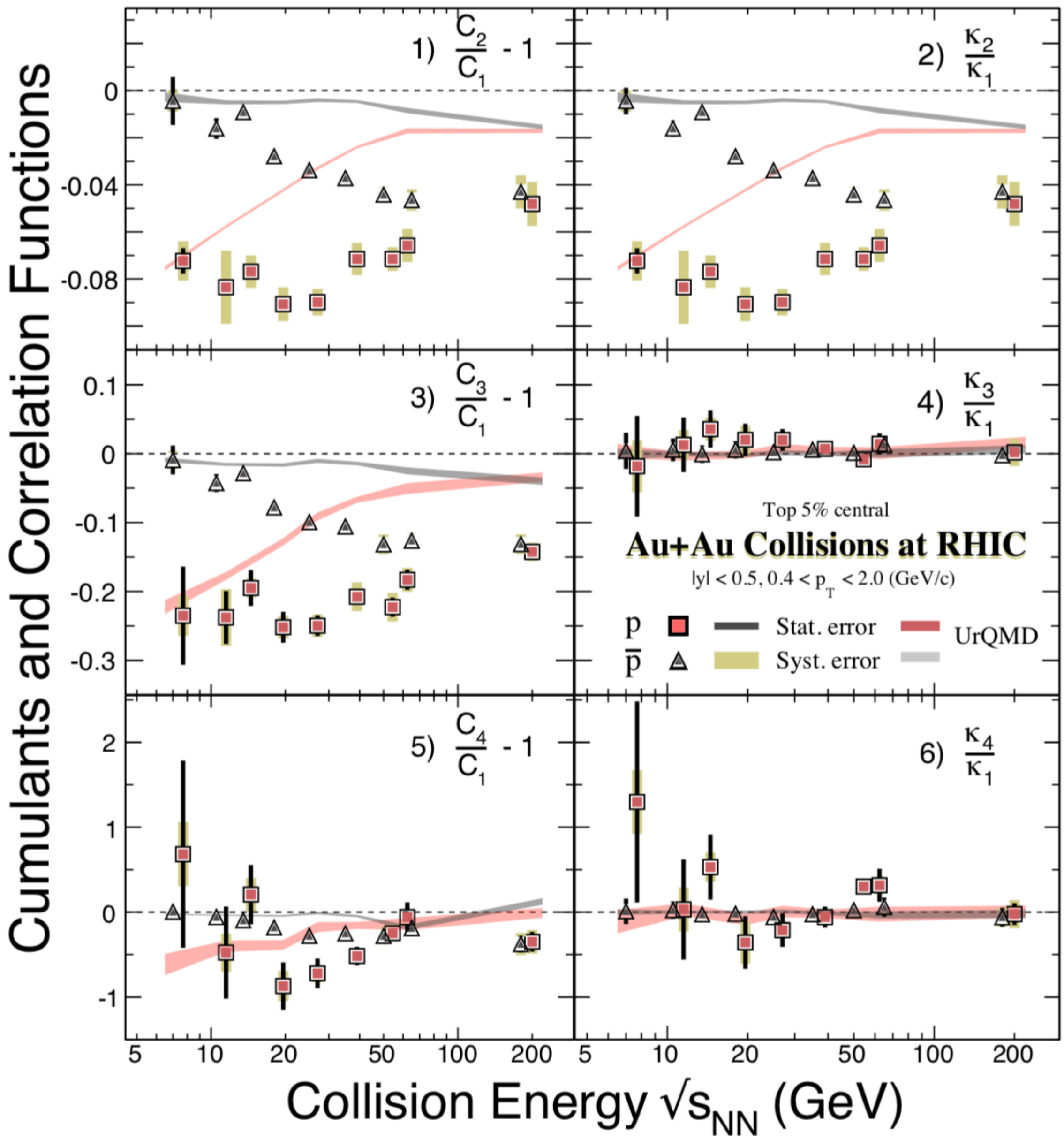

Fig. 4.17: Energy dependence of normalized cumulants and correlation functions of proton and anti-proton multiplicity distributions for Au+Au collisions at $\sqrt{s_{\rm NN}}$ = 7.7, 11.5, 14.5, 19.6, 27, 39, 54.4, 62.4 and 200 GeV. The error bars are statistical errors and the caps represent systematic errors.

correlation functions, separately.

Fig. 4.17 shows the energy dependence of the scaled (anti-)proton cumulants and correlation functions for most central ($0-5\%$) Au+Au collisions. We found that the scaled second cumulants minus unity are negative and show a decreasing trend for proton with decreasing collision energies. These energy dependence trends are mainly dominated by the two-particle correlation of proton. The negative values of κ_2 are mainly due to the effects of baryon number conservation. For the scaled third-order cumulants of proton, the contribution is mainly dominated by the two-particle correlation, due to the small three particle correlation of proton. For the scaled fourth-order cumulants of proton, we observe a non-monotonic energy dependence. The behavior is dominated by the combination of large enhancement of the four-particle and suppression of two-particle as the energy decreases. As discussed in [48, 94, 96], the observed large proton C_4 or κ_4 at $\sqrt{s_{\mathrm{NN}}} = 7.7$ GeV are very important and could be related to the signature of critical point or the first order phase transition. The three and four-particle correlation functions for anti-proton show a flat energy dependence.

We also show the results from UrQMD calculations to compare with the experimental data. The energy dependence trends for second and third-order (anti-)proton cumulants and correlation functions can be qualitatively described by the UrQMD model. However, the non-monotonic energy dependence trend for fourth-order proton cumulants observed in the STAR data cannot be explained by the UrQMD model. On the other hand, the three and four-particle correlation functions for (anti-)proton from UrQMD show almost no energy dependence and are consistent with zero. It indicates that the higher-order (n > 2) (anti-)proton correlation functions are not sensitive to the effect of baryon number conservation, which could serve as a good probe of the critical fluctuations in heavy-ion collisions[82, 83].

4.2 Results for Fixed-Target Collisions

Fig. 4.18 and Fig. 4.19 shows the centrality dependence of $C_1, C_2, C_3, C_4, C_2/C_1, C_3/C_2$ and C_4/C_2 for proton multiplicity distributions for Au+Au collisions in FXT mode at $\sqrt{s_{\mathrm{NN}}} = 4.5$ GeV. The measurements are made in $-2 < y_p < 0$ within $0.4 < p_{\mathrm{T}} < 2.0\,(\mathrm{GeV}/c)$ with efficiency uncorrected and corrected. Due to the low production of anti-proton at $\sqrt{s_{\mathrm{NN}}} = 4.5$ GeV, we only consider the proton. The efficiency corrected C_1 and C_2 values linearly increase with the increasing averaged number of participant nucleons. The efficiency corrected C_3 dropped to zero at most central ($0-5\%$) Au+Au collisions. The C_2/C_1 value has weak centrality dependence. The C_3/C_2 value decreases from mid-central to most central. The C_4/C_2 value increases from mid-central to most central. Since the FXT data is the test run and have very little statistics at $\sqrt{s_{\mathrm{NN}}} = 4.5$ GeV, the results can be wildly inaccurate, but is still can provide a baseline for the future FXT energies.

4.3 Cumulants and Cumulant Ratios for Cu+Cu collisions

Fig. 4.20 shows the centrality dependence of C_1, C_2, C_3 and C_4 for proton, anti-proton and net-proton multiplicity distributions for Cu+Cu collisions at $\sqrt{s_{\mathrm{NN}}} = 22.4$,

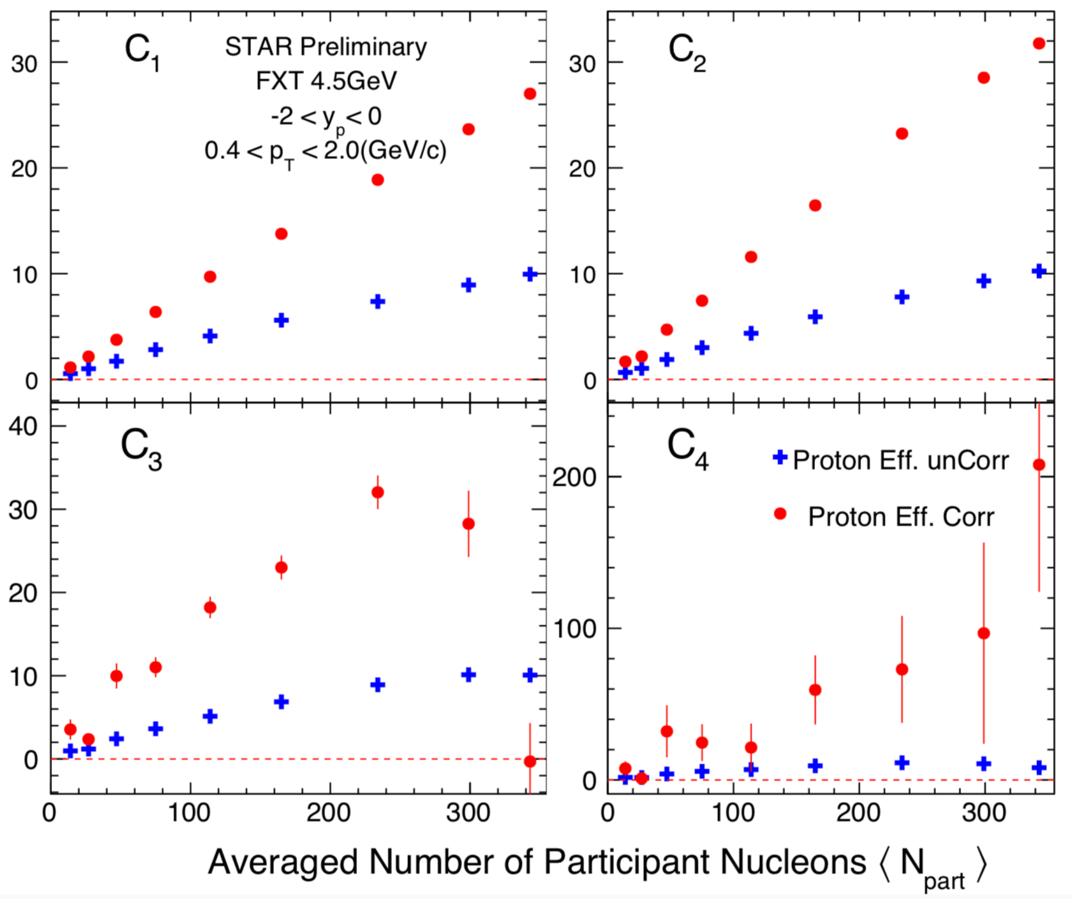

Fig. 4.18: The centrality dependence of C_1, C_2, C_3 and C_4 for proton multiplicity distributions for Au+Au collisions in FXT mode at $\sqrt{s_{\mathrm{NN}}} = 4.5$ GeV. The measurements are made in $-2 < y_p < 0$ within $0.4 < p_{\mathrm{T}} < 2.0\,(\mathrm{GeV}/c)$. The error bars are statistical errors.

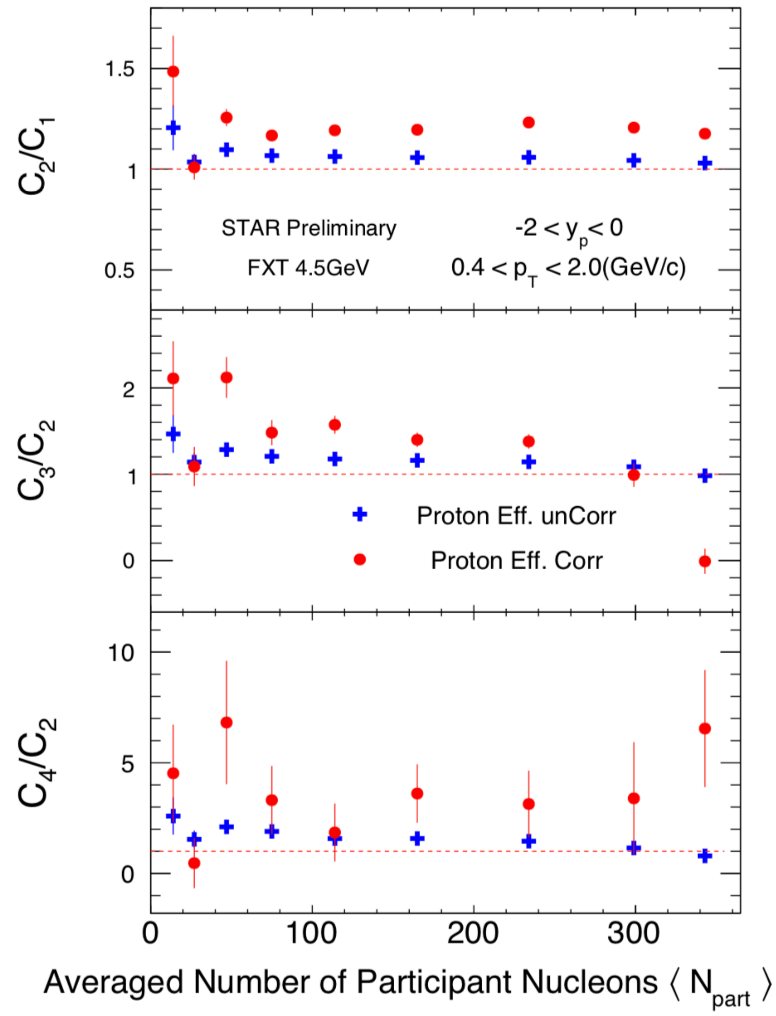

Fig. 4.19: The centrality dependence of $C_2/C_1, C_3/C_2$ and C_4/C_2 for proton multiplicity distributions for Au+Au collisions in FXT mode at $\sqrt{s_{\mathrm{NN}}} = 4.5$ GeV. The measurements are made in $-2 < y_p < 0$ within $0.4 < p_{\mathrm{T}} < 2.0\,(\mathrm{GeV}/c)$. The error bars are statistical errors.

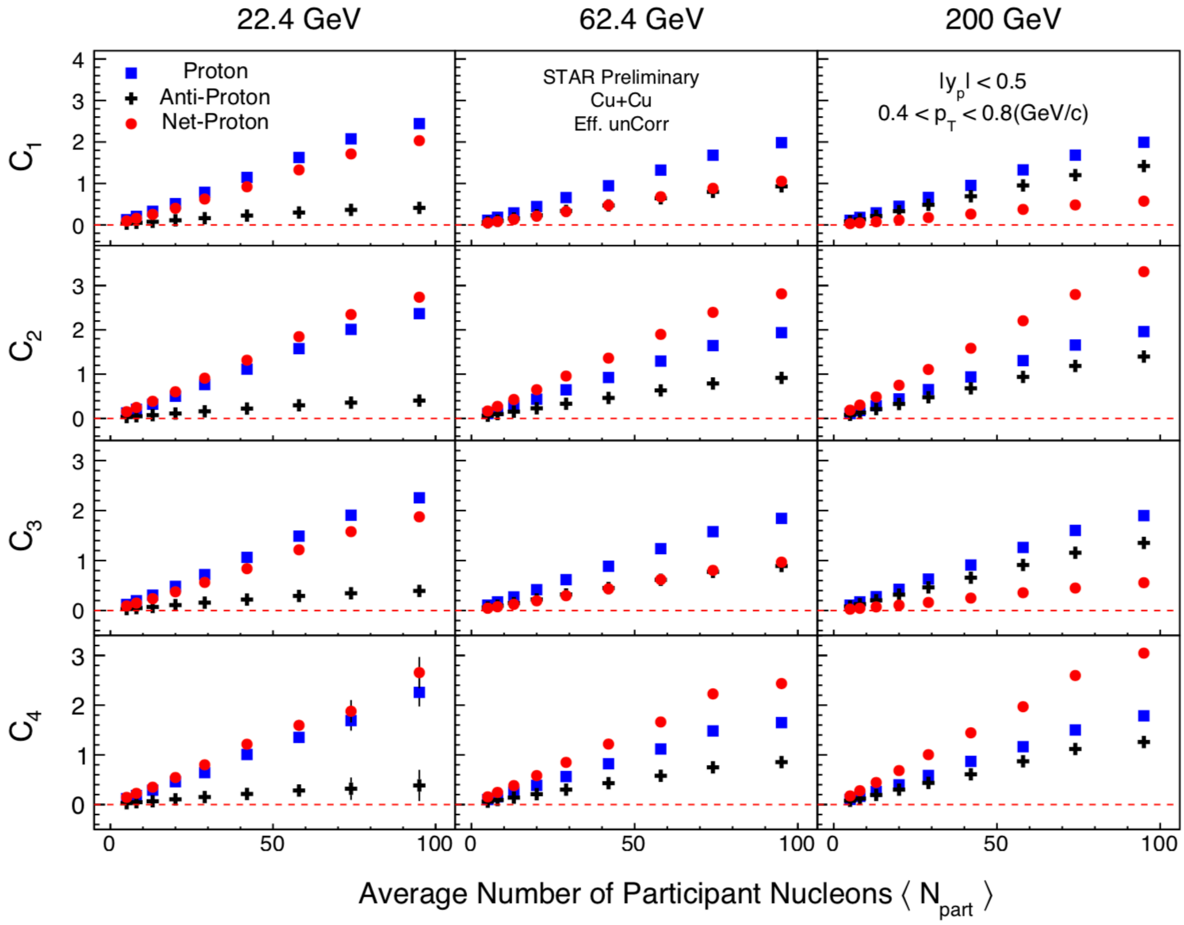

Fig. 4.20: The centrality dependence of C_1, C_2, C_3 and C_4 for proton , anti-proton and net-proton multiplicity distributions for Cu+Cu collisions at $\sqrt{s_{\mathrm{NN}}}$ = 22.4, 62.4 and 200 GeV. The measurements are made in mid-rapidity ($|y_p| < 0.5$) within low p_{T} range ($0.4 < p_{\mathrm{T}} < 0.8\,(\mathrm{GeV}/c)$). The error bars are statistical errors.

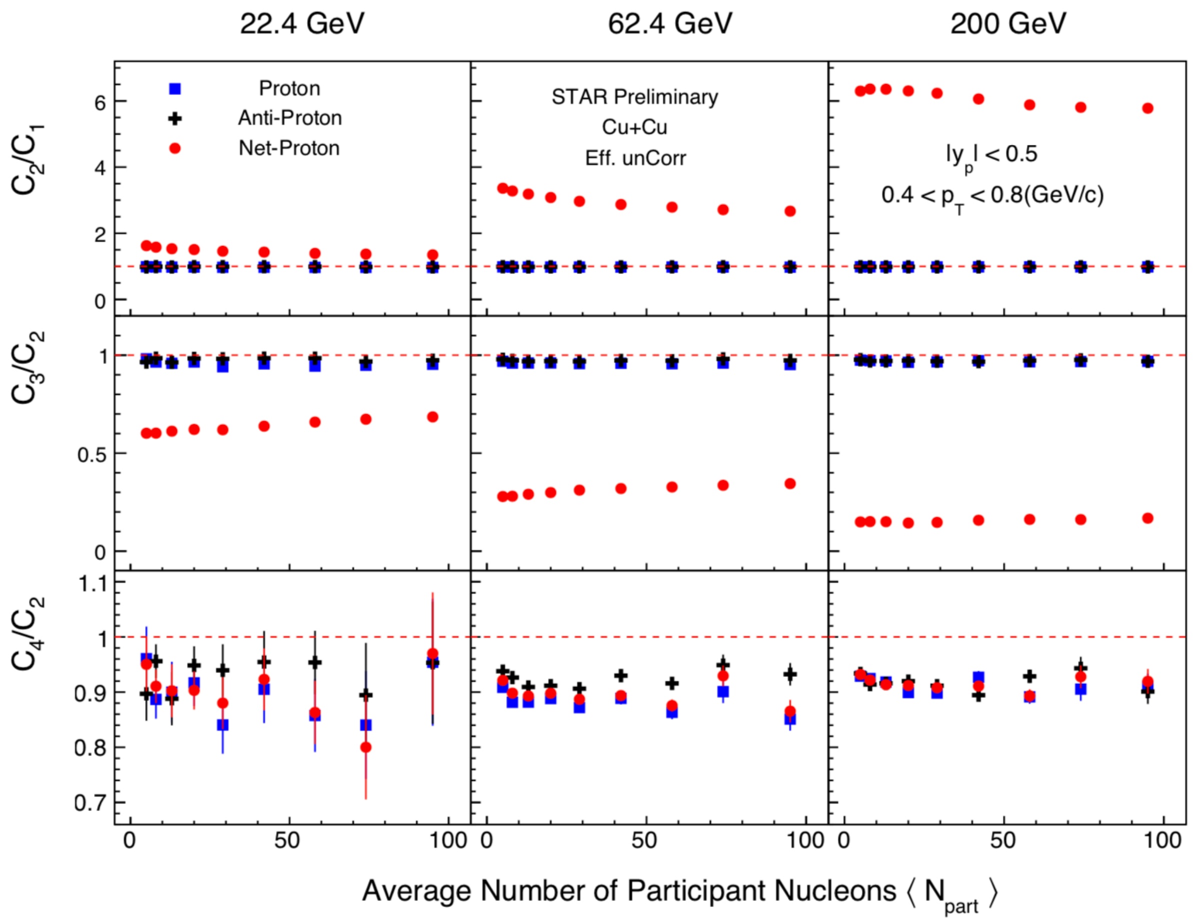

Fig. 4.21: The centrality dependence of $C_2/C_1, C_3/C_2$ and C_4/C_2 for proton multiplicity distributions for Cu+Cu collisions at $\sqrt{s_{\rm NN}}$ = 22.4, 62.4 and 200 GeV. The measurements are made in $|y_p| < 0.5$ within $0.4 < p_{\rm T} < 0.8\,({\rm GeV}/c)$. The error bars are statistical errors.

62.4 and 200 GeV. The measurements are made in $|y_p| < 0.5$ within $0.4 < p_{\rm T} < 0.8\,({\rm GeV}/c)$ with efficiency uncorrected. The efficiency uncorrected cumulants (C_1, C_2, C_3 and C_4) of proton, anti-proton and net-proton linearly increase with the increasing averaged number of participant nucleons.

Fig. 4.21 shows the centrality dependence of $C_2/C_1, C_3/C_2$ and C_4/C_2 for proton, anti-proton and net-proton multiplicity distributions for Cu+Cu collisions at $\sqrt{s_{\rm NN}}$ = 22.4, 62.4 and 200 GeV. The measurements are made in $|y_p| < 0.5$ within $0.4 < p_{\rm T} < 0.8\,({\rm GeV}/c)$ without efficiency corrections. The cumulant ratios ($C_2/C_1, C_3/C_2$ and C_4/C_2) of proton, anti-proton and net-proton have weak centrality dependence.

Fig. 4.22 and Fig. 4.23 shows the energy dependence of $C_1, C_2, C_3, C_4, C_2/C_1, C_3/C_2$ and C_4/C_2 for proton, anti-proton and net-proton multiplicity distributions for most central $(0-5\%)$ Cu+Cu collisions at $\sqrt{s_{\rm NN}}$ = 22.4, 62.4 and 200 GeV. The measurements are made in $|y_p| < 0.5$ within $0.4 < p_{\rm T} < 0.8\,({\rm GeV}/c)$ with efficiency uncorrected. The efficiency uncorrected cumulants (C_1, C_2, C_3 and C_4) of anti-proton linearly increase with the increasing averaged number of participant nucleons. The C_1 and C_3 values of net-proton decrease with the increasing energies. The C_2/C_1 value of net-proton for most central $(0-5\%)$ Cu+Cu collisions increases with the increasing energies. The C_3/C_2 value of net-proton for most central $(0-5\%)$ Cu+Cu collisions decreases with the in-

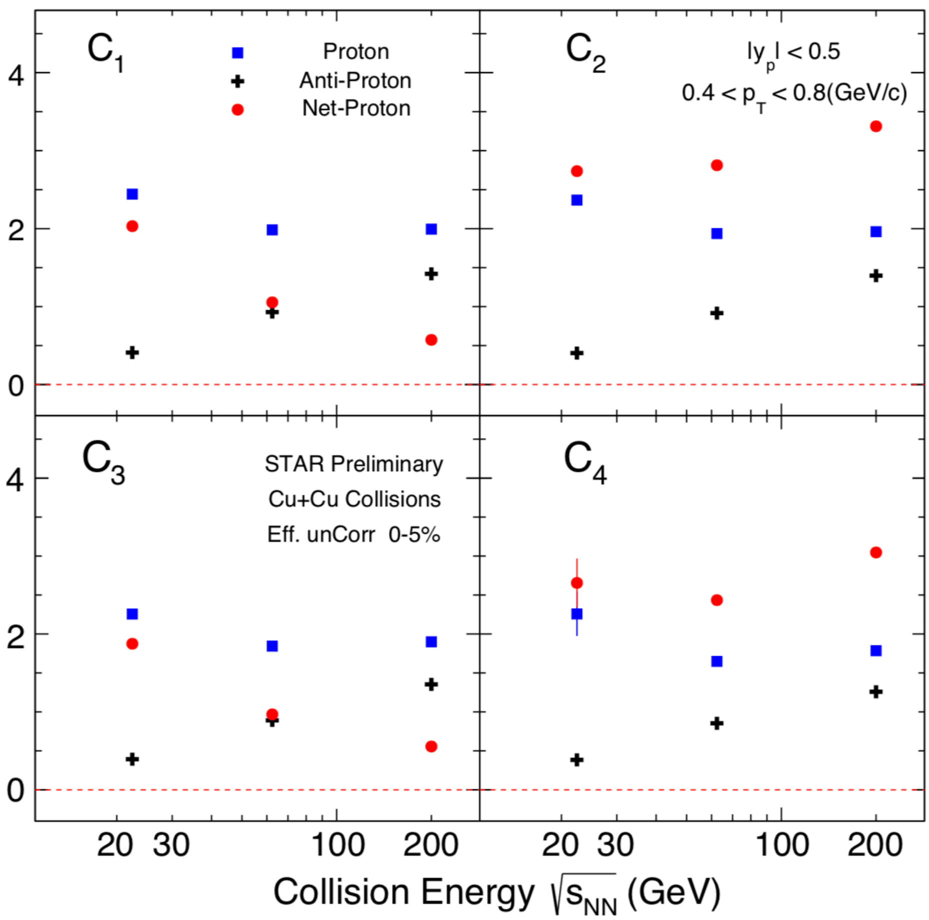

Fig. 4.22: The energy dependence of C_1, C_2, C_3 and C_4 for proton, anti-proton and net-proton multiplicity distributions for most central $(0-5\%)$ Cu+Cu collisions at $\sqrt{s_{\mathrm{NN}}}$ = 22.4, 62.4 and 200 GeV. The measurements are made in mid-rapidity $(|y_p| < 0.5)$ within low p_{T} range $(0.4 < p_{\mathrm{T}} < 0.8\,(\mathrm{GeV}/c)\,)$. The error bars are statistical errors.

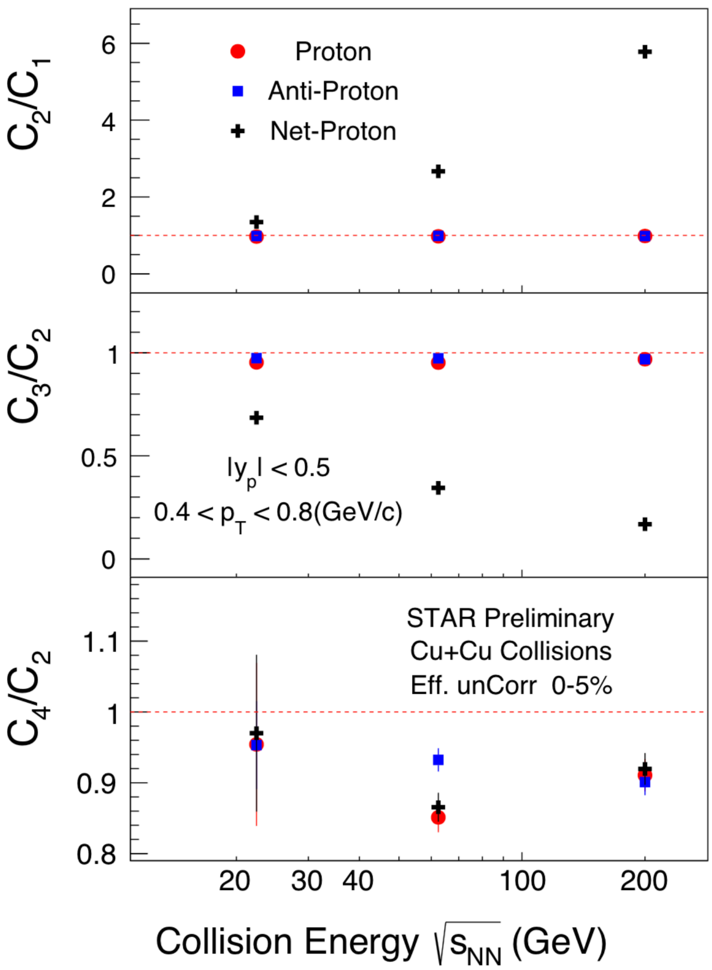

Fig. 4.23: The energy dependence of $C_2/C_1, C_3/C_2$ and C_4/C_2 for proton , anti-proton and net-proton multiplicity distributions for most central $(0-5\%)$ Cu+Cu collisions at $\sqrt{s_{\mathrm{NN}}} = 22.4$, 62.4 and 200 GeV. The measurements are made in mid-rapidity ($|y_p| < 0.5$) within low p_{T} range ($0.4 < p_{\mathrm{T}} < 0.8\,(\mathrm{GeV}/c)$). The error bars are statistical errors.

creasing energies. The C_2/C_1 and C_3/C_2 values for proton and anti-proton for most central $(0-5\%)$ Cu+Cu collisions are close to unity for these three energies and they have weak energy dependence. The C_4/C_2 value for proton and net-proton have weak energy dependence. Since the embedding data for Cu+Cu collisions is in progress, the efficiency corrected results haven't shown in the thesis. However, if the efficiency corrected results for Cu+Cu collisions are done, the comparison with Au+Au collisions can be used as a tool for studying the system size of the system.

Chapter 5

Summary and Outlook

5.1 Summary

In summary, measurements of the cumulants of net-proton, proton and anti-proton distributions up to fourth-order at mid-rapidity ($|y| < 0.5$) within $0.4 < p_{\mathrm{T}} < 2.0\,(\mathrm{GeV}/c)$ in Au+Au collisions over a wide range of $\sqrt{s_{\mathrm{NN}}}$ have been presented to search for a possible critical point and signals of a phase transition in the collisions. The measurements are presented as a function of collision centrality, y, p_{T} and average number of protons and anti-protons in the acceptance. Correlation functions for protons and anti-protons have also been obtained from the measured cumulants for all of the energies studied.

The protons and anti-protons are identified with better than 97% purity using the TPC and TOF detectors of STAR. The centrality selection has been done. Using pions and kaons at mid-rapidity to avoid self-correlation effects for the net-proton, proton and anti-proton fluctuation measurements. The maximum allowed rapidity acceptance at mid-rapidity has been used for centrality determination to minimize the effect of centrality resolution. The variation of average number of protons and anti-protons in a wide centrality bin has been accounted by doing the centrality bin width correction, which also minimizes the volume fluctuation effects. The cumulants are corrected for the proton and anti-proton. Reconstruction efficiency using binomial response function. The statistical errors on the cumulants are based on the delta theorem method and are shown to be consistent with those obtained by the bootstrap method. A detailed estimate of the systematic uncertainties has also been presented. Results on cumulant ratios from hadron resonance gas[87] and UrQMD model[90, 91] have been presented to understand the effect of experimental acceptance in p_{T}, resonance decay, net-proton versus net-baryons and baryon number conservation effects.

The cumulant ratios show a centrality and energy dependence, which are neither reproduced by non-CP transport model calculations, nor by a hadron resonance gas model. Specifically the C_4/C_2 value for the most central $(0-5\%)$ Au+Au collisions shows a non-monotonic variation with $\sqrt{s_{\mathrm{NN}}}$, with 3.1σ signification. A large value of C_4/C_2 is observed for most central $(0-5\%)$ Au+Au collisions at $\sqrt{s_{\mathrm{NN}}} = 7.7$ GeV. This is found to be due to four particle correlations in the system. The rapidity, p_{T} and proton+anti-proton multiplicity acceptance dependence of the cumulants and their ratios provide valuable data to understand the acceptance dependence of the fluctuations in the vicinity of critical point as discussed in [35, 97]. Specifically it will provide information on the range of correlations and their relation to the acceptance of the detector. The data presented here also provide information to extract freeze-out conditions in heavy-ion collisions using QCD based approaches[98–100].

The centrality dependence of cumulants and cumulant ratios of proton multiplicity distributions in rapidity window -2 < y <0 and within $0.4 < p_{\mathrm{T}} < 2.0\,(\mathrm{GeV}/c)$ for Au+Au collisions FXT mode at $\sqrt{s_{\mathrm{NN}}} = 4.5$ GeV have been presented. The centrality and energy dependence of efficiency uncorrected cumulants and cumulant ratios of proton, anti-proton and net-proton multiplicity distributions in rapidity window |y| < 0.5 and within $0.4 < p_{\mathrm{T}} < 0.8\,(\mathrm{GeV}/c)$ for Cu+Cu collisions at $\sqrt{s_{\mathrm{NN}}} = 22.4$, 62.4 and 200 GeV have been presented. Within uncertainties, the most central data of 200 GeV Cu+Cu collisions are consistent with the corresponding centrality of 200 GeV Au+Au collisions.

5.2 Future Prospects

In the second phase of beam energy scan (BES-II) program, STAR will take about 10 to 20 times (depending on energy) statistics data than BES-I to confirm the non-monotonic behavior observed in the fourth order fluctuations ($\kappa\sigma^2$) of net-protons in Au+Au collisions in the BES-I measured by the STAR experiment. With more statistics, the estimated BES-II statistical error will be smaller, and we'll get more precise results for measurements of higher-order moments of net-proton to search for the QCD critical point.

In 2019, RHIC has started the second phase of the beam energy scan program[101]. Due to the stochastic electron cooling of ion beam, the luminosity for low energy runs will be increased by a factor of four to fifteen, depending on beam energy. Meanwhile, the upgrades to the STAR detector system will significantly improve the quality of the measurements[101]. Primarily the goal is to make high-statistics measurements, with extended kinematic range in rapidity and transverse momentum for the measurements discussed in this thesis. In addition, STAR will make further improvements to the centrality selection by having a dedicated detector at forward rapidity compared to the cumulants measurements at mid-rapidity. The extended kinematic range in rapidity and transverse momentum is brought about by upgrading the inner TPC (iTPC)[102] to extend the measurement coverage to $|\eta| < 1.5$, p_{T} acceptance to greater than 100 MeV/c and better dE/dx resolution. Particle identification capability will be extended to $-1.6 < \eta < 1.0$ with the addition of an end-cap TOF (eTOF)[103] detector. The centrality selection will be through the measurements of charged particles using Event Plane Detector (EPD)[104] at $2.1 < |\eta| < 5.1$. This detector is expected to provide forward event plane determination and centrality definition with a better control on self correlation effects. And STAR have successfully installed the three detectors for Run-19. The upgrades of these STAR detectors[105] are shown in Fig. 5.1 and Tab. 5.1. And the event statistics goals for BES-II are given in Tab. 5.2. In addition, STAR will also run in fixed target mode to make measurements up to 700 MeV in μ_B in the QCD phase diagram. In the Fixed Target (FXT) mode, STAR will take about 100 million events at energies from $\sqrt{s_{\mathrm{NN}}} =$ 7.7 to 3.0 GeV, which can further extend the energy coverage of the STAR experiment and allow us to explore the phase structure at higher baryon density region. The event statistics goals for the future FXT program are given in Tab. 5.3. The BES-II program, with these upgrades, will allow for high-statistics measurements, with an extended kinematic range in rapidity and transverse momentum, using sensitive observables, to reveal the structure of the QCD phase diagram.

Fig. 5.2 shows energy dependence of the fourth-order net-proton fluctuations $\kappa\sigma^2$ and

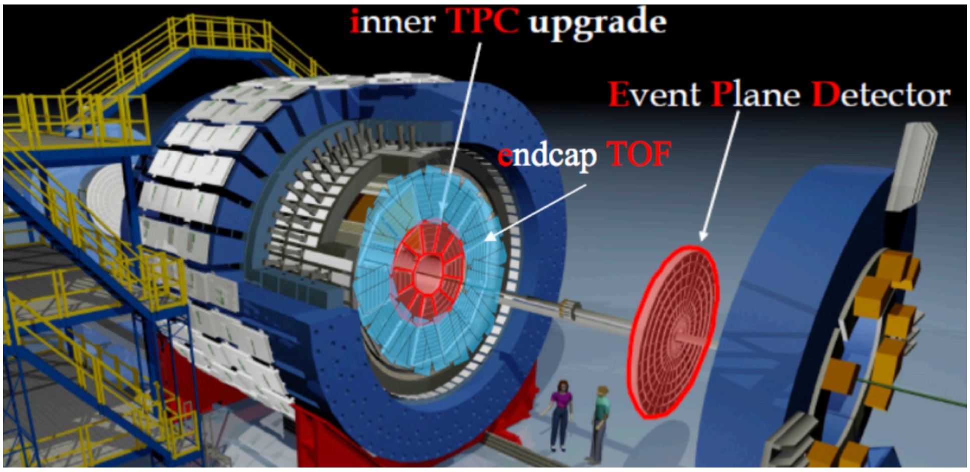

Fig. 5.1: The upgrade of STAR detector

Tab. 5.1: The STAR detector upgrades

iTPC	**EPD**	**eTOF**
$\lvert\eta\rvert < 1.5$	$2.1 < \lvert\eta\rvert < 5.1$	$-1.6 < \eta < -1$
Better dE/dx resolution	Better centrality and event plane resolution	Extend forward PID capability
Fully operational in 2019	Fully operational in 2018	Fully operational in 2019

Tab. 5.2: Statistics for the BES-II

$\sqrt{s_{\rm NN}}$ (GeV)	**BES-II/BES-I**	**Statistics(M)**	μ_B(MeV)	**T(MeV)**
7.7	2021/2010	100/4	422	140
9.1	2020	160	370	140
11.5	2020/2010	230/12	316	152
14.5	2019/2014	300/20	264	156
19.6	2019/2011	400/36	206	160
27	2018/2011	500/ 70	156	162
39	2010	86	112	164
54.4	2017	1000	83	165
62.4	2010	45	73	165
200		238	25	166

Tab. 5.3: Statistics in Au+Au Collisions for Fixed Target mode

FXT Energy	Year	Statistics(M)	μ_B(MeV)
3.0	2020	100	721
3.2			699
3.5			666
3.9	2019		633
4.5			589
5.2	2020		541
6.2			487
7.7	2019		420

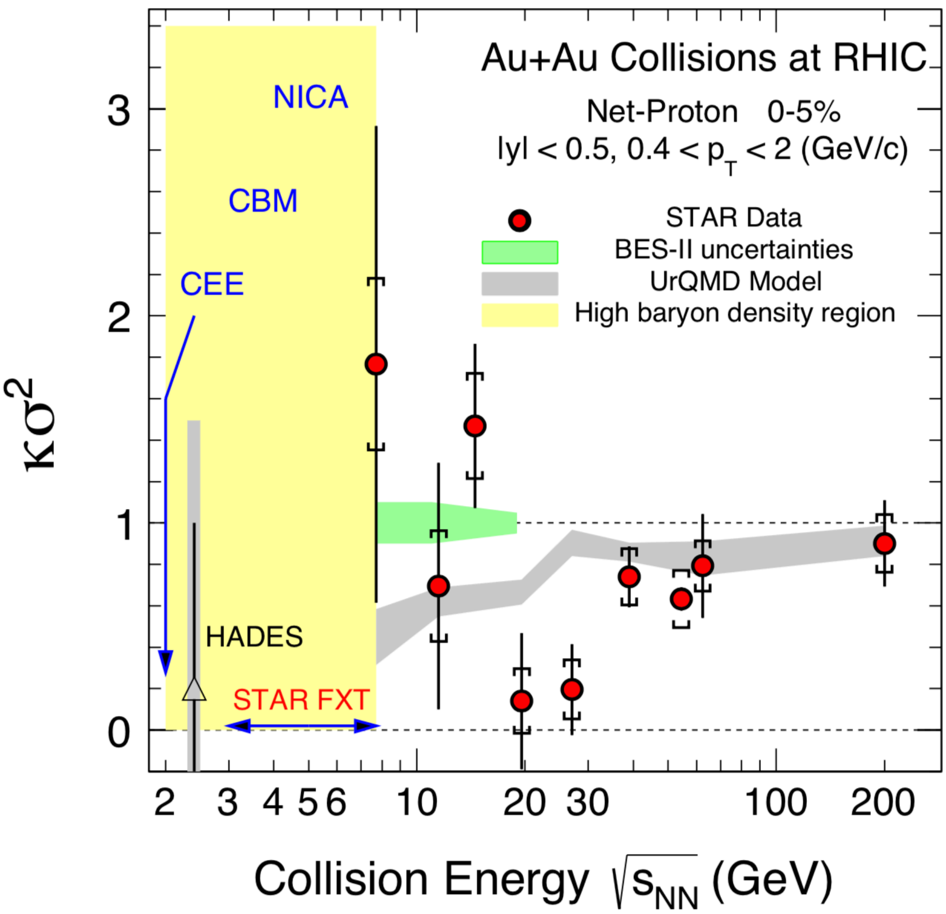

Fig. 5.2: The energy dependence of the fourth-order fluctuations ($\kappa\sigma^2$) of net-proton from BES-I and the estimated statistical BES-II error for net-proton for the most central Au+Au collisions.

the estimated statistical BES-II error for net-proton for the most central Au+Au collisions measured by STAR at RHIC BES-I. Non-monotonic energy dependence behavior has been observed, although the statistical errors are still large at energies below 20 GeV. The HADES experiment recently reported the proton number fluctuation in Au+Au collisions at $\sqrt{s_{\mathrm{NN}}} = 2.4$ GeV[106]. It showed that the fourth order proton number fluctuations $\kappa\sigma^2$ of 0-10% central Au+Au collisions is about 0.2 but with large error bar touching unity, although their kinematic cuts of protons are $0.4 < p_{\mathrm{T}} < 1.6$ (GeV/c), $|\mathrm{y}| < 0.4$[106], while the cut for STAR is $0.4 < p_{\mathrm{T}} < 2.0\,(\mathrm{GeV}/c)$, $|\mathrm{y}| < 0.5$[27]. Thus, obviously, it is very crucial to perform precise measurement of proton number fluctuation between $\sqrt{s_{\mathrm{NN}}} = 2{-}8$ GeV to confirm the possible peak structure at low energy region, which is predicted by the theoretical model calculations with the assumption of presence of QCD critical point. If the peak structure was confirmed, it might be the signature of QCD critical point and/or the first order phase transition. In the near future, precise measurement will be made with high statistics data from BES-II, both in collider ($\sqrt{s_{\mathrm{NN}}} = 7.7{-}19.6$ GeV) and FXT mode ($\sqrt{s_{\mathrm{NN}}} = 3{-}7.7$ GeV)[107]. The state of the art experimental facilities, such as FAIR ($\sqrt{s_{\mathrm{NN}}} = 2{-}5$ GeV, CBM: FXT exp.)[108, 109], HIAF ($\sqrt{s_{\mathrm{NN}}}$ up to 2.25 GeV[110], CEE: FXT exp.) and NICA ($\sqrt{s_{\mathrm{NN}}} = 4{-}11$ GeV, MPD: collider exp.)[111], aiming to explore the QCD phase structure at high baryon density are also under construction.

Reference

[1] S. Bethke, Eur. Phys. J. C **64**, 689 (2009) doi:10.1140/epjc/s10052-009-1173-1 [arXiv:0908.1135 [hep-ph]].

[2] S. Bethke, Prog. Part. Nucl. Phys. **58**, 351 (2007) doi:10.1016/j.ppnp.2006.06.001 [hep-ex/0606035].

[3] M. G. Alford, K. Rajagopal and F. Wilczek, Phys. Lett. B **422**, 247 (1998) doi:10.1016/S0370-2693(98)00051-3 [hep-ph/9711395].

[4] S. Ejiri, Phys. Rev. D **78**, 074507 (2008) doi:10.1103/PhysRevD.78.074507 [arXiv:0804.3227 [hep-lat]].

[5] P. de Forcrand and O. Philipsen, Nucl. Phys. B **642**, 290-306 (2002) doi:10.1016/S0550-3213(02)00626-0 [arXiv:hep-lat/0205016 [hep-lat]].

[6] G. Endrodi, Z. Fodor, S. D. Katz and K. K. Szabo, JHEP **1104**, 001 (2011) doi:10.1007/JHEP04(2011)001 [arXiv:1102.1356 [hep-lat]].

[7] Y. Aoki, G. Endrodi, Z. Fodor, S. D. Katz and K. K. Szabo, Nature **443**, 675 (2006) doi:10.1038/nature05120 [hep-lat/0611014].

[8] M. A. Stephanov, Prog. Theor. Phys. Suppl. **153**, 139 (2004) [Int. J. Mod. Phys. A **20**, 4387 (2005)] doi:10.1142/S0217751X05027965 [hep-ph/0402115].

[9] R. V. Gavai, Contemp. Phys. **57**, no. 3, 350 (2016). doi:10.1080/00107514.2016.1144914

[10] R. V. Gavai, Pramana **84**, no.5, 757-771 (2015) doi:10.1007/s12043-015-0983-y [arXiv:1404.6615 [hep-ph]].

[11] B. I. Abelev *et al.* [STAR Collaboration], Phys. Rev. C **81**, 024911 (2010) doi:10.1103/PhysRevC.81.024911 [arXiv:0909.4131 [nucl-ex]].

[12] J. M. Heuser [CBM Collaboration], Nucl. Phys. A **830**, 563C (2009) doi:10.1016/j.nuclphysa.2009.09.048 [arXiv:0907.2136 [nucl-ex]].

[13] B. Mohanty, Nucl. Phys. A **830**, 899C (2009) doi:10.1016/j.nuclphysa.2009.10.132 [arXiv:0907.4476 [nucl-ex]].

[14] E. S. Bowman and J. I. Kapusta, Phys. Rev. C **79**, 015202 (2009) doi:10.1103/PhysRevC.79.015202 [arXiv:0810.0042 [nucl-th]].

[15] M. A. Stephanov, Phys. Rev. Lett. **107**, 052301 (2011) doi:10.1103/PhysRevLett.107.052301 [arXiv:1104.1627 [hep-ph]].

[16] M. A. Stephanov, Phys. Rev. Lett. **102**, 032301 (2009) doi:10.1103/PhysRevLett.102.032301 [arXiv:0809.3450 [hep-ph]].

[17] Z. Yang, X. Luo and B. Mohanty, Phys. Rev. C **95**, no. 1, 014914 (2017) doi:10.1103/PhysRevC.95.014914 [arXiv:1610.07580 [nucl-ex]].

[18] A. Chatterjee [STAR Collaboration], PoS CORFU **2018**, 164 (2019) doi:10.22323/1.347.0164 [arXiv:1904.01302 [hep-ex]].

[19] Y. Hatta and M. A. Stephanov, Phys. Rev. Lett. **91**, 102003 (2003) Erratum: [Phys. Rev. Lett. **91**, 129901 (2003)] doi:10.1103/PhysRevLett.91.102003, 10.1103/PhysRevLett.91.129901 [hep-ph/0302002].

[20] C. Athanasiou, K. Rajagopal and M. Stephanov, Phys. Rev. D **82**, 074008 (2010) doi:10.1103/PhysRevD.82.074008 [arXiv:1006.4636 [hep-ph]].

[21] B. J. Schaefer and M. Wagner, Phys. Rev. D **85**, 034027 (2012) doi:10.1103/PhysRevD.85.034027 [arXiv:1111.6871 [hep-ph]].

[22] S. Gupta, X. Luo, B. Mohanty, H. G. Ritter and N. Xu, Science **332**, 1525 (2011) doi:10.1126/science.1204621 [arXiv:1105.3934 [hep-ph]].

[23] M. Asakawa, S. Ejiri and M. Kitazawa, Phys. Rev. Lett. **103**, 262301 (2009) doi:10.1103/PhysRevLett.103.262301 [arXiv:0904.2089 [nucl-th]].

[24] M. Kitazawa and M. Asakawa, Phys. Rev. C **85**, 021901 (2012) doi:10.1103/PhysRevC.85.021901 [arXiv:1107.2755 [nucl-th]].

[25] A. Bzdak and V. Koch, Phys. Rev. C **86**, 044904 (2012) doi:10.1103/PhysRevC.86.044904 [arXiv:1206.4286 [nucl-th]].

[26] V. Koch, Chapter of the book ”Relativistic Heavy Ion Physics”, R. Stock (Ed.), Springer, Heidelberg, 2010, p. 626-652. (Landolt-Boernstein New Series I, v. 23). (ISBN: 978-3-642-01538-0, 978-3-642-01539-7 (eBook)) doi:10.1007/978-3-642-01539-7_20 [arXiv:0810.2520 [nucl-th]].

[27] J. Adam *et al.* [STAR Collaboration], arXiv:2001.02852 [nucl-ex].

[28] J. Xu, J. Phys. Conf. Ser. **736**, no.1, 012002 (2016) doi:10.1088/1742-6596/736/1/012002 [arXiv:1611.07134 [hep-ex]].

[29] J. Thäder [STAR], Nucl. Phys. A **956**, 320-323 (2016) doi:10.1016/j.nuclphysa.2016.02.047 [arXiv:1601.00951 [nucl-ex]].

[30] X. Luo [STAR], PoS **CPOD2014**, 019 (2015) doi:10.22323/1.217.0019 [arXiv:1503.02558 [nucl-ex]].

[31] X. Luo, Nucl. Phys. A **956**, 75-82 (2016) doi:10.1016/j.nuclphysa.2016.03.025 [arXiv:1512.09215 [nucl-ex]].

[32] M. Kitazawa and X. Luo, Phys. Rev. C **96**, no.2, 024910 (2017) doi:10.1103/PhysRevC.96.024910 [arXiv:1704.04909 [nucl-th]].

[33] D. K. Mishra, P. K. Netrakanti and P. Garg, Phys. Rev. C **95**, no. 5, 054905 (2017) doi:10.1103/PhysRevC.95.054905 [arXiv:1705.04440 [nucl-th]].

[34] A. Bzdak, V. Koch and N. Strodthoff, Phys. Rev. C **95**, no. 5, 054906 (2017) doi:10.1103/PhysRevC.95.054906 [arXiv:1607.07375 [nucl-th]].

[35] B. Ling and M. A. Stephanov, Phys. Rev. C **93**, no.3, 034915 (2016) doi:10.1103/PhysRevC.93.034915 [arXiv:1512.09125 [nucl-th]].

[36] K. Ackermann *et al.* [STAR Collaboration], Nucl. Instrum. Meth. A **499**, 624-632 (2003) doi:10.1016/S0168-9002(02)01960-5

[37] M. Anderson, *et al.* [STAR Collaboration], Nucl. Instrum. Meth. A **499**, 659-678 (2003) doi:10.1016/S0168-9002(02)01964-2 [arXiv:nucl-ex/0301015 [nucl-ex]].

[38] W. J. Llope [STAR Collaboration], AIP Conf. Proc. **1099**, no. 1, 778 (2009). doi:10.1063/1.3120153

[39] W. Llope, F. Geurts, J. Mitchell, Z. Liu, N. Adams, G. Eppley, D. Keane, J. Li, F. Liu, L. Liu, G. Mutchler, T. Nussbaum, B. Bonner, P. Sappenfield, B. Zhang and W. Zhang, Nucl. Instrum. Meth. A **522**, 252-273 (2004) doi:10.1016/j.nima.2003.11.414 [arXiv:nucl-ex/0308022 [nucl-ex]].

[40] W. Llope , *et al.*[STAR Collaboration], Nucl. Instrum. Meth. A **661**, S110-S113 (2012) doi:10.1016/j.nima.2010.07.086

[41] W. Llope, *et al.* [STAR Collaboration], Nucl. Instrum. Meth. A **759**, 23-28 (2014) doi:10.1016/j.nima.2014.04.080 [arXiv:1403.6855 [physics.ins-det]].

[42] Alex Schah. Collaboration Communications.

[43] William R. Leo, Techniques for Nuclear and Particle Physics Experiments. ISBN 978-3-642-57920-2 (eBook) doi:10.1007/978-3-642-57920-2.

[44] https://drupal.star.bnl.gov/STAR/starnotes/public/sn0439

[45] W. Llope, Nucl. Instrum. Meth. B **241**, 306-310 (2005) doi:10.1016/j.nimb.2005.07.089

[46] K. C. Meehan [STAR], Nucl. Phys. A **956**, 878-881 (2016) doi:10.1016/j.nuclphysa.2016.04.016

[47] L. Adamczyk *et al.* [STAR Collaboration], Phys. Rev. C **96**, no. 4, 044904 (2017) doi:10.1103/PhysRevC.96.044904 [arXiv:1701.07065 [nucl-ex]].

[48] A. Bzdak, V. Koch, D. Oliinychenko and J. Steinheimer, Phys. Rev. C **98**, no.5, 054901 (2018) doi:10.1103/PhysRevC.98.054901 [arXiv:1804.04463 [nucl-th]].

[49] D. Ashery and J. Schiffer, Ann. Rev. Nucl. Part. Sci. **36**, 207-252 (1986) doi:10.1146/annurev.ns.36.120186.001231

[50] B. Abelev *et al.* [STAR], Phys. Rev. C **79**, 034909 (2009) doi:10.1103/PhysRevC.79.034909 [arXiv:0808.2041 [nucl-ex]].

[51] J. Adam *et al.* [STAR], Phys. Rev. C **101**, no.2, 024905 (2020) doi:10.1103/PhysRevC.101.024905 [arXiv:1908.03585 [nucl-ex]].

[52] M. L. Miller, K. Reygers, S. J. Sanders and P. Steinberg, Ann. Rev. Nucl. Part. Sci. **57**, 205 (2007) doi:10.1146/annurev.nucl.57.090506.123020 [nucl-ex/0701025].

[53] R. S. Hollis *et al.* [PHOBOS Collaboration], J. Phys. Conf. Ser. **5**, 46 (2005). doi:10.1088/1742-6596/5/1/004

[54] D. Kharzeev and M. Nardi, Phys. Lett. B **507**, 121 (2001) doi:10.1016/S0370-2693(01)00457-9 [nucl-th/0012025].

[55] X. Luo, J. Xu, B. Mohanty and N. Xu, J. Phys. G **40**, 105104 (2013) doi:10.1088/0954-3899/40/10/105104 [arXiv:1302.2332 [nucl-ex]].

[56] A. Chatterjee, Y. Zhang, J. Zeng, N. R. Sahoo and X. Luo, Phys. Rev. C **101**, no.3, 034902 (2020) doi:10.1103/PhysRevC.101.034902 [arXiv:1910.08004 [nucl-ex]].

[57] X. Luo, Phys. Rev. C **91**, no. 3, 034907 (2015) Erratum: [Phys. Rev. C **94**, no. 5, 059901 (2016)] doi:10.1103/PhysRevC.91.034907, 10.1103/PhysRevC.94.059901 [arXiv:1410.3914 [physics.data-an]].

[58] S. He and X. Luo, Chin. Phys. C **42**, no.10, 104001 (2018) doi:10.1088/1674-1137/42/10/104001 [arXiv:1802.02911 [physics.data-an]].

[59] A. Bzdak and V. Koch, Phys. Rev. C **91**, no.2, 027901 (2015) doi:10.1103/PhysRevC.91.027901 [arXiv:1312.4574 [nucl-th]].

[60] L. Adamczyk *et al.* [STAR Collaboration], Phys. Rev. Lett. **112**, 032302 (2014) doi:10.1103/PhysRevLett.112.032302 [arXiv:1309.5681 [nucl-ex]].

[61] A. Bzdak, R. Holzmann and V. Koch, Phys. Rev. C **94**, no.6, 064907 (2016) doi:10.1103/PhysRevC.94.064907 [arXiv:1603.09057 [nucl-th]].

[62] X. Luo and T. Nonaka, Phys. Rev. C **99**, no.4, 044917 (2019) doi:10.1103/PhysRevC.99.044917 [arXiv:1812.10303 [physics.data-an]].

[63] X. Luo, J. Phys. G **39**, 025008 (2012) doi:10.1088/0954-3899/39/2/025008 [arXiv:1109.0593 [physics.data-an]].

[64] R. Barlow, hep-ex/0207026.

[65] J. Li, H. Xu and H. Song, Phys. Rev. C **97**, no.1, 014902 (2018) doi:10.1103/PhysRevC.97.014902 [arXiv:1707.09742 [nucl-th]].

[66] Y. Lin, L. Chen and Z. Li, Phys. Rev. C **96**, no.4, 044906 (2017) doi:10.1103/PhysRevC.96.044906 [arXiv:1707.04375 [hep-ph]].

[67] G. A. Almasi, B. Friman and K. Redlich, Phys. Rev. D **96**, no.1, 014027 (2017) doi:10.1103/PhysRevD.96.014027 [arXiv:1703.05947 [hep-ph]].

[68] C. Zhou, J. Xu, X. Luo and F. Liu, Phys. Rev. C **96**, no.1, 014909 (2017) doi:10.1103/PhysRevC.96.014909 [arXiv:1703.09114 [nucl-ex]].

[69] A. Zhao, X. Luo and H. Zong, Eur. Phys. J. C **77**, no.4, 207 (2017) doi:10.1140/epjc/s10052-017-4784-y [arXiv:1609.01416 [nucl-th]].

[70] J. Xu, S. Yu, F. Liu and X. Luo, Phys. Rev. C **94**, no.2, 024901 (2016) doi:10.1103/PhysRevC.94.024901 [arXiv:1606.03900 [nucl-ex]].

[71] V. Vovchenko, L. Jiang, M. I. Gorenstein and H. Stoecker, Phys. Rev. C **98**, no.2, 024910 (2018) doi:10.1103/PhysRevC.98.024910 [arXiv:1711.07260 [nucl-th]].

[72] M. Albright, J. Kapusta and C. Young, Phys. Rev. C **92**, no.4, 044904 (2015) doi:10.1103/PhysRevC.92.044904 [arXiv:1506.03408 [nucl-th]].

[73] K. Fukushima, Phys. Rev. C **91**, no.4, 044910 (2015) doi:10.1103/PhysRevC.91.044910 [arXiv:1409.0698 [hep-ph]].

[74] P. Netrakanti, X. Luo, D. Mishra, B. Mohanty, A. Mohanty and N. Xu, Nucl. Phys. A **947**, 248-259 (2016) doi:10.1016/j.nuclphysa.2016.01.005 [arXiv:1405.4617 [hep-ph]].

[75] K. Morita, B. Friman and K. Redlich, Phys. Lett. B **741**, 178-183 (2015) doi:10.1016/j.physletb.2014.12.037 [arXiv:1402.5982 [hep-ph]].

[76] S. Samanta and B. Mohanty, [arXiv:1905.09311 [hep-ph]].

[77] S. He, X. Luo, Y. Nara, S. Esumi and N. Xu, Phys. Lett. B **762**, 296-300 (2016) doi:10.1016/j.physletb.2016.09.053 [arXiv:1607.06376 [nucl-ex]].

[78] M. Kitazawa and M. Asakawa, Phys. Rev. C **86**, 024904 (2012) doi:10.1103/PhysRevC.86.024904 [arXiv:1205.3292 [nucl-th]].

[79] M. Nahrgang, M. Bluhm, P. Alba, R. Bellwied and C. Ratti, Eur. Phys. J. C **75**, no.12, 573 (2015) doi:10.1140/epjc/s10052-015-3775-0 [arXiv:1402.1238 [hep-ph]].

[80] D. Mishra, P. Garg, P. Netrakanti and A. Mohanty, Phys. Rev. C **94**, no.1, 014905 (2016) doi:10.1103/PhysRevC.94.014905 [arXiv:1607.01875 [hep-ph]].

[81] M. Bluhm, M. Nahrgang, S. A. Bass and T. Schaefer, Eur. Phys. J. C **77**, no.4, 210 (2017) doi:10.1140/epjc/s10052-017-4771-3 [arXiv:1612.03889 [nucl-th]].

[82] Y. Zhang, S. He, H. Liu, Z. Yang and X. Luo, Phys. Rev. C **101**, no.3, 034909 (2020) doi:10.1103/PhysRevC.101.034909 [arXiv:1905.01095 [nucl-ex]].

[83] S. He and X. Luo, Phys. Lett. B **774**, 623-629 (2017) doi:10.1016/j.physletb.2017.10.030 [arXiv:1704.00423 [nucl-ex]].

[84] F. Karsch, K. Morita and K. Redlich, Phys. Rev. C **93**, no.3, 034907 (2016) doi:10.1103/PhysRevC.93.034907 [arXiv:1508.02614 [hep-ph]].

[85] A. Bzdak, V. Koch and V. Skokov, Phys. Rev. C **87**, no.1, 014901 (2013) doi:10.1103/PhysRevC.87.014901 [arXiv:1203.4529 [hep-ph]].

[86] P. Braun-Munzinger, A. Rustamov and J. Stachel, [arXiv:1907.03032 [nucl-th]].

[87] P. Garg, D. Mishra, P. Netrakanti, B. Mohanty, A. Mohanty, B. Singh and N. Xu, Phys. Lett. B **726**, 691-696 (2013) doi:10.1016/j.physletb.2013.09.019 [arXiv:1304.7133 [nucl-ex]].

[88] F. Karsch and K. Redlich, Phys. Lett. B **695**, 136-142 (2011) doi:10.1016/j.physletb.2010.10.046 [arXiv:1007.2581 [hep-ph]].

[89] A. N. Tawfik, Int. J. Mod. Phys. A **29**, no.17, 1430021 (2014) doi:10.1142/S0217751X1430021X [arXiv:1410.0372 [hep-ph]].

[90] S. Bass, M. Belkacem, M. Bleicher, M. Brandstetter, L. Bravina, C. Ernst, L. Gerland, M. Hofmann, S. Hofmann, J. Konopka, G. Mao, L. Neise, S. Soff, C. Spieles, H. Weber, L. Winckelmann, H. Stoecker, W. Greiner, C. Hartnack, J. Aichelin and N. Amelin, Prog. Part. Nucl. Phys. **41**, 255-369 (1998) doi:10.1016/S0146-6410(98)00058-1 [arXiv:nucl-th/9803035 [nucl-th]].

[91] M. Bleicher, E. Zabrodin, C. Spieles, S. Bass, C. Ernst, S. Soff, L. Bravina, M. Belkacem, H. Weber, H. Stoecker and W. Greiner, J. Phys. G **25**, 1859-1896 (1999) doi:10.1088/0954-3899/25/9/308 [arXiv:hep-ph/9909407 [hep-ph]].

[92] M. Aggarwal *et al.* [STAR], Phys. Rev. Lett. **105**, 022302 (2010) doi:10.1103/PhysRevLett.105.022302 [arXiv:1004.4959 [nucl-ex]].

[93] M. Sakaida, M. Asakawa, H. Fujii and M. Kitazawa, Phys. Rev. C **95**, no.6, 064905 (2017) doi:10.1103/PhysRevC.95.064905 [arXiv:1703.08008 [nucl-th]].

[94] V. Braun, Y. He, B. A. Ovrut and T. Pantev, JHEP **01**, 025 (2006) doi:10.1088/1126-6708/2006/01/025 [arXiv:hep-th/0509051 [hep-th]].

[95] M. Cheng, P. Hegde, C. Jung, F. Karsch, O. Kaczmarek, E. Laermann, R. Mawhinney, C. Miao, P. Petreczky, C. Schmidt and W. Soeldner, Phys. Rev. D **79**, 074505 (2009) doi:10.1103/PhysRevD.79.074505 [arXiv:0811.1006 [hep-lat]].

[96] A. Bzdak, V. Koch and V. Skokov, Eur. Phys. J. C **77**, no.5, 288 (2017) doi:10.1140/epjc/s10052-017-4847-0 [arXiv:1612.05128 [nucl-th]].

[97] J. Brewer, S. Mukherjee, K. Rajagopal and Y. Yin, Phys. Rev. C **98**, no.6, 061901 (2018) doi:10.1103/PhysRevC.98.061901 [arXiv:1804.10215 [hep-ph]].

[98] A. Bazavov, H. Ding, P. Hegde, O. Kaczmarek, F. Karsch, E. Laermann, S. Mukherjee, P. Petreczky, C. Schmidt, D. Smith, W. Soeldner and M. Wagner, Phys. Rev. Lett. **109**, 192302 (2012) doi:10.1103/PhysRevLett.109.192302 [arXiv:1208.1220 [hep-lat]].

[99] S. Borsanyi, Z. Fodor, S. Katz, S. Krieg, C. Ratti and K. Szabo, Phys. Rev. Lett. **111**, 062005 (2013) doi:10.1103/PhysRevLett.111.062005 [arXiv:1305.5161 [hep-lat]].

[100] P. Alba, W. Alberico, R. Bellwied, M. Bluhm, V. Mantovani Sarti, M. Nahrgang and C. Ratti, Phys. Lett. B **738**, 305-310 (2014) doi:10.1016/j.physletb.2014.09.052 [arXiv:1403.4903 [hep-ph]].

[101] BES-II White paper:, STAR Note 0598:
`https://drupal.star.bnl.gov/STAR/starnotes/public/sn0598`

[102] iTPC proposal, STAR Note 0619:
`https://drupal.star.bnl.gov/STAR/starnotes/public/sn0619`

[103] eTOF proposal, STAR Note 0665:
https://drupal.star.bnl.gov/STAR/starnotes/public/sn0665

[104] EPD proposal, STAR Note 0666:
https://drupal.star.bnl.gov/STAR/starnotes/public/sn0666

[105] STAR Beam Use Request:
https://drupal.star.bnl.gov/STAR/system/files/BUR2019_final_0_0.pdf

[106] J. Adamczewski-Musch *et al.* [HADES Collaboration], arXiv:2002.08701 [nucl-ex].

[107] Available online: https://drupal.star.bnl.gov

[108] Available online: https://fair-center.eu/ and CBM https://fair-center.eu/user/experiments/nuclear-matter-physics/cbm.html

[109] T. Ablyazimov *et al.* [CBM Collaboration], Eur. Phys. J. A **53**, no. 3, 60 (2017) doi:10.1140/epja/i2017-12248-y [arXiv:1607.01487 [nucl-ex]].

[110] Available online: http://hiaf.impcas.ac.cn

[111] NICA white paper. Available online: http://nica.jinr.ru/files/WhitePaper.pdf

Publications and Presentations

Papers

1. Baryon-Strangeness correlations in Au+Au collisions at $\sqrt{s_{NN}}$ = 7.7 - 200 GeV from UrQMD model.
   Zhenzhen Yang, Xiaofeng Luo and Bedangadas Mohanty.
   Phys. Rev. C. 95, 014914(2017).

2. Effects of Weak Decay and Hadronic Scattering on the Proton Number Fluctuations in Au + Au Collisions at $\sqrt{s_{NN}}$ = 5GeV from JAM Model.
   Yu Zhang, Shu He, Hui Liu, Zhenzhen Yang, Xiaofeng Luo.
   Phys. Rev. C. 101, 034909(2020).

3. Net-proton Number Fluctuations and the Quantum Chromodynamics Critical Point.
   Primary authors (alphabetically): Shu He, Xiaofeng Luo, Bedanga Mohanty, Toshihiro Nonaka, Nu Xu, Zhenzhen Yang, Yu Zhang.

   For the STAR Collaboration. **e-Print: arXiv:2001.02852. Target Journal: Nature Physics**

4. Measurements of Cumulants of Net-proton, Proton and Anti-proton Multiplicity Distributions at RHIC
   Primary authors (alphabetically): Shu He, Xiaofeng Luo, Bedanga Mohanty, Toshihiro Nonaka, Nu Xu, Zhenzhen Yang, Yu Zhang.

   For the STAR Collaboration. **Target Journal: Phys. Rev. C**.

Presentations

1. The XXV international conference on Ultrarelativistic Heavy-Ion Collisions
   Poster: Higher Moments of Net-Proton Multiplicity Distributions in Cu+Cu Collisions at $\sqrt{s_{\mathrm{NN}}}$ = 22.4, 62.4 and 200 GeV at STAR

2. The 35th winter workshop on nuclear dynamics 2019.
   Talk: Measurements of Cumulants of Net-proton, Proton and Anti-proton Multiplicity Distributions at STAR.

Acknowledgements

Firstly, I would like to express my gratitude to my supervisor, Prof. Xiaofeng Luo. He is a patient, easy-going and humble person and an expert on the fluctuations analysis in the STAR experiments. His strong code writing and data analysis ability helped me overcome the difficulties on the road of scientific research, cultivate my serious attitude and the independent ability to do scientific research. When I was admitted to this university, he gave me an opportunity to join in his group and study the higher order cumulants in heavy ion collisions. Thank you for giving me guidance in the analysis of higher order cumulants. Thank you for providing many opportunities to communicate with the experts and exchange ideas with other students by going out for meetings. Thank you for providing the opportunity to continue my study in the Lawrence Berkeley National Laboratory for two years. I also would like to express my gratitude to Prof. Nu Xu. His profound knowledge gave me a lot of comments and suggestions in the higher moments analysis, and great help when I was at LBNL.

Many thanks to the STAR group members at CCNU. I would like to express my thanks to Prof. Feng Liu, Shusu Shi, Ning Yu, Hua Pei and Zhiming Li for their suggestions at group meeting. Thanks to Ji Xu, Liang Zhang, Shili Yu and Biao Tu for your help in the beginning of learning data analysis. Thanks to Dingwei Zhang, Yu Zhang, Shu He, Shaowei Lan and Hui Liu for helping submit the forms during my stay at LBNL. Thanks to Pan Chai, Yilong Wang, Chang Zhou, Xixia Feng, Jiamin Chen, Ke Liu, Yufu Lin, Yanhua Zhang and Yaxiong Zhao for the happy times with you. Thanks to Ke Mi, Chun Tian, Yun Huang, Chuan Fu, Jingdong Zeng, Yige Huang, Ruiqin Wang, Shaoqiu Fang, Keli Liu, Jin Wu, Yingjie Zhou, Zuowen Liu and Shuai Zhou for working together.

Many thanks to Dr. Xin Dong and Dr. Grazyna Odyniec in the RNC group at LBNL. Thank you for providing a lot of help in my life and study. Thank you for giving valuable advices on my presentations. Thanks to Jinlong Zhang and Xiaolong Chen for their tips on my code learning and data analysis. Thanks to Yuanjing Ji, Yue Liang, Xinyue Ju and Yaping Xie for the happy lunch times with you. Especially thanks to Kathryn Meehan for taking me to UC Davis to discuss with Deniel Cebra, driving me to the grocery store and running together.

Many thanks to Wan Chang, Yufu Lin and Pengfei Wang at BNL. Thank you for the hot pot and grocery shopping during my STAR shift at BNL.

This is a special year with the outbreak of COVID-19. I would like to hats off to the medical staff and many of the staff, who are fighting COVID-19 on the front line. Thank you for your courage, dedication and sacrifice. Thank you for protecting life with your life. Hope COVID-19 is over soon. Tomorrow is another day.

Finally, I would like to give my appreciate to my family for their understanding, supporting and encouragement. Without your love, encouragement and support, I couldn't overcome many difficulties along the way and finish the thesis.

Appendix

A Formula

A.1 Formula for Moments

According to the definition of the central moments Eq. 1.28, we can express the higher-order central moments as terms of the moments about zero:

$$\mu_1 \equiv E(X - EX) = 0 \tag{A.1}$$

$$\begin{aligned}\mu_2 &\equiv E(X - EX)^2 = \langle (X - \langle X \rangle)^2 \rangle = \langle (\delta X)^2 \rangle \\ &= \langle (X^2 - 2X\langle X \rangle + \langle X \rangle^2) \rangle \\ &= \langle X^2 \rangle - \langle X \rangle^2 \end{aligned} \tag{A.2}$$

$$\begin{aligned}\mu_3 &\equiv E(X - EX)^3 = \langle (X - \langle X \rangle)^3 \rangle = \langle (\delta X)^3 \rangle \\ &= \langle (X^3 - 3X^2\langle X \rangle + 3X\langle X \rangle^2 - \langle X \rangle^3) \rangle \\ &= \langle X^3 \rangle - 3\langle X^2 \rangle\langle X \rangle + 2\langle X \rangle^3 \end{aligned} \tag{A.3}$$

$$\begin{aligned}\mu_4 &\equiv E(X - EX)^4 = \langle (X - \langle X \rangle)^4 \rangle = \langle (\delta X)^4 \rangle \\ &= \langle (X^4 - 4X^3\langle X \rangle + 6X^2\langle X \rangle^2 - 4X\langle X \rangle^3 + \langle X \rangle^4) \rangle \\ &= \langle X^4 \rangle - 4\langle X^3 \rangle\langle X \rangle + 6\langle X^2 \rangle\langle X \rangle^2 - 3\langle X \rangle^4 \end{aligned} \tag{A.4}$$

where $\delta X = X - \langle X \rangle$. Thus, the central moments can be expressed in terms of moments about zero:

$$\mu_1 = 0 \tag{A.5}$$

$$\mu_2 = m_2 - m_1 \tag{A.6}$$

$$\mu_3 = m_3 - 3m_2m_1 + 2m_1^3 \tag{A.7}$$

$$\mu_4 = m_4 - 4m_3m_1 + 6m_2m_2^2 - 3m_1^4 \tag{A.8}$$

A.2 Formula for Cumulants

According to the definition of the cumulants Eq. 1.33, we have the expression for up to forth-order cumulants:

$$C_1 = \frac{d}{dt}logM_X(t)|_{t=0} = \frac{M_X^{(1)}(t)}{M_X(t)}|_{t=0}$$
$$= \langle X \rangle \tag{A.9}$$

$$C_2 = \frac{d^2}{dt^2}logM_X(t)|_{t=0} = \frac{d}{dt}[\frac{M_X^{(1)}(t)}{M_X(t)}]|_{t=0}$$
$$= \frac{M_X^{(2)}(t)}{M_X(t)}|_{t=0} - (\frac{M_X^{(1)}(t)}{M_X(t)})^2|_{t=0}$$
$$= \langle X^2 \rangle - \langle X \rangle^2$$
$$= \langle (\delta X)^2 \rangle \tag{A.10}$$

$$C_3 = \frac{d^3}{dt^3}logM_X(t)|_{t=0} = \frac{d}{dt}[\frac{M_X^{(2)}(t)}{M_X(t)} - (\frac{M_X^{(1)}(t)}{M_X(t)})^2]|_{t=0}$$
$$= \frac{M_X^{(3)}(t)}{M_X(t)}|_{t=0} - 3\frac{M_X^{(2)}(t)}{M_X(t)}\frac{M_X^{(1)}(t)}{M_X(t)}|_{t=0} + 2(\frac{M_X^{(1)}(t)}{M_X(t)})^3|_{t=0}$$
$$= \langle X^3 \rangle - 3\langle X \rangle \langle X^2 \rangle + 2\langle X \rangle^3$$
$$= \langle (\delta X)^3 \rangle \tag{A.11}$$

$$C_4 = \frac{d^4}{dt^4}logM_X(t)|_{t=0} = \frac{d}{dt}[\frac{M_X^{(3)}(t)}{M_X(t)} - 3\frac{M_X^{(2)}(t)}{M_X(t)}\frac{M_X^{(1)}(t)}{M_X(t)} + 2(\frac{M_X^{(1)}(t)}{M_X(t)})^3]|_{t=0}$$
$$= [\frac{M_X^{(4)}(t)}{M_X(t)}]|_{t=0} - 4\frac{M_X^{(3)}(t)}{M_X(t)}\frac{M_X^{(1)}(t)}{M_X(t)}|_{t=0} - 3[\frac{M_X^{(2)}(t)}{M_X(t)}]^2|_{t=0}$$
$$+ 12\frac{M_X^{(2)}(t)}{M_X(t)}[\frac{M_X^{(1)}(t)}{M_X(t)}]^2|_{t=0} - 6[\frac{M_X^{(1)}(t)}{M_X(t)}]^4|_{t=0}$$
$$= \langle X^4 \rangle - 4\langle X^3 \rangle \langle X \rangle - 3\langle X^2 \rangle^2 + 12\langle X^2 \rangle \langle X \rangle^2 - 6\langle X \rangle^4$$
$$= \langle (\delta X)^4 \rangle - 3\langle (\delta X)^2 \rangle^2 \tag{A.12}$$

A.3 Relationship between Cumulants and Moments

From Eq. A.10–Eq. A.12, the cumulants can also be written as the terms of moments:

$$C_1 = m_1 \tag{A.13}$$
$$C_2 = m_2 - m_1^2 = \mu_2 \tag{A.14}$$
$$C_3 = m_3 - 3m_2m_1 + 2m_1^3 = \mu_3 \tag{A.15}$$
$$C_4 = m_4 - 4m_3m_1 - 3m_2^2 + 12m_2m_1^2 - 6m_1^4 = \mu_4 - 3\mu_2^2 \tag{A.16}$$

And vice versa, according to the relationship of moment-generating function Eq. 1.26 and cumulant-generating function Eq. 1.32, the moments can be written as terms of cumulant-generating function, and the terms of the cumulants:

$$m_n = \frac{d^n}{dt^n} M_X(t)|_{t=0} = \frac{d^n}{dt^n} e^{K_X(t)}|_{t=0} = M_X^{(n)}(0) \tag{A.17}$$

where $e^{K_X(0)} = M_X(0) = 1$, and $K_X^{(n)}(0) = C_n$.

Thus, the up to fourth-order central moments can be expressed as:

$$\begin{aligned} m_1 &= \frac{d}{dt} e^{K_X(t)}|_{t=0} = e^{K_X(t)} K_X^{(1)}(t)|_{t=0} \\ &= C_1 \end{aligned} \tag{A.18}$$

$$\begin{aligned} m_2 &= \frac{d^2}{dt^2} e^{K_X(t)}|_{t=0} = \frac{d}{dt} e^{K_X(t)} K_X^{(1)}(t)|_{t=0} \\ &= e^{K_X(t)} K_X^{(2)}(t)|_{t=0} + e^{K_X(t)}[(K_X^{(1)}(t)]^2|_{t=0} \\ &= C_2 + C_1^2 \end{aligned} \tag{A.19}$$

$$\begin{aligned} m_3 &= \frac{d^3}{dt^3} e^{K_X(t)}|_{t=0} = \frac{d}{dt}\left\{ e^{K_X(t)} K_X^{(2)}(t) + e^{K_X(t)}[(K_X^{(1)}(t)]^2 \right\}|_{t=0} \\ &= e^{K_X(t)} K_X^{(3)}(t)|_{t=0} + 3e^{K_X(t)} K_X^{(2)}(t) K_X^{(1)}(t)|_{t=0} + e^{K_X(t)}[(K_X^{(1)}(t)]^3|_{t=0} \\ &= C_3 + 3C_2C_1 + C_1^3 \end{aligned} \tag{A.20}$$

$$\begin{aligned} m_4 &= \frac{d^4}{dt^4} e^{K_X(t)}|_{t=0} \\ &= \frac{d}{dt}\left\{ e^{K_X(t)} K_X^{(3)}(t) + 3e^{K_X(t)} K_X^{(2)}(t) K_X^{(1)}(t) + e^{K_X(t)}[(K_X^{(1)}(t)]^3 \right\}|_{t=0} \\ &= e^{K_X(t)} K_X^{(4)}(t)|_{t=0} + 4e^{K_X(t)} K_X^{(3)}(t) K_X^{(1)}(t)|_{t=0} + 3e^{K_X(t)}[K_X^{(2)}(t)]^2|_{t=0} \\ &\quad + 6e^{K_X(t)} K_X^{(2)}(t)[K_X^{(1)}(t)]^2|_{t=0} + e^{K_X(t)}[(K_X^{(1)}(t)]^4|_{t=0} \\ &= C_4 + 4C_3C_1 + 3C_2^2 + 6C_2C_1^2 + C_1^4 \end{aligned} \tag{A.21}$$

A.4 Formula for Factorial Moments

According to the definition of the factorial moments Eq. 1.53, we have the expression for various order factorial moments:

$$F_1 = \frac{d}{dt}\langle t^X \rangle|_{t=1} = \langle X t^{X-1} \rangle|_{t=1} = \langle X \rangle \tag{A.22}$$

$$\begin{aligned} F_2 &= \frac{d^2}{dt^2}\langle t^X \rangle|_{t=1} = \frac{d}{dt}\langle X t^{X-1} \rangle|_{t=1} \\ &= \langle X(X-1) t^{X-2} \rangle|_{t=1} \\ &= \langle X(X-1) \rangle \\ &= \langle X^2 \rangle - \langle X \rangle \end{aligned} \tag{A.23}$$

$$
\begin{aligned}
F_3 &= \frac{d^3}{dt^3}\langle t^X\rangle|_{t=1} = \frac{d}{dt}\langle X(X-1)t^{X-2}\rangle|_{t=1} \\
&= \langle X(X-1)(X-2)t^{X-3}\rangle|_{t=1} \\
&= \langle X(X-1)(X-2)\rangle \\
&= \langle X^3\rangle - 3\langle X^2\rangle + 2\langle X\rangle
\end{aligned} \tag{A.24}
$$

$$
\begin{aligned}
F_4 &= \frac{d^4}{dt^4}\langle t^X\rangle|_{t=1} = \frac{d}{dt}\langle X(X-1)(X-2)t^{X-3}\rangle|_{t=1} \\
&= \langle X(X-1)(X-2)(X-3)t^{X-4}\rangle|_{t=1} \\
&= \langle X(X-1)(X-2)(X-3)\rangle \\
&= \langle X^4\rangle - 6\langle X^3\rangle + 11\langle X^2\rangle - 6\langle X\rangle
\end{aligned} \tag{A.25}
$$

A.5 Formula for Correlation Function

According to the definition of the correlation function Eq. 1.59, we have the expression for various order correlation function:

$$
\kappa_1 = \frac{d}{dt}lnH_X(t)|_{t=1} = \frac{H_X^{(1)}(t)}{H_X(t)}|_{t=1} = F_1 \tag{A.26}
$$

$$
\begin{aligned}
\kappa_2 &= \frac{d^2}{dt^2}lnH_X(t)|_{t=1} = \frac{d}{dt}\frac{H_X^{(1)}(t)}{H_X(t)}|_{t=1} \\
&= \frac{H_X^{(2)}(t)}{H_X(t)}|_{t=1} - (\frac{H_X^{(1)}(t)}{H_X(t)})^2|_{t=1} \\
&= F_2 - F_1^2
\end{aligned} \tag{A.27}
$$

$$
\begin{aligned}
\kappa_3 &= \frac{d^3}{dt^3}lnH_X(t)|_{t=1} = \frac{d}{dt}[\frac{H_X^{(2)}(t)}{H_X(t)} - (\frac{H_X^{(1)}(t)}{H_X(t)})^2]|_{t=1} \\
&= \frac{H_X^{(3)}(t)}{H_X(t)}|_{t=1} - 3\frac{H_X^{(2)}(t)}{H_X(t)}\frac{H_X^{(1)}(t)}{H_X(t)}|_{t=1} + 2(\frac{H_X^{(1)}(t)}{H_X(t)})^3|_{t=1} \\
&= F_3 - 3F_2F_1 + 2F_1^3
\end{aligned} \tag{A.28}
$$

$$
\begin{aligned}
\kappa_4 &= \frac{d^4}{dt^4}lnH_X(t)|_{t=1} = \frac{d}{dt}[\frac{H_X^{(3)}(t)}{H_X(t)} - 3\frac{H_X^{(2)}(t)}{H_X(t)}\frac{H_X^{(1)}(t)}{H_X(t)} + 2(\frac{H_X^{(1)}(t)}{H_X(t)})^3]|_{t=1} \\
&= \frac{H_X^{(4)}(t)}{H_X(t)}|_{t=1} - 4\frac{H_X^{(3)}(t)}{H_X(t)}\frac{H_X^{(1)}(t)}{H_X(t)}|_{t=1} - 3(\frac{H_X^{(2)}(t)}{H_X(t)})^2|_{t=1} \\
&\quad + 12\frac{H_X^{(2)}(t)}{H_X(t)}(\frac{H_X^{(1)}(t)}{H_X(t)})^2|_{t=1} - 6(\frac{H_X^{(1)}(t)}{H_X(t)})^4|_{t=1} \\
&= F_4 - 4F_3F_1 - 3F_2^2 + 12F_2F_1^2 - 6F_1^4
\end{aligned} \tag{A.29}
$$

A.6 Formula for Moments of Binomial Distributions

From Eq. 1.81–Eq. 1.84, moments of BD are given by:

$$
\begin{aligned}
m_1 &= \frac{d}{dt}\sum_{k=0} \frac{N!}{k!(N-k)!}p^k e^{kt}(1-p)^{N-k}|_{t=0} \\
&= \sum_{k=0} \frac{kN!}{k!(N-k)!}p^k e^{kt}(1-p)^{N-k}|_{t=0} \\
&= \sum_{k=1} \frac{Npe^t(N-1)!}{(k-1)!(N-k)!}p^{k-1} e^{(k-1)t}(1-p)^{N-k}|_{t=0} \\
&\Downarrow x = k-1 \qquad \text{(A.30)} \\
&= \sum_{x=0} \frac{Npe^t(N-1)!}{x!(N-1-x))!}p^{x} e^{tx}(1-p)^{N-1-x}|_{t=0} \\
&= Npe^t(1-p+pe^t)^{N-1}|_{t=0} \\
&= Np \qquad \text{(A.31)}
\end{aligned}
$$

where $\frac{kN!}{k!(N-k)!}p^k e^{kt}(1-p)^{N-k}|_{t=0,k=0} = 0$.

$$
\begin{aligned}
m_2 &= \frac{d}{dt}\sum_{k=0} \frac{kN!}{k!(N-k)!}p^k e^{kt}(1-p)^{N-k}|_{t=0} \\
&= \sum_{k=0} \frac{k^2N!}{k!(N-k)!}p^k e^{kt}(1-p)^{N-k}|_{t=0} \\
&= \sum_{k=1} \frac{N!}{(N-k)!}[\frac{k-1}{(k-1)!} + \frac{1}{(k-1)!}]p^k e^{kt}(1-p)^{N-k}|_{t=0} \\
&\Downarrow x = k-1 \qquad \text{(A.32)} \\
&= \sum_{x=0} \frac{xpe^tN(N-1)!}{x!(N-1-x))!}p^{x} e^{tx}(1-p)^{N-1-x}|_{t=0} + Np \\
&= N(N-1)p^2e^{2t}(1-p+pe^t)^{N-2}|_{t=0} + Np \\
&= N^2p^2 + Np(1-p) \qquad \text{(A.33)}
\end{aligned}
$$

$$
\begin{aligned}
m_3 &= \frac{d}{dt}\sum_k \frac{k^2 N!}{k!(N-k)!}p^k e^{kt}(1-p)^{N-k}|_{t=0} \\
&= \sum_k \frac{k^3 N!}{k!(N-k)!}p^k e^{kt}(1-p)^{N-k}|_{t=0} \\
&= \sum_k \frac{N!}{(N-k)!}[\frac{(k-1)(k-2)+3(k-1)+1}{(k-1)!}]p^k e^{kt}(1-p)^{N-k}|_{t=0} \\
&= N(N-1)(N-2)p^3 e^{3t}(1-p+pe^t)^{N-3}|_{t=0} + 3[N^2p^2 + Np(1-p)] + Np \\
&= N(N-1)(N-2)p^3 + 3N(N-1)p^2 + Np \\
&= N^3p^3 - 3N^2p^2(1-p) + Np(1-3p+2p^2) \qquad \text{(A.34)}
\end{aligned}
$$

$$
\begin{aligned}
m_4 &= \frac{d}{dt}\sum_k \frac{k^3 N!}{k!(N-k)!}p^k e^{kt}(1-p)^{N-k}|_{t=0} \\
&= \sum_k \frac{k^4 N!}{k!(N-k)!}p^k e^{kt}(1-p)^{N-k}|_{t=0} \\
&= \sum_k \frac{N!}{(N-k)!}[\frac{(k-1)(k-2)(k-3)+6(k-1)(k-2)+7(k-1)+6}{(k-1)!}]p^k e^{kt}(1-p)^{N-k}|_{t=0} \\
&= N(N-1)(N-2)(N-3)p^4 e^{4t}(1-p+pe^t)^{N-4}|_{t=0} \\
&\quad + 6N(N-1)(N-2)p^3 + 7N(N-1)p^2 + 6Np \\
&= N(N-1)(N-2)(N-3)p^4 + 6N(N-1)(N-2)p^3 + 7N(N-1)p^2 + Np \\
&= N^4p^4 - 6N^3p^3(1-p) + N^2p^2(7-18p+11p^2) + Np(1-7p+12p^2-6p^3) \qquad \text{(A.35)}
\end{aligned}
$$

A.7 Formula for Cumulants of Binomial Distributions

According to the definition of the cumulants of BD Eq. 1.80, we have the expression for various order cumulants of BD:

$$
\begin{aligned}
C_1 &= N\frac{d}{dt}ln(1-p+pe^t)|_{t=0} = N\frac{pe^t}{1-p+pe^t}|_{t=0} \\
&= Np \qquad \text{(A.36)}
\end{aligned}
$$

$$
\begin{aligned}
C_2 &= N\frac{d^2}{dt^2}ln(1-p+pe^t)|_{t=0} = N\frac{d}{dt}\frac{pe^t}{1-p+pe^t}|_{t=0} \\
&= N\frac{pe^t}{1-p+pe^t}|_{t=0} - N(\frac{pe^t}{1-p+pe^t})^2|_{t=0} \\
&= Np(1-p) \qquad \text{(A.37)}
\end{aligned}
$$

$$\begin{aligned}
C_3 &= N\frac{d^3}{dt^3}ln(1-p+pe^t)|_{t=0} = N\frac{d}{dt}[\frac{pe^t}{1-p+pe^t} - (\frac{pe^t}{1-p+pe^t})^2]|_{t=0} \\
&= N\frac{pe^t}{1-p+pe^t}|_{t=0} - 3N(\frac{pe^t}{1-p+pe^t})^2|_{t=0} + 2N(\frac{pe^t}{1-p+pe^t})^3|_{t=0} \\
&= Np(1-p)(1-2p) \\
&= Np(1-3p+2p^2) \qquad (A.38)
\end{aligned}$$

$$\begin{aligned}
C_4 &= N\frac{d^3}{dt^3}ln(1-p+pe^t)|_{t=0} \\
&= N\frac{d}{dt}[\frac{pe^t}{1-p+pe^t} - 3(\frac{pe^t}{1-p+pe^t})^2 + 2(\frac{pe^t}{1-p+pe^t})^3]|_{t=0} \\
&= N\frac{pe^t}{1-p+pe^t}|_{t=0} - 7N(\frac{pe^t}{1-p+pe^t})^2|_{t=0} + 12N(\frac{pe^t}{1-p+pe^t})^3|_{t=0} \\
&\quad - 6N(\frac{pe^t}{1-p+pe^t})^4|_{t=0} \\
&= Np(1-7p+12p^2-6p^3) \qquad (A.39)
\end{aligned}$$

Usually, we have:

$$\begin{aligned}
\frac{d}{dt}(\frac{pe^t}{1-p+pe^t})^n|_{t=0} &= n(\frac{pe^t}{1-p+pe^t})^n|_{t=0} - n(\frac{pe^t}{1-p+pe^t})^{n+1}|_{t=0} \\
&= np^n - np^{n+1} \\
&= np^n(1-p) \qquad (A.40)
\end{aligned}$$

B Tables for Details

Tab. B.1: EventId cuts at $\sqrt{s_{\mathrm{NN}}}$ = 7.7 GeV. The first column is the bad run number, and the second column shows the event Id. For event boundary, we need to remove all events before that event Id.

RunId	EventId	RunId	EventId	RunId	EventId
11123022	21016	11126033	61875	11130005	33806
11124013	23879	11126034	50369	11130007	53262
11125072	64756	11126035	23438	11130010	37838
11125078	67273	11126044	53583	11130011	30055
11125079	78581	11129007	44492	11130022	54371
11125085	61019	11129027	22920	11130023	53040
11125100	58912	11129064	53517	11130024	54270
11125101	51412	11129074	45949	11130026	23619
11125102	47067	11129076	41697	11130043	23846
11126001	40854	11129077	52600	11140094	130816
11126004	44678	11129078	67841	11140096	66021
11126010	47188	11129079	30795	11141001	66960
11126011	78231	11129080	22733	11141021	62837
11126012	66410	11129081	62777	11141023	56108
11126014	28841	11129082	64989	11141068	29345
11126015	30924	11130001	66901	11143035	27277
11126028	24609	11130002	37324	11144010	20570
11126031	63731	11130003	48597	11144063	20562
11126032	33541	11130004	57035		

Tab. B.2: Bad eventId cuts at $\sqrt{s_{\mathrm{NN}}}$ = 11.5, 14.5, 19.6, 27, 39 and 62.4 GeV.

$\sqrt{s_{\mathrm{NN}}}$ (GeV)	**EventId Cuts**
11.5	if (RunId == 11148017) { if (EventId <= 42349) continue;}
	if (RunId == 11148048) { if (EventId <= 29116) continue;}
	if (RunId == 11148057) { if (EventId <= 42611) continue;}
	if (RunId == 11148067) { if (EventId <= 24713) continue;}
	if (RunId == 11148071) { if (EventId <= 40455) continue;}
	if (RunId == 11149002) { if (EventId <= 36872) continue;}
	if (RunId == 11149009) { if (EventId <= 31302) continue;}
	if (RunId == 11149012) { if (EventId <= 21430) continue;}
	if (RunId == 11149013) { if (EventId <= 23563) continue;}
	if (RunId == 11149014) { if (EventId <= 34073) continue;}
	if (RunId == 11149086) { if (EventId <= 20511) continue;}
	if (RunId == 11150002) { if (EventId <= 20335) continue;}
	if (RunId == 11151070) { if (EventId <= 34788) continue;}
	if (RunId == 11157028) { if (EventId <= 27977) continue;}
14.5	if (RunId == 15049041) continue;
19.6	if (RunId == 12114001) { if (EventId > 300000) continue;}
	if (RunId == 12114024) { if (EventId > 40000) continue;}
	if (RunId >= 12114038 && RunId <= 12114121) continue;
	if (RunId == 12115011) { if (EventId > 125000) continue;}
	if (RunId == 12115092) { if (EventId > 180000) continue;}
	if (RunId == 12115071) { if (EventId > 70000 && EventId < 110000) continue;}
	if (RunId == 12119064) { if (EventId > 80000 && EventId < 130000) continue;}
27	if (RunId == 12176066) { if (EventId > 560000) continue;}
	if (RunId == 12176017) { if (EventId>= 20000 && EventId <= 60000) continue;}
	if (RunId == 12176018) { if (EventId>= 240000 && EventId <= 280000) continue;}
	if (RunId == 12177053) { if (EventId>= 170000 && EventId <= 220000) continue;}
	if (RunId == 12179023) { if (EventId>= 80000 && EventId <= 100000) continue;}
	if (RunId == 12179061) { if (EventId>= 160000 && EventId <= 190000) continue;}
39	if (RunId == 11102085) { if (EventId >= 330000 && Eventid <= 410000) continue;}
	if (RunId == 11102085) { if (EventId >= 500000 && EventId <= 560000) continue;}
62.4	if (RunId == 11085031) { if (EventId >= 210000 && EventId <= 260000) continue;}
	if (RunId == 11086085) { if (EventId >= 225000) continue;}
	if (RunId>= 11084046 && RunId<=11084050) continue;
	if (RunId>= 11085047 && RunId<=11086019) continue;

Tab. B.3: Bad events cut in Au+Au Collisions at $\sqrt{s_{\mathrm{NN}}}$ = 7.7, 11.5, 14.5, 19.6, 27, 39, 54.4, 62.4 and 200 GeV. These cuts should be included in the analysis.

$\sqrt{s_{\mathrm{NN}}}$ (GeV)	nTofmatch and Beta_eta1 vs Refmult
7.7	if (nTofmatch ≤ 1 || nTofmatch $< 0.5\times$(Refmult$-$20)) continue; if (Beta_eta1 ≤ 0 || Beta_eta1 $< 26\times$(Refmult$-$20)/33.)) continue;
11.5	if (nTofmatch ≤ 1 || nTofmatch $< 0.4848\times$(Refmult$-$20)) continue; if (Beta_eta1 ≤ 0 || Beta_eta1 $< 29\times$(Refmult$-$20)/33.) continue;
14.5	if (nTofmatch ≤ 1 || nTofmatch $< 10\times$(Refmult$-$20)/19.) continue; if (Beta_eta1 ≤ 0 || Beta_eta1 $< 14\times$(Refmult$-$20)/19.) continue;
19.6	if (nTofmatch ≤ 1 || nTofmatch $< 0.5116\times$(Refmult$-$20)) continue; if (Beta_eta1 ≤ 0 || Beta_eta1 $< 37\times$(Refmult$-$20)/43.) continue;
27	if (nTofmatch ≤ 1 || nTofmatch $< 0.5208\times$(Refmult$-$20)) continue; if (Beta_eta1 ≤ 0 || Beta_eta1 $< 19\times$(Refmult$-$20)/22.) continue;
39	if (nTofmatch ≤ 1 || nTofmatch $< 0.5208\times$(Refmult$-$20)) continue; if (Beta_eta1 ≤ 0 || Beta_eta1 $< 7\times$(Refmult $-$20)/8.) continue;
54.4	if ((nTofmatch +10) $\leq 0.46\times$ Refmult) continue; if ((tofmult+100) $\leq 2.7\times$Refmult || (tofmult-230) $\geq 3.7\times$ Refmult) continue;
62.4	if (nTofmatch ≤ 1 || nTofmatch $< 0.5172\times$ (Refmult$-$20)) continue; if (Beta_eta1 ≤ 0 || Beta_eta1 $< 21\times$(Refmult$-$21)/26.) continue;
200	if (nTofmatch ≤ 1 || nTofmatch $< 0.5\times$(Refmult$-$40)) continue; if ((Beta_eta1 ≤ 0 || Beta_eta1 $< 25\times$(Refmult$-$40)/31.) continue;